Analysis of oxidative stress and metabolic reprogramming in HPV^{+} HNSCC

Inaugural-Dissertation

Dissertation

zur

Erlangung des Doktorgrades

der Mathematisch-Naturwissenschaftlichen Fakultät

der Universität zu Köln

vorgelegt von

Harini Balaji

geboren in Chennai, Indien

angenommen im Jahr 2025

Table of content

1 List of abbreviation

AKR1C	Aldo-Keto Reductase family 1 member C
AKT	Protein Kinase B
APOBEC	Apolipoprotein B mRNA-editing enzyme, catalytic polypeptide-like
APOT	Amplification of Papillomavirus Oncogene Transcripts
ATP	Adenosine triphosphate
BABAM2	BRISC and BRCA1 A complex member 2
BWA	Burrows–Wheeler Aligner
BWA-MEM	Burrows–Wheeler Aligner Maximal Exact Matches
BWA-SW	Burrows–Wheeler Aligner Smith–Waterman
CD200	Cluster of Differentiation 200
CD36	Cluster of Differentiation 36
CO_2	Carbon dioxide
COX	Cyclooxygenase
CUL3	Cullin-3
CYLD	Cylindromatosis (deubiquitinase)
DG8	DG8 Genotyping Chip
DIPS-PCR	Detection of Integrated Papillomavirus Sequences - Polymerase Chain Reaction
DUOX1	Dual oxidase 1
ECAR	Extracellular acidification rate

EGFR	Epidermal growth factor receptor
ETC	Electron transport chain
ETS2	ETS Proto-Oncogene 2
FDG	Fluorodeoxyglucose
FFPE	Formalin-fixed paraffin-embedded
FISH	Fluorescence in situ hybridisation
GFP	Green fluorescent protein
GLUT	Glucose transporter
GPX3	Glutathione peroxidase 3
HEK 293	Human embryonic kidney 293 cells
GFP	Green fluorescent protein
HIC1	Hypermethylated in cancer 1
HIF	Hypoxia-inducible factor
HK2	Hexokinase 2
HPRT-1	Hypoxanthine phosphoribosyltransferase 1
HPV16/18	Human papillomavirus type 16/18
HSPG	Heparan sulfate proteoglycan
KEAP1	Kelch-like ECH-associated protein 1
KLF5	Krüppel-like factor 5
LDHA	Lactate dehydrogenase A
LNA-RNA	Locked nucleic acid - ribonucleic acid
MPO	Myeloperoxidase

MYC	MYC proto-oncogene
NAD	Nicotinamide adenine dinucleotide
NADPH	Nicotinamide adenine dinucleotide phosphate (reduced form)
NF	Nuclear factor
NGS	Next-generation sequencing
NHANES	National Health and Nutrition Examination Survey
NQO1	NAD(P)H quinone dehydrogenase 1
O_2	Oxygen
OCR	Oxygen consumption rate
OS	Oxidative stress
OSCC	Oral squamous cell carcinoma
PBM	Peripheral blood mononuclear cells
PBSA	Phosphate-buffered saline with albumin
PD-L1	Programmed death-ligand 1
PDK1	Pyruvate dehydrogenase kinase 1
PGC	Peroxisome proliferator-activated receptor gamma coactivator
PKM2	Pyruvate kinase M2
PX1	Pannexin 1
RBX1	Ring-box 1
SOD2	Superoxide dismutase 2
SP1	Specificity protein 1
SPSS	Statistical Package for the Social Sciences

SRXN1	Sulfiredoxin 1
STR	Short tandem repeat
SV	Structural variant
TCA	Tricarboxylic acid cycle
TCF-4	Transcription factor 4
TGFBR2	Transforming growth factor beta receptor 2
TLA	Targeted locus amplification
TLC	Targeted locus capture
TMEM182	Transmembrane protein 182
TP 53/63	tumour protein p5363
TPRG1	tumour protein receptor gene 1
TRAF3	TNF receptor-associated factor 3
WGS	Whole genome sequencing
XRCC4	X-ray repair cross complementing 4

2 Abstract

HPV-positive (HPV^+) oropharyngeal squamous cell carcinoma (OPSCC) represents a biologically distinct subset of head and neck cancer with generally favourable outcomes compared to HPV-negative (HPV^-) disease. Nevertheless, 20–25% of HPV^+ OPSCC patients develop recurrence or metastasis, reflecting a clinically relevant subgroup with poor prognosis. This aggressive behaviour is frequently associated with HPV16 host genome integration and high expression of the splice variant HPV16-E6*I, which often co-occurs with PI3K pathway mutations and 3q chromosomal gains. These tumours adopt metabolic and redox profiles resembling HPV^- cancers, illustrating the limitations of current $p16^{INK4a}$-based risk stratification and underscoring the need for HPV-specific biomarkers to guide therapy. This builds on previous research from our group, which identified that HPV16 integration and HPV16-E6*I overexpression and are both associated with unfavourable disease outcome.

To address this, we developed FFPE-targeted locus capture (FFPE-TLC), a proximity-ligation sequencing method optimised for formalin-fixed, paraffin-embedded tissue. FFPE-TLC achieves high-resolution mapping of virus–host breakpoints and local structural variation, enabling integration analysis directly from diagnostic samples. In a cohort of $HPV16^+$ OPSCC, ~56% of tumours contained HPV integration, frequently accompanied by simple rearrangements and intratumour heterogeneity. Breakpoints often localised near genes involved in DNA repair, epithelial–mesenchymal transition (EMT), and apoptosis signalling. Importantly, shared integration sites in primary and metastatic lesions confirmed viral insertion as a stable clonal marker.

To functionally link integration-associated isoforms with phenotype, we established HEK 293 models stably overexpressing HPV16-E6 or -E6*I under O_2 levels that mimic tonsillar physiology. HPV16-E6*I broadly induced NRF2 and AKR1C3 expression with O_2-sensitive differences in subcellular localisation. Functionally, HPV16-E6*I enhanced migration under both hypoxia and hyperoxia and promoted a dual-fuel phenotype: oxidative phosphorylation (OXPHOS) activation with ATP

advantage at high O_2, and glycolytic flexibility under low O_2. By contrast, HPV16-E6 favoured glycolysis at physiologic normoxia. Inhibition of AKR1C1/3 reversed transcript changes and abolished migration, highlighting these enzymes as critical effectors of the HPV16-E6*I-driven redox–motility axis.

For translational application, we established isoform-specific RNA-FISH using locked nucleic acid (LNA) probes for HPV16-E6 and -E6*I in FFPE material. This enables spatial mapping of isoform expression in situ, which can be combined with FFPE-TLC data to stratify tumours by integration status, redox activity, and metabolic adaptation.

In conclusion, our study defines HPV16-E6*I as a central regulator linking viral integration to O_2-sensitive redox and metabolic reprogramming, thereby driving aggressive tumour behaviour in a clinically relevant OPSCC subgroup. By introducing FFPE-TLC and isoform-specific RNA-FISH as robust, clinically applicable tools, we provide a framework for biomarker-driven risk stratification and open new perspectives for tailored therapeutic strategies beyond p16-based classification.

3 Introduction

3.1 Epidemiology and Rising Burden of HNSCC and OPSCC

Head and neck squamous cell carcinoma (HNSCC) ranks as the seventh most prevalent cancer globally, with around 660,000 new cases and 325,000 fatalities documented each year (Gormley et al. 2022). Given the anatomical and histological diversity of head and neck cancer, where numerous distinct tissue types converge within a confined region, understanding its subtypes is crucial to grasp the disease's overall burden and biological complexity. HNSCC generally originates from the mucosal linings of the upper aerodigestive tract. HNSCCs arise in the oral cavity, oropharynx, and larynx in more than 90% of cases (Fig.1) (Balaji et al. 2021). While HNSCC has traditionally been associated with risk factors such as tobacco and alcohol use, a striking shift has emerged in recent years: the proportion of human papillomavirus (HPV)-associated oropharyngeal carcinomas (OPSCC) is rapidly increasing - bringing significant implications for pathogenesis, therapy, and prognosis (Leemans et al. 2011).

3.2 Clinical Relevance of HPV$^+$ OPSCC

OPSCC, a subtype originating from the squamous epithelium of the tonsils, base of the tongue, soft palate, and the pharyngeal walls, constitutes approximately 11% of all HNSCC cases. Over the last two decades, there has been a notable rise in the incidence of OPSCC, a trend that is particularly pronounced in high-income countries. (Jemal et al. 2013; Faraji et al. 2019; Lim and D'Silva 2024). This rise is primarily due to ongoing infection with high-risk human papillomavirus (HR-HPV), mainly HPV16. Estimates suggest a subsequent 50% rise in the incidence and mortality of OPSCC over the next two decades (Lim and D'Silva 2024). Remarkably, HPV-positive (HPV$^+$) OPSCC has now exceeded cervical cancer in prevalence among HPV$^+$ malignancies in the United States (Sonawane et al. 2017; Lechner et al. 2022; Ziogas et al. 2024).

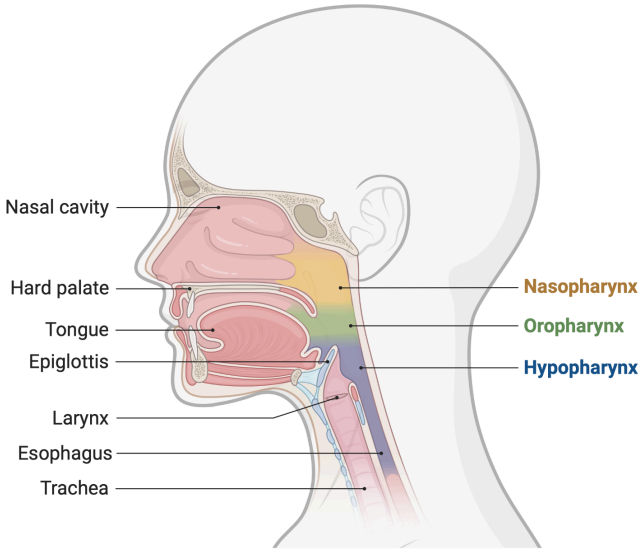

Figure 1. Anatomical Locations for HNSCC Onset. HNSCC arises from the mucosal epithelium lining the oral cavity, nasopharynx, oropharynx, hypopharynx, and larynx. Created in https://BioRender.com.

3.3 Distinct Oncogenic Pathways in HPV$^+$ Versus HPV$^-$ OPSCC

This notable epidemiological shift has led researchers to distinguish OPSCC into two major categories based on etiological factors: those related to HR-HPV infection and those driven by traditional risk factors like tobacco and alcohol. HPV$^+$ OPSCC arises by distinct viral oncogenic mechanisms. This contrasts with the observation that tumours associated with smoking and alcohol consumption typically exhibit mutations in TP53 and present complex mutational profiles resulting from early mutational processes (Martínez-Ramírez et al. 2018; Leemans et al. 2011). Conversely, HPV$^+$ OPSCC is characterised by viral alteration of host cell metabolism and deregulation of the cell cycle during prolonged infection (Leemans et al. 2011; Karbalaie Niya et al. 2018).

3.4 Molecular Mechanisms of HPV Infection and Persistence

For an HPV infection to be regarded as biologically relevant, there are several factors that are considered to be necessary. Sites of infection are typically lined by stratified squamous epithelium derived from the ectoderm. The virus shows a particular

predilection for certain epithelial niches, including the salivary glands of the oral cavity and the crypts of the tonsils. It has also been detected in areas where stratified epithelium is in close proximity to the squamocolumnar junction such as the uterine cervical transformation zone (Woodman et al. 2007; Balaji et al. 2021). These regions are thought to be more susceptible to HPV entry due to their reduced epithelial barrier integrity, which facilitates viral access to basal epithelial stem and progenitor cells. The increased presence of epithelial reserve and stem cells in these areas likely contributes to the heightened vulnerability to persistent infection and malignant transformation. Furthermore, successful viral entry requires wounds or microlesions that disrupt the epithelium, thereby allowing HPV to access and infect the basal cell layer, where its target cells reside. An inflow of serum containing growth factors (GFs), cytokines, and heparan sulphate proteoglycan (HSPGs) is produced at the sites of (micro)injury to promote wound healing. Subsequently, the HPV L1 capsid protein will bind to the HSPGs that have been exposed (Ozbun 2019; Balaji et al. 2021). Additionally, it is necessary for virions to bind to α6-integrins, which then proceeds to initiate other intracellular signalling events. Furthermore, conformational changes that are produced in HSPGs lead to the cleavage of L2, the binding of the exposed L2 N-terminus to an L2-specific receptor (annexin A2 heterotetramer), and the subsequent endocytosis of HPV that is independent of clathrin, caveolin, lipid raft, flotillin, cholesterol, and dynamin (Speel 2017; Balaji et al. 2021). Once HPV enters basal cells, including potential stem cell subsets, its genome is maintained as extrachromosomal, so-called episomal DNA and replicates in coordination with host cell division, typically at a stable copy number of about 50 copies per cell. The viral proteins E1 and E2 regulate replication, while E6 and E7 promote cellular proliferation, facilitating efficient viral genome amplification. The E6 and E7 proteins are two of the principal oncoproteins encoded by high-risk HPV, among several viral factors contributing to carcinogenesis. While E6 (full-length) promotes degradation of p53 and E7 disrupts the retinoblastoma (Rb) pathway, both of which are crucial steps in enabling uncontrolled cell proliferation, these represent just a subset of their broader oncogenic activities (Leemans et al. 2011). HPV16 produces an abundant spliced isoform, HPV16-E6*I, from the HPV16-E6 transcript, as well as the full-length HPV16-E6 protein. During productive infection, HPV16-E6*I acts as a

dominant-negative regulator of HPV16-E6, modulating host-cell signalling without targeting p53 for proteasomal degradation. HPV16-E6*I possesses a C-terminal PDZ-binding motif that facilitates interaction with PDZ-domain proteins, such as Dlg. These proteins regulate polarity and signalling in differentiating epithelia (Vazquez-Vega et al. 2013; Umnajvijit et al. 2021). There is evidence that HPV16-E6*I influences redox-responsive pathways, including the activation of NRF2 target genes such as AKR1C1 and AKR1C3, as well as controlling ROS signalling. This may facilitate the preservation of viral genomes and amplification associated with differentiation, while minimising robust inflammatory responses (Wanichwatanadecha et al. 2012; Huebbers et al. 2019). Subsequent sections will elaborate on HPV16-E6*I's role in malignant transformation and tumour behaviour. As infected cells undergo differentiation and move toward the surface of the epithelium, the E4 protein is expressed, and the structural proteins L1 and L2 are produced to facilitate assembly of new virions. E4 contributes to viral release by disrupting the intermediate filament network, leading to the shedding of virion-containing cell debris from the epithelial surface. It is important to note that this process avoids cell lysis, systemic spread, and strong inflammatory responses, thereby helping the virus to evade immune detection (Fig. 2) (Lim et al. 2023). This complex infection process establishes the foundation for persistent HPV infection, which can then trigger the subsequent stage of oncogenesis through metabolic reprogramming and genomic instability.

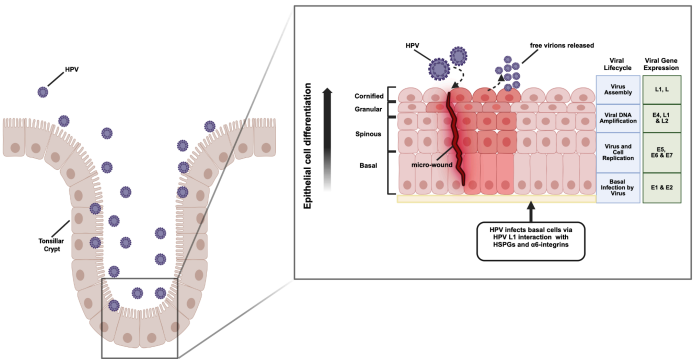

Figure 2. Molecular Basis of HPV Entry and Pathogenicity. To infect, HPV needs access to the basal epithelium through microlesions or wounds. These locations make proliferative cells susceptible

to infection and secrete serum rich in growth factors, cytokines, and tissue-repairing HSPGs. Upon binding to exposed HSPGs, HPV L1 capsid proteins interact with α6-integrins, leading to intracellular signalling. The virus-HSPG complex's structural modifications cleave L2, exposing its N-terminus for annexin A2 heterotetramer binding. This sequence helps HPV to be internalised without clathrin or caveolin. After entering basal cells, including potential stem cell populations, the HPV genome replicates with the host DNA at a stable copy number, around 50 per cell as so-called extrachromosomal episomes during cell division. Through E1 and E2 protein activity, viral proteins E6 and E7 enhance cell proliferation, enabling high-level viral genome replication. E4 expression and virion assembly capsid protein L1 and L2 synthesis occur as infected cells move and develop in the epithelium. By disrupting the cytokeratin network, E4 releases mature virus particles, allowing virion-containing cell remnants to spontaneously shed from the epithelial surface. This life cycle does not cause cell lysis, systemic infection, or a severe inflammatory response, allowing the virus to avoid local immune monitoring. Created in https://BioRender.com

3.5 Viral Genome Maintenance and Host Cell Alteration

Starting with a transient HPV infection, the viral genome is maintained as extrachromosomal episomes. To replicate efficiently within stratified squamous epithelia - where most cells are normally no longer permitted to divide and thus are limited in anabolic pathways - HPV must reprogram the local environment to support a metabolically favorable and proliferative state. This allows for the expression of viral genes, amplification of the genome, and assembly of new virions in differentiated epithelial layers (Vigneswaran and Williams 2014; Leemans et al. 2011). While these processes are tightly regulated, persistent infection combined with immune evasion leads to disruption of epithelial homeostasis. Reactive oxygen species (ROS) and reactive nitrogen species (RNS) can arise from various sources, including environmental exposures, chronic inflammation driven by HPV, particularly through the expression of the viral oncoproteins E6 and E7, as well as coinfections and host-derived inflammatory responses. These reactive species play a critical role in promoting DNA damage, genomic instability and metabolic reprogramming, all of which contribute to malignant transformation. Furthermore, Apolipoprotein B mRNA-editing catalytic (APOBEC) polypeptides were recently identified to contribute to HPV-induced DNA damage (Fig. 3). Persistent infection may ultimately lead to the breakage of viral DNA followed by integration of the viral genome into the host DNA, one of the pivotal events in malignant transformation (Balaji et al. 2021).

3.6 HPV Integration: Mechanisms, Functional Implications, and Emerging Detection Technologies

3.6.1 HPV Genome Integration: Mechanisms and Consequences

A key event in this malignant progression is the integration of the HPV genome into the host genome, which requires the breakage of both viral and host DNA (Balaji et al. 2021). This integration is believed to be closely associated with the extent of ROS- and RNS-mediated DNA damage, a phenomenon frequently observed in HPV$^+$ OPSCC. The accumulation of chromosomal alterations and the activation of DNA damage repair mechanisms are thought to facilitate this process by promoting conditions favorable for viral integration (Fig. 3). Two possible mechanisms have been proposed for how integration occurs: direct insertion and looping integration. Notably, this event frequently disrupts the viral E2 gene, resulting in the continuous expression of the oncoproteins E6 and E7 (Demers, Balaji et al., 2024).

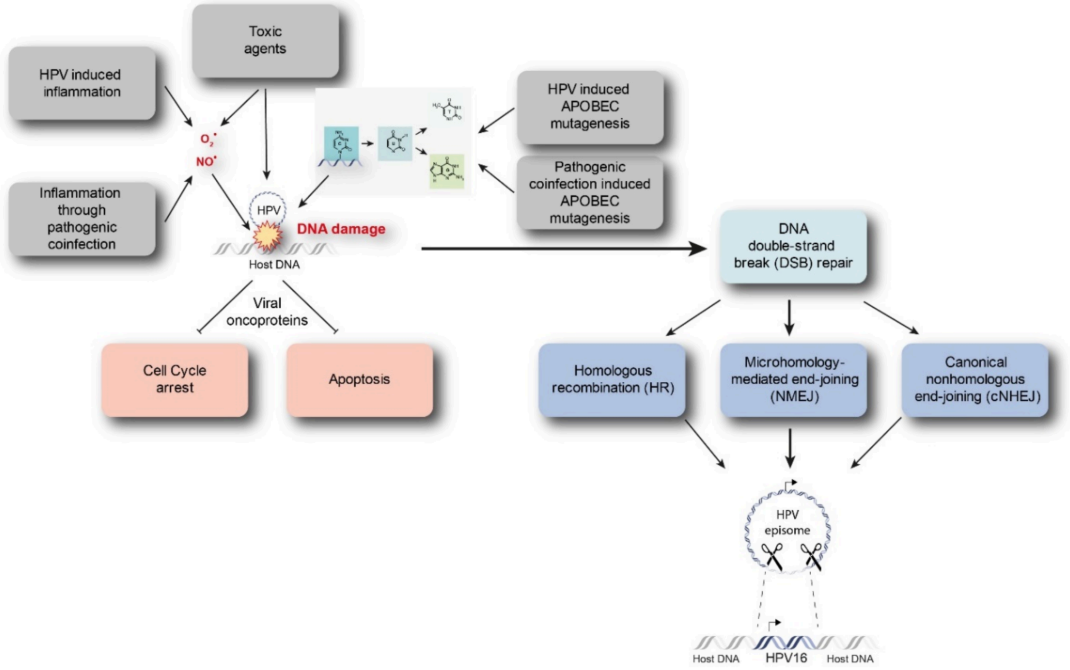

Figure 3. Drivers of HPV integration and DNA damage. Intrinsic and extrinsic factors, including inflammation, toxic chemicals, or APOBEC mutagenesis induced by HPV infection, can provoke DNA damage. Consequently, chromosomal abnormalities and DNA damage repair pathways may facilitate viral integration. (Balaji et al. 2021).

The integration of the HPV genome into the human genome is believed to modify carcinogenesis, potentially impacting disease development and patient prognosis (Balaji et al. 2021). Furthermore, the integration of HPV appears to disrupt cellular pathways and functions. This may occur through direct integration into or near an oncogene or tumour suppressor gene, or by enhancing the persistent expression of viral oncoproteins E6/E6*I/E7 (Fig. 4) (Balaji et al. 2021). Furthermore, recent discoveries indicate that interactions between the integrated HPV genome and host chromosomes result in the deregulation of host genes across considerable distances within regions known as topologically associated domains (TADs). It appears that integration into or near a "cancer gene" is not essential for influencing the expression of that gene (Groves et al. 2021). Consequently, these integration events have far-reaching implications not only for viral gene expression but also for host genome regulation and tumour progression.

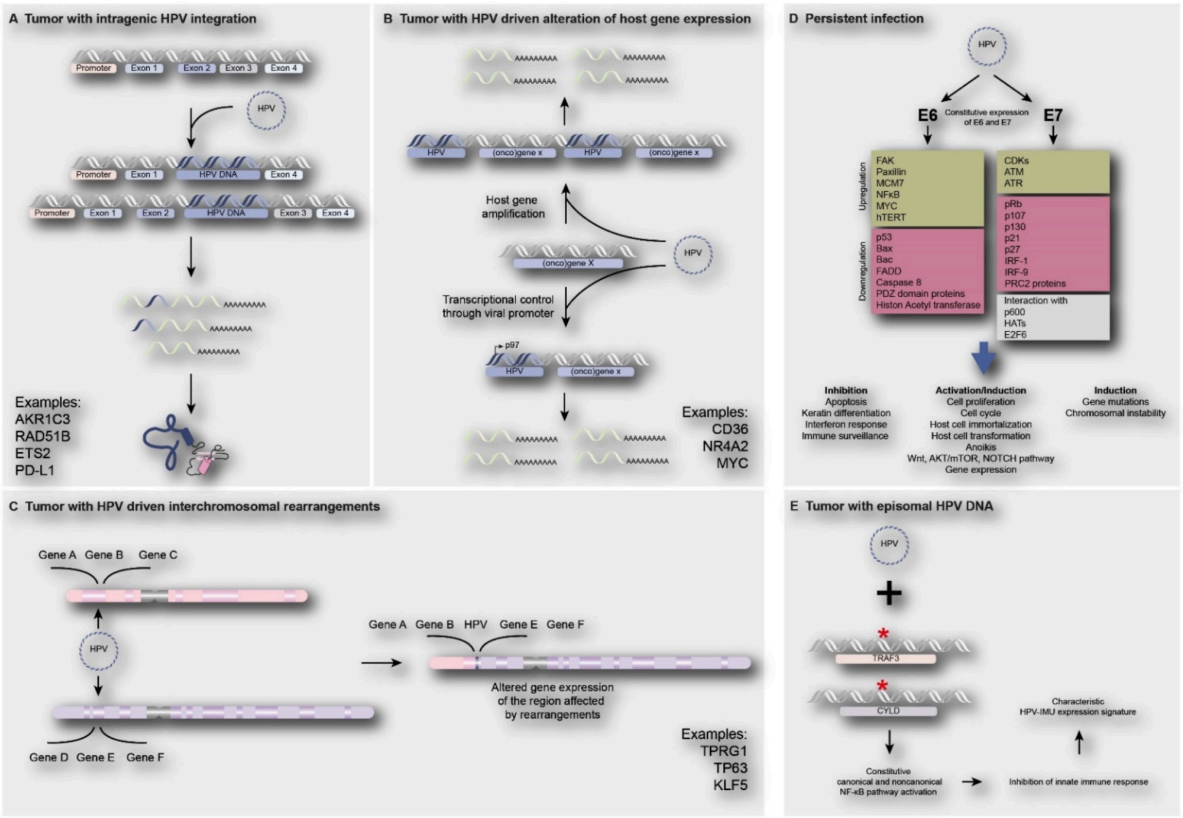

Figure 4. HPV's direct and indirect effects on gene expression. HPV integration into intragenic areas of the human genome has been shown to cause gene function loss and/or shortened proteins, including AKR1C3, RAD51B, ETS2, and PD-L1. (B) HPV integration near proto-oncogenes such as CD36, NR4A2, and MYC, which activates oncogenes by amplification or upregulation. (C) HPV

integration may cause interchromosomal rearrangements, gene amplification, and increased expression of genes such as TP63, TPRG1, and KLF5. (D) HPV infection has been shown to cause constitutive expression of E6 and E7 oncoproteins, resulting in deregulated signalling pathways, inhibition of apoptosis, activation of cell proliferation, and gene mutations or chromosomal instability. (E) Episomal HPV tumours frequently exhibit TRAF3/CYLD mutations, leading to NF-κB activation and suppression of innate immune responses (Balaji et al. 2021).

3.6.2 Technological Advances in HPV Integration Detection

The findings of studies regarding the prevalence of HPV integration and its clinical implications in OPSCC have shown considerable inconsistency. A plausible explanation for this inconsistency is the heterogeneity in integration patterns, genomic locations, and associated biological outcomes. In addition, as highlighted by numerous studies, there are multiple techniques available to detect HPV integration. These include fluorescence in situ hybridisation (FISH), polymerase chain reaction (PCR)-based techniques, and next-generation sequencing (NGS) methodologies (Fig. 5). Differences in detection methodologies are likely a major contributor to the variability in reported integration rates (Balaji et al. 2021). Recent studies using advanced NGS platforms have reported integration frequencies exceeding 50% in HPV^{+} OPSCC cases (Symer et al. 2022; Mainguené et al. 2022). Historically, many studies relied on fresh frozen tumour tissue for integration analysis. However, in addition to potential limitations such as detection bias, low sensitivity, and lack of specificity, research on HPV integration is further constrained by the limited compatibility of these methods with formalin-fixed, paraffin-embedded (FFPE) tissues, where DNA is often highly fragmented. As a result, DNA fragments may be too short to reliably map to specific loci in the human genome, complicating both large-scale studies and the translation of these techniques into routine diagnostic workflows (Demers, Balaji et al., 2024).

Figure 5 (next page). Summary of established and novel methodologies for detecting HPV integration into the human genome. Established methods for detecting integration encompass RNA-based techniques like APOT PCR (amplification of papilloma virus oncogene transcripts PCR) and RNAseq (RNA sequencing), as well as DNA-based approaches including DIPS-PCR (detection of integrated papillomavirus sequences by ligation-mediated PCR), whole genome sequencing (WGS), and enrichment or capture sequencing. Nanopore Sequencing and TLA are identified as novel methodologies for detecting HPV incorporation (Balaji et al. 2021).

Figure 5 (for legend see previous page)

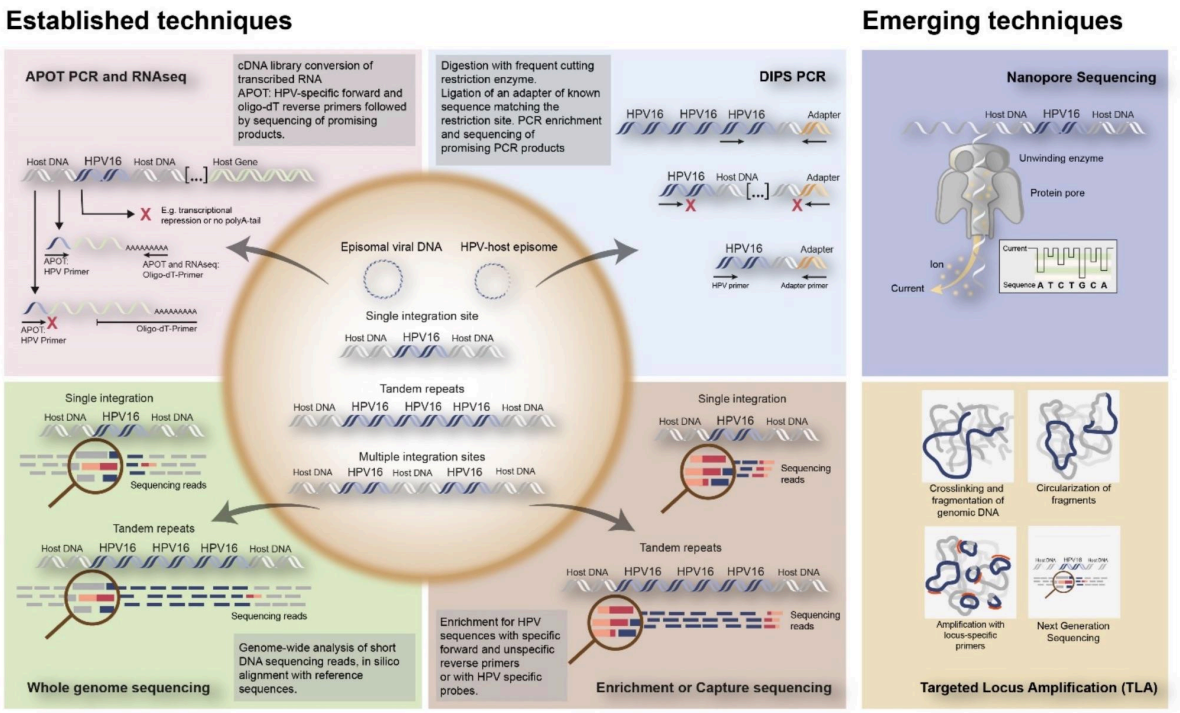

3.6.3 Targeted locus Amplification and Targeted Locus Capture

A distinctive proximity ligation-based sequencing technique, known as targeted locus amplification (TLA), was validated for identifying HPV integration sites in fresh biological samples, including cell lines. To overcome the limitations associated with formalin-fixed, paraffin-embedded (FFPE) tissues, a modified version of this technology, termed targeted locus capture (TLC), was developed. This method was originally developed for the purpose of investigating chromosomal folding (Dekker et al. 2002). The process involves formalin fixation, DNA fragmentation and ligation to concatenate DNA fragments located in proximity within the cell nucleus. The primary criterion for defining the occurrence of proximity ligation is the linear adjacency of DNA sequences located on the same chromosome. Consequently, focused amplification / capture of a specific locus (such as the integrated HPV genome) followed by NGS enables the sequencing of genomic areas extending up to hundreds of kilobases. The sequence length is determined by the sequencing depth and the

quantity of HPV genome copies, ultimately providing high-resolution information on flanking host genomic sequences. (Demers, Balaji et al., 2024).

*3.6.4 Integration and E6*I Upregulation: Contributors to Aggressive Tumour Phenotypes in OPSCC*

The implementation of NGS techniques combining host genome integration profiling with RNA expression analysis has advanced our understanding of the molecular consequences of HPV integration, including the regulation of viral isoforms such as E6*I. In this context, FFPE-TLC represents a recent methodological addition that enables high-resolution detection of integration sites directly in clinical FFPE specimens, further refining our ability to investigate the genomic landscape of HPV-driven cancers. It has been demonstrated that in a subset of HPV$^+$ OPSCCs, HPV16-E6*I which is one of the major spliced isoform of HPV16-E6 oncoprotein, is significantly upregulated in tumours with integrated HPV genomes (Huebbers et al. 2019; Leemans et al. 2011). Research findings indicate that elevated expression of this specific isoform is associated with a more aggressive clinical phenotype, including rapid disease progression. These integration-related changes influence both host and viral gene expression, highlighting the crucial role of HPV genome integration in driving tumour development and progression (Huebbers et al. 2019; Zhang et al. 2016). Besides its correlation with viral integration, elevated HPV16-E6*I expression has also been associated with an unfavourable prognosis in OPSCC and is linked to increased ROS metabolism and reprogrammed metabolic pathways. This highlights a multifaceted contribution of viral integration to oncogenic transformation (Huebbers et al. 2019).

3.7 Oxidative Stress in HPV$^+$ Tumours

3.7.1 ROS-Mediated NRF2 Activation and the Functional Role of AKR1C1 and AKR1C3 in HPV$^+$ OPSCC

Aforementioned findings provide valuable insights into the oxidative and metabolic reprogramming associated with HPV integration, particularly mediated by elevated expression of the HPV16-E6*I isoform. However, they raise important questions regarding the mechanisms by which redox homeostasis is maintained in HPV$^+$

tumours, especially in light of the distinct molecular alterations seen in HPV$^-$ HNSCC. Unlike HPV$^+$ tumours, HPV$^-$ HNSCCs frequently harbor somatic mutations in key regulators of the OS response, including NFE2L2 (encoding NRF2), KEAP1, CUL3, and RBX1, which collectively modulate the cellular antioxidant defense pathway. These mutations are often mutually exclusive and lead to the constitutive activation of the NRF2 pathway in around 25% of patients. This contributes to enhanced antioxidant defence, metabolic reprogramming and therapy resistance (Campbell et al. 2018).

The NRF2 pathway acts as a master regulator of the cellular antioxidant response. Under basal conditions, NRF2 is sequestered by KEAP1 and targeted for proteasomal degradation. Upon OS, however, NRF2 dissociates from KEAP1, translocates to the nucleus and induces the transcription of genes that protect the cell against damage, including those involved in glutathione metabolism, detoxification and redox buffering. Aberrant NRF2 activation is observed in many cancers and is closely associated with resistance to chemotherapy and radiotherapy (Penning 2017). However, these mutations are rare in HPV$^+$ HNSCC, suggesting alternative mechanisms of redox regulation in these tumours (Balaji et al. 2021).

In addition to these genetic distinctions, HPV$^-$ HNSCCs also demonstrate reduced oxidative phosphorylation (OXPHOS) activity and a pronounced shift toward glycolytic metabolism, further distinguishing their bioenergetic profile from HPV$^+$ tumours (Jung et al. 2017; Cruz-Gregorio et al. 2019). Notably, HPV$^+$ tumours frequently exhibit oxidative and metabolic stress profiles that resemble NRF2 activation despite lacking NFE2L2 mutations. This is particularly evident in tumours with integrated HPV16 genomes and correlates with overexpression of the viral HPV16-E6*I splice variant, amplification of chromosome 3q, PIK3CA mutations, and poor prognosis (Zhang et al. 2016; Huebbers et al. 2019; Leemans et al. 2011). In line with this, HPV$^+$ tumours show increased expression of canonical NRF2 target genes, including the aldo-keto reductases AKR1C1 and AKR1C3, which play a role in redox regulation (Fig. 6). There is evidence from HPV$^+$ OPSCC that HPV16-E6*I may modulate NRF2 activity, either directly or via increased ROS generation (Huebbers et al. 2019). Elevated ROS, which may arise from mitochondrial dysfunction or altered

metabolism, can stabilize NRF2 and drive the transcription of detoxifying and antioxidant enzymes, including AKR family members. AKR1C1 and AKR1C3 are of particular interest due to their dual roles in maintaining redox homeostasis and regulating steroid metabolism, prostaglandin synthesis and cell proliferation (Penning 2017). It is important to note that AKR1C1 and AKR1C3 expression serves not only as a marker of oxidative stress adaptation but also as a robust prognostic indicator and a potential therapeutic target in OPSCC (Huebbers et al. 2019). This highlights a critical link between HPV-driven oncogenesis and metabolic reprogramming.

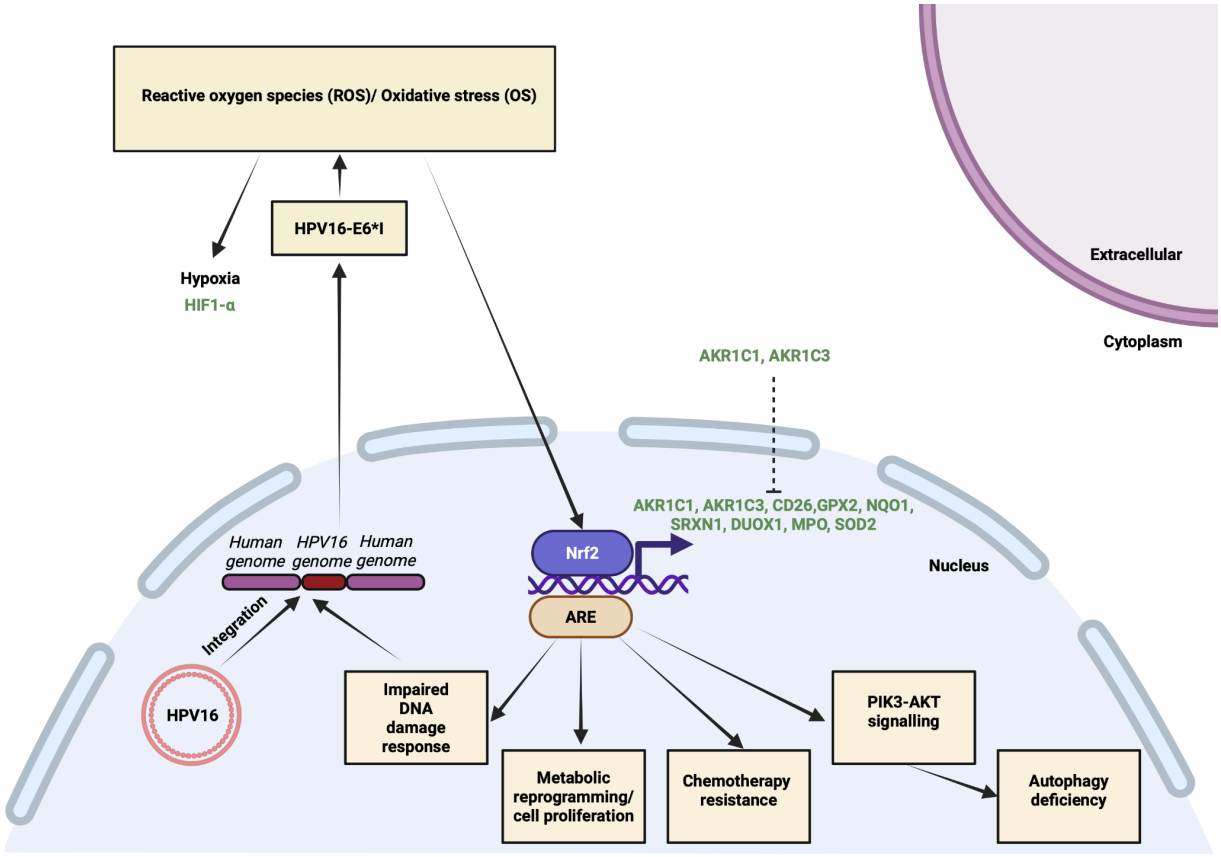

Figure 6. Proposed mechanisms connecting HPV16 genome integration and NRF2-mediated Oxidative stress (OS) response in HPV⁺ OPSCC. The integration of the HPV16 genome into the host DNA results in the overexpression of the viral splice isoform HPV16-E6*I. HPV16-E6*I promotes the generation of ROS while simultaneously activating transcription factors such as NRF2 to mitigate oxidative stress, paralleling the response observed in tobacco-induced cellular stress. This subsequently amplifies the expression of antioxidant enzymes such as AKR1C1 and AKR1C3. Activation of NRF2 also enhances the expression of NQO1 (NAD(P)H quinone dehydrogenase 1), which aids in the stabilisation of p53 by inhibiting its degradation. mRNA array analysis revealed that several NRF2-regulated OS response genes with antioxidant response elements (AREs) were increased, including CD36, DUOX1, GPX3, MPO, SOD2, and SRXN1. In HPV16 integration-positive OPSCC, it is additionally suggested that the full-length HPV16-E6 function may be diminished by its splice variant HPV16-E6*I. Recognised downstream effects of NRF2 pathway activation encompass augmented PI3K-AKT signalling, metabolic reprogramming, heightened cell proliferation, compromised

autophagy, reduced DNA damage response, and chemotherapy resistance. Modified from (Huebbers et al. 2019) using https://BioRender.com.

3.8 HPV16-E6*I as a Multifunctional Driver of HPV-Mediated Oncogenesis

As previously discussed, HPV16-E6 and HPV16-E7 are one of the key drivers of HPV-mediated carcinogenesis, degrading the tumour suppressors p53 and pRB, respectively. In addition to these well-characterised functions, the alternatively spliced HPV16-E6*I isoform has emerged as a modulator of oncogenic processes. Although HPV16-E6*I can counteract full-length HPV16-E6 and stabilise p53 under certain conditions (Vazquez-Vega et al. 2013), there is growing evidence that it plays additional, p53-independent roles in tumour progression. Proteins implicated in cell signaling, cell polarity, and tumour suppression frequently harbor PDZ domains that mediate specific protein-protein interactions. HR-HPV E6 proteins including HPV16 and HPV18 target the PDZ-domain-containing family proteins such as Discs large (Dlg), leading to their proteasome-mediated degradation. This disruption of PDZ protein networks alters cell polarity and contributes to uncontrolled cell growth. HPV16-E6 harbors a C-terminal PDZ-binding motif (PBM) that mediates interaction with Dlg. The spliced variant HPV16-E6*I retains the ability to degrade Dlg via its PBM, similarly to full-length HPV16-E6, and modulates PDZ protein function to enhance oncogenic signaling (Umnajvijit et al. 2021). These effects on polarity and signalling pathways suggest that HPV16-E6*I may influence broader regulatory networks. Notably, the E6*I from HPV18 (a variant closely related to HPV16, but with significantly weaker oncogenic potential) has been shown to upregulate Wnt/β-catenin signaling by interacting with the TCF-4 transcriptional activation complex. This suggests a potential role for E6*I in modulating key cellular pathways involved in proliferation and transformation. However, further investigation into the downstream effects of E6*I on additional components of the Wnt/β-catenin signaling cascade is necessary to clarify its specific contribution to HPV16 mediated cell transformation (Muñoz-Bello et al. 2018). In parallel, HPV16-E6*I has been shown to directly influence host cell metabolism by increasing ROS levels, impairing antioxidant responses, and promoting DNA damage (Paget-Bailly et al. 2019). In addition to modulating p53 stability, HPV16-E6*I promotes OS and induces NRF2

target genes, such as AKR1C1 and AKR1C3. This effectively mimics NRF2 activation (Wanichwatanadecha et al. 2012; Huebbers et al. 2019). These activities have been associated with chemoresistance, metabolic reprogramming and evasion of DNA damage checkpoints (Zhang et al. 2016; Penning 2017). These interconnected mechanisms, ranging from disruption of cell polarity to NRF2 pathway mimicry, including its induction of AKR1Cs expression are illustrated in Fig. 7 to provide an integrated view of HPV16-E6*I's oncogenic potential. These findings position HPV16-E6*I as a key regulator of redox adaptation and metabolic reprogramming in HPV^{+} tumours, with striking parallels to NRF2-mediated phenotypes in HPV^{-} tumours.

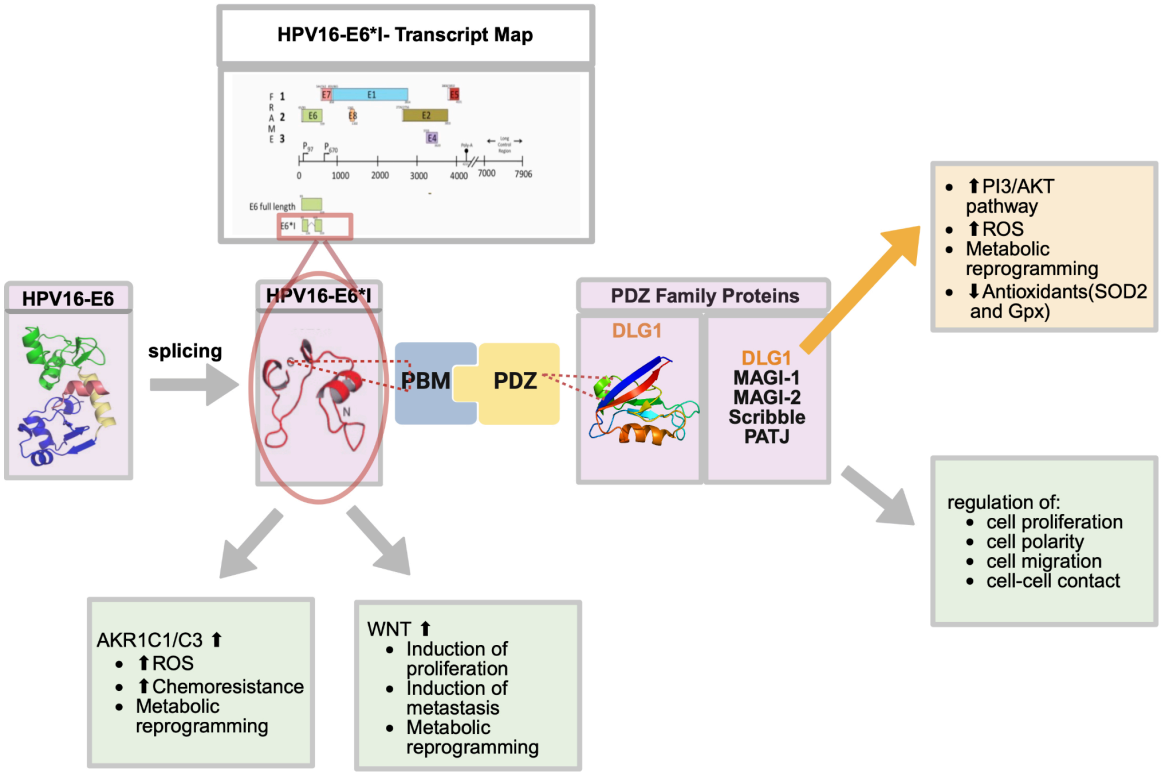

Figure 7. HPV16-E6*I, a major spliced variant of the HPV16-E6 oncoprotein, has been shown to exhibit distinct biological functions that contribute to carcinogenesis. It has been shown to antagonize full-length HPV16-E6-mediated p53 degradation, potentially stabilizing p53, while also promoting the degradation of PDZ domain-containing proteins such as Dlg via a putative PDZ-binding motif, thereby disrupting cell polarity, proliferation, migration, and cell–cell adhesion. E6*I activates Wnt/β-catenin signalling (as seen with HPV18-E6*I) and promotes OS by increasing ROS, impairing antioxidant defences, and inducing NRF2 target genes, including AKR1C1 and AKR1C3. These effects contribute to chemoresistance, metabolic reprogramming, PI3K-AKT activation, and impaired DNA damage responses, features which reflect NRF2-driven tumour phenotypes. Created in https://BioRender.com.

3.9 The Role of O_2 Concentration and Hypoxia in HPV^+ Tumour Biology

Most human tissues operate under physiological O_2 levels ("normoxia") ranging from approximately 2–7% O_2, whereas standard in vitro culture systems typically expose cells to atmospheric O_2 (~20% O_2), creating a hyperoxic artifact (Keeley and Mann 2019; Carreau et al. 2011). In contrast, solid tumours, including HPV^+ OPSCC, develop steep and dynamic O_2 gradients that result in localized hypoxia (Höckel and Vaupel 2001; McKeown 2014). While O_2 levels in healthy tonsillar tissue average around 5%, HPV^+ OPSCC often contain regions with ≤2% O_2, reflecting profound hypoxia and associated metabolic stress (McKeown 2014). O_2 tension plays a critical role in regulating ROS levels, cellular metabolism, DNA repair, and redox-responsive transcription networks. Research has shown that pathways such as HIF-1α signaling and the KEAP1–NRF2 antioxidant axis demonstrate O_2-dependent regulation, altering gene expression, cell fate, and therapy responses. In the context of HPV-associated oncogenesis, these redox-sensitive networks interact with viral oncoproteins such as HPV16-E6*I, whose function and expression may be modulated by hypoxia and ROS status (Huebbers et al. 2019; Zhang et al. 2016). Therefore, modelling both normoxic and hypoxic O_2 levels is essential to reflect the tumour microenvironment and to uncover clinically relevant mechanisms.

4 Aim of this thesis:

HPV^+ HNSCC displays distinct molecular profiles, including HPV16 host genome integration, overexpression of HPV16-E6*I, and characteristic patterns of oxidative stress (OS) and metabolic reprogramming that contribute to disease progression and therapeutic resistance. Previous research from our group identified HPV16-E6*I overexpression as a predictor of poor clinical outcome, providing the rationale for further investigation. Accordingly, this thesis explores how HPV16-E6*I expression, in the context of viral integration, promotes redox imbalance and metabolic shifts under tumour-relevant O_2 conditions. The objective is to uncover mechanistic links that may inform personalized therapeutic strategies by integrating molecular profiling with functional phenotypic analysis. The research is structured around the following aims:

1. **To investigate HPV16 integration events** in clinically relevant sample collections - applying targeted locus capture (TLA/FFPE-TLC) to map HPV16-host genomic breakpoints, structural variants, and clonality in clinical HPV^+ OPSCC specimens.
2. **To generate recombinant cell culture models overexpressing HPV16-E6*I and HPV16-E6 and perform in vitro characterisation** — establishing stable HEK 293 models followed by functional assays under tumour-relevant O_2 conditions to determine HPV16-E6*I-induced migration and proliferation.
3. **To understand the impact of HPV16-E6*I on ROS metabolism** — assessing NRF2 activation and AKR1C3 regulation at mRNA and protein levels, examining subcellular localisation, and evaluating functional effects through mitochondrial ROS measurements dependent on O_2 levels.
4. **To assess the role of HPV16-E6*I in metabolic reprogramming** — evaluating glycolysis and OXPHOS at transcript, protein, and functional levels.
5. **To establish spatial mapping of HPV16-E6/E6*I in tumour tissue** — developing isoform-specific RNA-FISH for FFPE material and integrating these results with FFPE-TLC data to correlate integration status with redox and metabolic states in situ.

5 Material and Methods

Reagents, kits, and equipment used in this study, along with their respective vendors, are listed in Table 6 and Table 7

5.1 Cell Models and Culture Conditions

5.1.1 Cell lines

5.1.1.1 Cell Lines Utilised

A number of HPV16^{+} HNSCC cell lines - including 93-VU-147T, UM-SCC-47, UD-SCC-2, UPCI-SCC152, UPCI-SCC154, UPCI-SCC090, and UM-SCC-104 - were obtained from commercial sources such as Merck Millipore and the Leibniz Institute DSMZ – German Collection of Microorganisms and Cell Cultures. Genotyping using the ProfilerPlus test revealed that each of the HNSCC cell lines (UPCI-SCC090, UPCI-SCC152, UPCI-SCC154, UD-SCC-2, UM-SCC-47, UM-SCC-104 and 93-VU-147T) possesses a unique short tandem repeat (STR) profile.

A summary of the cell lines, together with data on their clinicopathological characteristics, is provided in Table S1. For cell-based TLA, viable cells ranging from 10 - 20 × 10^6 were used (Demers, Balaji et al., 2024). CaSki and SiHa, two cervical squamous cell carcinoma (CSCC) cell lines that were positive for HPV16, were available in-house and authenticated by STR profiling. HEK 293 cells, derived from human embryonic kidney tissue and retaining wild-type p53, were likewise obtained in-house and verified through STR profiling for use as a model system in stable overexpression studies.

5.1.1.2 Cell Culture Conditions and Experimental Treatments

All cell lines were grown in a humidified environment at 37°C with 5% CO_2. HEK 293 cells were maintained in a modified version of Dulbecco’s Modified Eagle Medium

(DMEM) supplemented with 2 mM L-glutamine, 10% fetal bovine serum (FBS), and 1% penicillin-streptomycin.

All other cell lines were cultured in complete DMEM containing 2 mM L-glutamine, 1% non-essential amino acids (NEAA), 10% FBS, and 1% penicillin-streptomycin. Routine cultures were carried out under hyperoxic conditions (20% O_2). When indicated, cells were pre-conditioned for one week under either normoxic (5% O_2) or hypoxic (2% O_2) conditions to mimic the O_2 levels found in healthy tonsillar tissue and tumours, respectively. Mycoplasma contamination was routinely monitored using the MycoAlert® Mycoplasma Detection Kit. For inhibition experiments targeting AKR1C1 and AKR1C3, the specific inhibitors bromo-5-phenylsalicylic acid (5-PBSA, 2000 µM) and 3-(4-(trifluoromethyl)phenylamino)benzoic acid (20 µM) were used.

*5.1.2 Generation of stable HEK 293 cells overexpressing tagged HPV16-E6 and -E6*I*

To examine the functional impact of HPV16-E6 and -E6*I in a controlled setting, recombinant HEK 293 cell lines overexpressing HPV16-E6 and -E6*I were generated as described below. HEK 293 cells were transfected with either the pEGFP-N1 control vector, the HPV16-E6*I-HIS-GFP plasmid, or the HPV16-E6-GFP plasmid (Table 7). Transfection was performed using the Cell Line NucleofectorTM Kit C, following the manufacturer's instructions. In order to select stable clones, 500 µg/mL of G418 Sulphate was used (Ziogas et al. 2024) subsequently sorted by flow cytometry using an ID7000 analyser (Sony Biotechnology Europe in Surrey, United Kingdom; CECAD FACS facility) Non-transfected HEK 293 and HEK 293-GFP cells were used as controls in subsequent experiments.

5.1.3 Clinical samples

5.1.3.1 OPSCC Samples for FFPE-TLC Analysis and HPV Classification

Patient-derived OPSCC samples were used for comprehensive analysis of HPV host genome integration. For FFPE analysis using targeted locus capture (TLC) analysis, FFPE tissue samples were obtained from the Institute of Pathology at the University Hospital of Cologne. The samples were derived from 23 patients diagnosed with $HPV16^{+}$ OPSCC who were treated at the Department of Otorhinolaryngology, Head and Neck Surgery between 1994 and 2009. The study was approved by the Ethics Committee of the Medical Faculty at the University of Cologne (reference number 19-1288). Tumours were classified according to the World Health Organization (WHO) guidelines applicable at the time, based on HPV positivity as determined by $p16^{INK4A}$ immunohistochemistry and HPV-specific PCR. Additional selection criteria included sufficient tumour tissue and available data on HPV physical status, which had been assessed previously using DIPS-PCR (detection of integrated papillomavirus sequences by ligation-mediated PCR) (Olthof et al. 2014).

5.2 HPV Integration Analysis

This section is based on (Demers, Balaji et al., 2024).

5.2.1 Cell-based TLA

In order to validate a novel proximity ligation-based sequencing method for identifying HPV integration patterns, targeted locus amplification (TLA) was performed on HPV16 HNSCC cell lines. The cell-based TLA was carried out in accordance with the methodology outlined by (de Vree et al. 2014) (Fig. 8). In summary, the genomic DNA of live frozen cells was crosslinked with formaldehyde, and then digested with the restriction enzyme NlaIII, which recognises CATG sequences. The DNA was then purified after it had been ligated, and crosslinks were eliminated by incubating it at 80°C overnight. In order to create circular chimeric DNA molecules for the purpose of

PCR amplification, the DNA molecules were first trimmed using the restriction enzyme NspI. Subsequently, the DNA molecules were ligated at a concentration of 5 ng/µL in order to facilitate intramolecular ligation. The NspI restriction enzyme was selected because its RCATGY recognition site includes the CATG site recognized by NlaIII. Consequently, only a proportion of the CATG sites were subjected to re-digestion. Using two HPV-specific inverse primer pairs that were complementary to the E1 and E7 genes, circular DNA molecules that were about two kilobase (kb) in size and included the HPV16 sequence were completely amplified after the process of self-ligation, as described in Table S2. For the purpose of sequencing, the products obtained from four PCR reactions, each of which contained 150 ng of template in 50 µL, were combined. Both the preparation of Illumina NGS libraries and the 151-base pair (bp) paired-end sequencing of TLA libraries were carried out on Illumina platforms. The preparation of Illumina NGS libraries was carried out in accordance with the methodology provided by the manufacturer by Nextera™ DNA FLEX Library Preparation Kit.

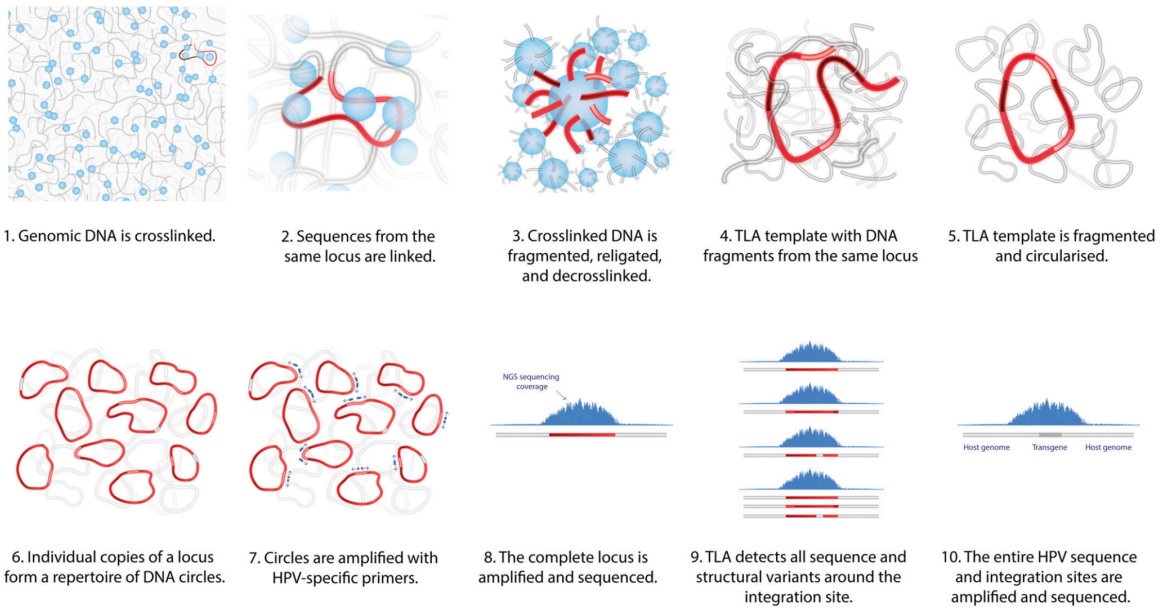

Figure 8. The cell-based TLA workflow is depicted in a schematic overview. The genomic DNA of viable frozen cells is crosslinked, a process that occurs most efficiently between sequences in close physical proximity (1). Crosslinks are indicated by blue circles. These sequences, represented by various shades of red, are linked together as a consequence of crosslinking (2). The DNA that has been crosslinked is first fragmented, then religated, and finally decrosslinked using the NlaIII restriction enzyme (3). This results in the establishment of a TLA template, which consists of extended lengths of

DNA comprising DNA fragments originating from the same locus (4). To create a circle of approximately 2 kb, this TLA template is first fragmented using the NspI restriction enzyme, and then self-ligated. A repertory of DNA circles is produced as a result of the random diversity that occurs in the folding, crosslinking, and religation of DNA fragments in individual copies of a locus (6). Inverse primers complementary to the HPV16 sequence are used to amplify DNA circles originating from the locus of interest, i.e. the HPV integration site (7). Consequently, the entire DNA circle, along with the HPV integration site, is amplified, enabling the use of NGS technology for sequencing (8). Therefore, TLA technology facilitates hypothesis-free sequencing in a targeted manner. In the loci of interest, it is able to identify all of the sequences and structural variations as well (9). Using primers that are specific to the HPV16, the whole genome of the HPV virus, as well as the sequences of the human genome that flank the integration site (which are included in the DNA circles), are amplified and sequenced (10).

5.2.2 FFPE-TLC

To investigate HPV integration patterns in patient tissues, a modified approach of TLA, (TLC, targeted locus capture) was applied to FFPE specimens, as detailed below. The FFPE-TLC procedure was performed according to the methodology described by (Allahyar et al. 2021) (Fig. 9). For each patient, 3–4 FFPE sections (4 µm thick) mounted on Superfrost™ Plus microscope slides were promptly scraped and transferred to vials containing 1.5 mL of buffer. After heat treatment and centrifugation, the paraffin layer was removed. Tissue disruption and homogenization were carried out by sonication using an M220 Focused-ultrasonicator (Covaris Ltd., Brighton BN2 6AH). Samples were then permeabilized, followed by digestion with the NlaIII restriction enzyme and subsequent ligation. For validation purposes, seven samples were subjected to random DNA digestion using an endonuclease, without prior sonication. DNA purification was performed after overnight de-crosslinking at 80 °C. Following elution, 100 ng of DNA was fragmented to a size of 200–300 bp and used to construct next-generation sequencing libraries using the Roche KAPA HyperPrep Kit and the KAPA Unique Dual-Indexed Adapter Kit. Twenty individually prepared libraries (totaling 2 µg DNA) were pooled and hybridized with a capture probe set targeting HPV16 and HPV18 (Table S3). Subsequently, magnetic bead separation and amplification were performed. Paired-end sequencing (2 × 151 bp) was carried out on Illumina platforms. Table 1 summarizes the key differences between the cell-based TLA protocol and the FFPE-TLC method.

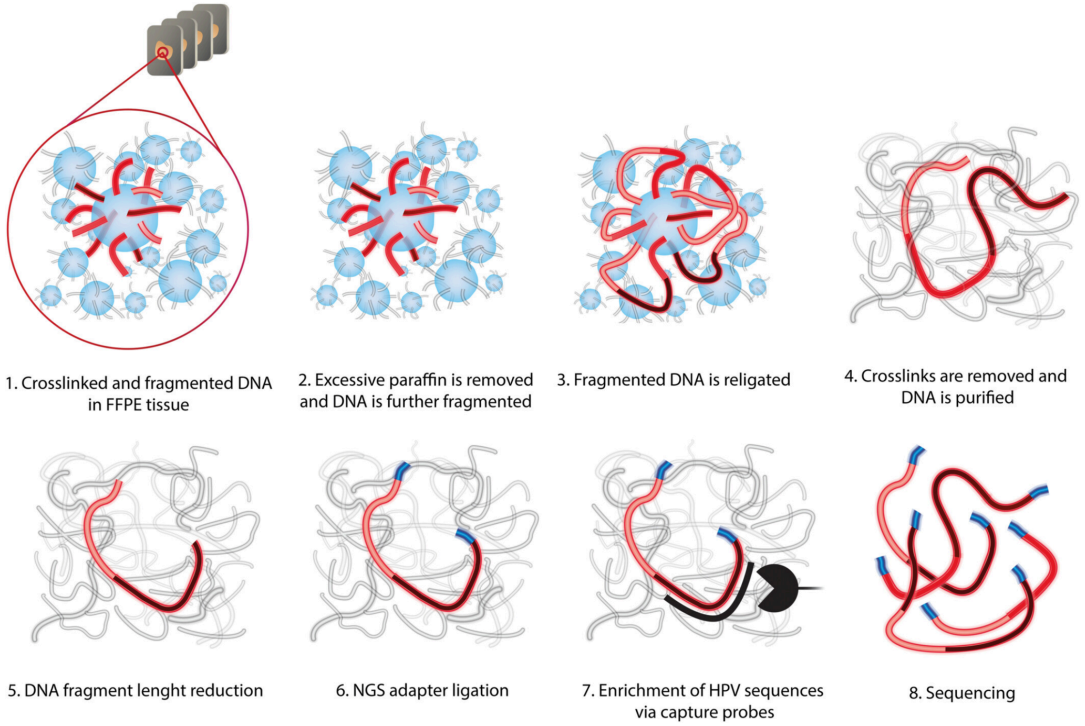

Figure 9. A graphical overview of the FFPE-TLC procedure / method. During the process of tissue fixation, sequences that are physically close together are crosslinked in a preferred manner (1). The sample is then permeabilized once the paraffin has been removed, which makes it possible for the NlaIII restriction enzyme to continue fragmenting the DNA (2). Religation of the DNA (3), removal of crosslinks, and purification of the DNA are the steps involved (4). After that, the DNA is put through the process of NGS library preparation, which includes DNA fragment length reduction from (5) and NGS adaptor ligation (6). Combining hybrid capture probes that are complementary to the HPV sequence (7) allows for the enrichment of HPV integration sites. After that, the library that has been created is amplified, and then it is sequenced using paired-end sequencing equipment from Illumina (8).

Table 1: Comparison of TLA and FFPE-TLC methodologies

	TLA	**FFPE-TLC**
Crosslinking of DNA	DNA is crosslinked using formaldehyde	Crosslinking is already established during the fixation of tissue samples
Fragmentation of DNA	DNA is digested using restriction enzymes NlaIII and NspI	Fragmentation is performed using the NlaIII enzyme

	TLA	FFPE-TLC
Proximity ligation result	Produces circular DNA molecules approximately 2 kb in size	Results in linear DNA fragments ranging from 200 to 300 bp
Enrichment of HPV	Performed using PCR with primers targeting HPV sequences	Achieved by capturing with full-length HPV-specific probes before amplification

2.2.3 Mapping and alignment

The sequencing data from both TLA and FFPE-TLC was processed using computer algorithms to map it and align it to the human reference genome, as demonstrated below. The custom TLA analysis pipeline utilised the BWA mapping software to align reads generated from cell-based TLA and FFPE-TLC experiments to the human reference genome (hg19). Two versions of the aligner were used: The BWA-SW v0.7.15-r1140 was executed with the setting 'bwasw -b 7, and the BWA-MEM v0.7.17-r1188 was executed with the setting 'bwa mem -b 7 (Allahyar et al. 2021). Both aligners support the "split-mapping" technique, which enables a single read containing multiple DNA fragments to be mapped to different genomic locations.

5.2.4 Identification of breakpoint

The identification of breakpoints, defined as junctions between the viral and host chimeric reads, was carried out using both a manual inspection of the human genome coverage profile and automated identification of HPV16-human breakpoint sequences. If split-alignments were available, they were gathered for the latter method. Split-alignments refer to individual read sequences that have been mapped to both the human genome and the genome of the virus. Split alignments that joined precisely at the restriction-enzyme recognition site (CATG) were excluded, thereby

removing the ligation-induced breakpoints. Given that the portion of the sequence that corresponds to the human genome exceeds 10 bp in length, it was revealed that HPV16-human breakpoint sequences were present in >1% percent of the readings at the site of the fusion. Concurrently, a visual inspection of the breakpoint sequence was conducted in an NGS data browser to eliminate sequencing artefacts, such as breakpoints located in hairpin structures or low-complexity areas.

5.2.5 Validation of integration sites by PCR

To validate the integration sites identified by TLA/FFPE-TLC, PCR was performed on selected integration events in HNSCC cell lines and in a subset of 7 OPSCC patient samples. Case selection was based on the availability of suitable tissue material and prior integration analysis results. Based on data from DIPS-PCR and/or TLA/FFPE-TLC, primers were designed to target viral-human fusion sites of 100–150 bp in length (Table 8). DNA from the HNSCC cell lines 93-VU-147T, UPCI:SCC090, UPCI:SCC152, UPCI:SCC154, UD-SCC-2, and UM-SCC-47 was extracted using the QIAamp DNA Micro Kit. For FFPE-derived OPSCC samples, DNA extraction was performed using the QIAamp DNA FFPE Advanced UNG Kit, following the manufacturer's instructions. PCR amplification was conducted using 500 ng of input DNA. A temperature gradient ranging from 50°C to 60°C was applied during the annealing step to determine the optimal annealing temperature for each primer pair. PCR products were purified and subsequently analyzed by Sanger sequencing. Electrophoresis on 3% agarose gels was used to assess the PCR products.

5.3 Gene Expression Analysis

5.3.1 RT-PCR Analysis

HEK 293, HEK 293-GFP, -GFP-E6, and -GFP-His-E6*I cell lines were exposed to the O_2 conditions described in Section 2.1.1.2. The RNeasy Mini Kit was used to extract total RNA in accordance with the established procedure provided by the manufacturer. The RNA concentration was quantified using the 4150 TapeStation System from Agilent Technologies with the RNA ScreenTape assay. The iScriptTM cDNA synthesis kit was used to reverse transcribe 500 µg of RNA into cDNA. The process was carried out in accordance with the instructions provided by the manufacturer. RT-PCR was carried out using the CFX96 equipment from Bio-Rad Laboratories GmbH and the iTaq Universal SYBR Green Supermix in accordance with the instructions provided by the manufacturer. The housekeeping gene HPRT-1 was used for internal normalization (Olthof et al. 2014). A comprehensive list of the primer sequences is provided in Table 8. The $2^{-\Delta\Delta Ct}$ method was used to determine mRNA expression levels.

5.3.2 ddPCR Analysis

This study aimed to investigate changes in gene expression resulting from the overexpression of HPV16-E6/-E6*I under varying O_2 concentrations in the HEK 293 cell culture models. To enable precise quantification and reliable comparison across experimental conditions including different O_2 levels, droplet digital PCR (ddPCR) was employed using cDNA synthesized as described in Section 5.3.1. All reagents and instrumentation were obtained from Bio-Rad Laboratories GmbH. Reaction mixtures were prepared using ddPCR Supermix for Probes (No dUTP), along with the cDNA template, appropriate controls, and custom designed probes targeting the genes of interest, as detailed in Table 9.

Table 2: Reaction mix setup for ddPCR using Supermix for Probes (No dUTP)

Component	Volume	Final Concentration
2x ddPCR Supermix (No dUTP)	10 µL	1x
20x target probe (FAM)	1 µL	250 nM
20x reference probe (HEX)	1 µL	250 nM
Sample cDNA	variable	500 ng
RNase-/DNase-free water	to 20 µL	

The reaction components were thoroughly mixed in a tube before being transferred to a DG8™ Cartridge. 70 µl of Droplet Generation Oil were loaded into the designated oil wells, the cartridge was sealed with a gasket, and placed into the QX200™ Droplet Generator according to the manufacturer's instructions. This process partitioned the reaction mixture into approximately 20,000 uniform nanoliter-sized droplets per sample. The generated droplets were then transferred to a PCR plate, sealed with pierceable foil using the PX1™ Plate Sealer, and subjected to thermal cycling in a C1000 Touch Thermal Cycler, following the cycling conditions specified in Table 3.

Table 3: Thermal Cycling protocol used for ddPCR

Step	Temp (°C)	Time	Cycles
Enzyme activation	95	10 minutes	1
Denaturation	94	30 seconds	40
Annealing/Extension	60	1 minutes	40
Enzyme deactivation	98	10 minutes	1
Final hold	4	–	1

The generated droplets were analyzed using the QX200™ Droplet Reader based on fluorescence intensity. QuantaSoft™ software classified each droplet as positive or negative and calculated the target copy/µL of reaction mixture.

5.4 Protein Expression and Functional Assessment

5.4.1 Western blot Analysis

To complement the gene expression data and assess corresponding protein-level changes, Western blot analysis was performed on cell lysates prepared from HEK 293 cell culture models exposed to different O_2 conditions, as previously described. Proteins were extracted from cell pellets using 1× RIPA lysis buffer. DNA was sheared by sonication (Diagenode Bioruptor® Plus) at high power in 30-second on/off cycles, repeated 5–10 times. This was followed by centrifugation at 16,000 x g at 4°C for 15 minutes. Protein concentrations were determined using the Pierce™ BCA Protein Assay Kits. For electrophoresis, 25 µg of total protein per sample was mixed with 4× Laemmli Sample Buffer freshly supplemented with 10% β-mercaptoethanol and loaded onto 10% Criterion™ TGX™ Precast Midi Protein Gels (26-well). Gel electrophoresis was performed in a Criterion™ cell system at 200 V. Proteins were transferred to 0.2 µm nitrocellulose membranes using the Trans-Blot Turbo Midi Nitrocellulose Transfer Packs and the Trans-Blot Turbo Transfer System under semi-dry conditions. Membranes were blocked with EveryBlot Blocking Buffer and subsequently incubated overnight with primary antibodies of interest at 4°C (Table 8). After washing, membranes were incubated with the appropriate secondary antibodies for 1 hour at room temperature (Table 8). Protein detection was performed using Clarity™ Western ECL Substrate, and bands were visualized with the ChemiDoc™ Imaging System, and intensities were quantified using Image Lab Software.

5.4.2 Wound Healing Assay

To investigate the functional effects of varying O_2 levels on cell proliferation and migration, wound healing assays were performed using HEK 293 cell culture models under the different O_2 conditions described previously. Cells were seeded into Culture-Insert 2 Well 24 devices at a density of 1×10^6 cells/mL in a volume of 70 µL per insert, with four replicates per cell line. After careful addition of 500 µL of complete culture medium to each well, cells were incubated overnight under the designated O_2 conditions and allowed to grow to confluence. The 2-well inserts were

then gently removed using autoclaved tweezers to avoid disrupting the monolayer and to ensure a uniform cell-free gap. Cells were maintained under the respective O_2 conditions during the migration phase. Live-cell imaging was conducted every 30 minutes using a Zeiss AxioObserver, Carl Zeiss microscope equipped with O_2 control and an automated stage. Wound closure was quantified by measuring the reduction in gap area over time using ImageJ (Fiji®) with the “Wound Healing Size Tool” plugin (Suarez-Arnedo et al. 2020).

5.5 Oxidative Stress and Metabolic Reprogramming Profiling

5.5.1 Immunofluorescence Assay of ROS Biomarkers

To visualize subcellular localization and quantify the expression of ROS-related proteins in HEK 293 cell culture models overexpressing HPV16-E6 or -E6*I under different O_2 conditions, immunofluorescence assays were performed. As previously described, HEK 293 cell cultures were exposed to varying O_2 concentrations and subsequently seeded at a density of 6 x 10^4 cells/mL in 8-well detachable chamber slides in accordance with the manufacturer's protocol. After 24 hours of incubation, cells were thoroughly washed with PBS and fixed with 4% paraformaldehyde for at least 20 minutes, followed by PBS rinses, twice. Permeabilization was performed using 0.5% Triton X-100, after which cells were rinsed again with PBS and blocked with 1% FBS. Antibodies (Table 8) were applied and incubated overnight at 4 °C. Following incubation, cells were washed 5 times with PBS (5 minutes per wash) under continuous agitation. Secondary antibodies (Table 8) were diluted in blocking buffer and incubated for 1 hour at room temperature, according to the manufacturer's recommendations. After a final 5-minute rinse with distilled water, the chamber walls were removed and cells were mounted with coverslips using ProLong™ Glass Antifade Mountant with NucBlue™ nuclear stain. Confocal imaging was performed using the Zeiss LSM 980 Airyscan2, Carl Zeiss confocal microscope. Laser settings were optimized for the brightest signal in each channel and kept constant across all samples to ensure reliable quantification.

5.5.2 MitoSox Analysis

Given the critical role of oxidative stress in the cellular response to HPV16-E6/-E6*I expression, MitoSOX assays were performed to detect mitochondrial superoxide production under the different experimental O_2 conditions. Cells were seeded at a density of 1 × 10^5 cells/mL into black 96-well plates with a transparent bottom, pre-coated with Corning® Cell-Tak™ Cell and Tissue Adhesive. As described previously, the experiments were conducted under varying O_2 concentrations. Following seeding, the plates were incubated for 12 hours under their respective O_2 conditions. After this initial incubation, to assess mitochondrial superoxide levels, cells were stained with MitoSOX™ Red Mitochondrial Superoxide Indicator, prepared according to the manufacturer's instructions. A 5 mM stock solution was prepared by dissolving the contents of a 50 µg vial in 13 µL of anhydrous dimethyl sulfoxide (DMSO), and used the same day to ensure reagent stability. The working solution was prepared by diluting 5 µL of stock into 50 mL of Hank's Balanced Salt Solution (HBSS) supplemented with calcium and magnesium, resulting in a final staining concentration of 500 nM. Cells were incubated with the dye for 30 minutes at 37 °C in a humidified atmosphere containing 5% CO_2 at their respective O_2 concentrations, protected from light. Following incubation, cells were gently washed three times with prewarmed HBSS to remove excess dye prior to analysis. Following the staining and washes, fluorescence intensity, reflecting mitochondrial superoxide levels, was measured using a Clariostar plate reader, BMG LABTECH with excitation/emission wavelengths of 510 nm / 580 nm. To normalize for cell number, Hoechst 33342 staining was performed using the same plate reader, with fluorescence detected at 350 nm / 461 nm, as its nuclear fluorescence correlates with DNA content. Additionally, stained samples were fixed with 4% paraformaldehyde, mounted using ProLong™ Glass Antifade Mountant with NucBlue™, and examined by Zeiss AxioObserver, Carl Zeiss fluorescence microscope. This was done to assess the localization of staining.

5.5.3 Seahorse Analysis for Cellular Metabolic Profiling

To assess metabolic activity under hyperoxic conditions, cellular respiration and glycolysis were analyzed using the Seahorse XF Cell Mito Stress Test on a Seahorse XFe96 Analyzer, Agilent Technologies. Oxygen consumption rate (OCR) and extracellular acidification rate (ECAR) were measured as indicators of mitochondrial respiration and glycolytic function, respectively. Due to technical limitations preventing measurements under reduced O_2 conditions, this assay was performed exclusively under hyperoxia to identify key metabolic pathways for further investigation. In parallel, subsequently, cells were counted and seeded at a density of 2×10^5 cells/mL in standard growth medium into Seahorse XFe96 cell culture microplates pre-coated with Corning® Cell-Tak™ Cell and Tissue Adhesive. Following a 4 hour incubation at 37°C to allow for cell adherence, the medium was replaced with Seahorse XF assay medium (Agilent Technologies), adjusted to pH 7.4 and supplemented with 10 mM glucose, 2 mM pyruvate, and 2 mM glutamine. Cells were then incubated for an additional 60 minutes in a non-CO_2 incubator to allow metabolic equilibration. During the assay, sensor cartridges were pre-hydrated overnight using Seahorse XF Calibrant. The following compounds were injected sequentially via the cartridge ports at the indicated final concentrations listed in Table 4.1.

Table 4.1: Final Concentrations of Mitochondrial Stress Compounds Used in Seahorse XF Assay

Compound	Function	Final Concentration
Oligomycin	ATP synthase inhibitor	1.5 µM
FCCP (Carbonyl cyanide-p-trifluoromethoxyphenylhydrazone)	Mitochondrial uncoupler	2.5 µM
Rotenone/Antimycin A	Complex I and III inhibitors	1.5 µM

After data acquisition, measurement cycles were conducted at 37°C and consisted of mixing, waiting, and measurement phases, following the manufacturer's protocol. Real-time OCR and ECAR were recorded throughout the assay. Finally, to normalize OCR and ECAR values to cell number, nuclei were stained post-assay with Hoechst 33342. Fluorescence intensity was measured using a Clariostar plate reader (BMG LABTECH GmbH) under the settings detailed in Table 4.2.

Table 4.2: Hoechst Fluorescence Measurement Parameters

Parameter	Value
Excitation Wavelength	355 ± 10 nm
Emission Wavelength	455 ± 15 nm
Detector Gain	1400
Focus Offset	2.1 mm
Measurement Temperature	37°C

Finally, mitochondrial respiration and glycolytic activity were analyzed using Seahorse Wave software (Agilent Technologies). OCR and ECAR values were normalized to cell number based on Hoechst fluorescence intensity, as described above, using the software's built-in normalization function.

5.5.4 Metabolic Profiling by Plate Reader Assays: Assessment of ATP Content, Glucose Uptake, and Lactate Production

To supplement the Seahorse-based real-time metabolic flux analysis, additional endpoint metabolic assays were performed using a plate reader platform to quantify intracellular ATP levels, glucose uptake, and lactate production.

5.5.4.1 Cells preparation and plating

HEK 293 cell culture models were seeded in triplicate into white, opaque 96-well plates pre-coated with Corning® Cell-Tak™ Cell and Tissue Adhesive, at a density of 1×10^4 cells/well in 100 µL of complete culture medium. Cells were allowed to adhere overnight under standard culture conditions (37 °C, 5% CO_2) at the O_2 concentrations described previously. The seeding density was optimized to ensure that the luminescence signals remained within the linear detection range for each assay, as confirmed by preliminary titration experiments.

5.5.4.2 ATP Content Measurement

Intracellular ATP levels were quantified using the CellTiter-Glo® Luminescent Cell Viability Assay, following the manufacturer's protocol. To prepare the CellTiter-Glo® Reagent, the lyophilized substrate was reconstituted with the supplied buffer according to the instructions. Prior to the assay, cell culture medium was carefully aspirated from each well of a 96-well plate to avoid disturbing the adherent cells. Subsequently, 100 µL of fresh complete culture medium was added to each well, followed by 100 µL of CellTiter-Glo® Reagent. The plate was placed on an orbital shaker for 2 minutes to ensure complete cell lysis, then incubated at room temperature for 10 minutes to allow luminescent signal stabilization. Luminescence was measured using a CLARIOstar®, BMG LABTECH plate reader with an integration time of 1 second per well. Orbital averaging (circular scanning) was applied to minimize well-to-well variability and improve signal accuracy. The resulting luminescent signal is directly proportional to the intracellular ATP concentration.

5.5.4.3 Glucose Uptake Assay

Glucose uptake was measured using the Glucose Uptake-Glo™ Assay, following the manufacturer’s instructions. After treatment, the culture medium was carefully aspirated, and cells were washed once with 100 µl of PBS to remove residual glucose. Cells were then incubated in PBS containing 50 µl of 1 mM 2-deoxyglucose

(2DG) at room temperature for 10 minutes. To terminate glucose uptake, 25 µL of Stop Buffer was added, followed immediately by 25 µL of Neutralization Buffer. Finally, 100 µl of the freshly prepared 2DG6P Detection Reagent was added to each well. The plate was incubated at room temperature for 1 hour, after which luminescence was measured using a CLARIOstar®, BMG LABTECH plate reader with an integration time of one second per well. Orbital averaging (circular scanning) was utilized to reduce well-to-well variability and improve signal accuracy.

5.5.4.3 Lactate Production Assay

Extracellular lactate production was measured using the Lactate-Glo™ Assay (Promega) in accordance with the manufacturer's instructions. Following the designated incubation period under experimental conditions, the culture medium was carefully removed by pipetting from each well of the 96-well plate. Cells were washed with 100 µL of PBS to eliminate any residual glucose. 50 µl of Lactate Detection Reagent were added directly to each well to commence the detection process. The plate was then incubated at room temperature for 60 minutes to allow the development of the luminescence signal. The process of detection was initiated by adding 50 µL of Lactate Detection Reagent directly to each well. The plate was then left at room temperature for 1 hour. Luminescence was recorded using a CLARIOstar®, BMG LABTECH plate reader with an integration time of 1 second per well. Orbital averaging (circular scanning) was used to minimize well-to-well variability. Luminescence intensity is directly proportional to the amount of extracellular lactate, providing a reliable measure of glycolytic activity.

5.6 Tissue-Level Protein and RNA Detection

5.6.1 LNA-RNA FISH

to detect and quantify HPV16-E6*I expression in FFPE patient samples, LNA-RNA fluorescence in situ hybridization (FISH) was employed. Elevated levels of HPV16-E6*I have been functionally associated with HPV host genome integration,

increased ROS metabolism, metabolic reprogramming, and unfavourable prognosis in OPSCC. This method enables spatial mapping of viral transcript expression and links molecular phenotype to integration status. Regarding probe design, locked nucleic acids (LNA) are high-affinity RNA analogs characterized by modified ribose rings that confer enhanced thermal stability when hybridized to complementary sequences. Each incorporated LNA monomer increases the melting temperature (Tm) of a duplex by approximately 2–8 °C. LNA oligonucleotides are typically shorter than conventional probes, offering high specificity and sensitivity, particularly for short or spliced RNA targets. Their tunable composition (LNA + DNA/RNA) makes them well-suited for detection of transcripts like HPV16-E6*I. Initially, sections (4 µm) of paraffin-embedded UD-SCC2 cell block material were prepared using Profcontrol GmbH, microtome and mounted on Superfrost™ Plus microscope slides for cell adhesion. The UD-SCC2 cell line was selected for standardising the RNA-FISH protocol, as mRNA analysis demonstrated increased expression of both HPV16-E6 and -E6*I transcripts. All reagents were freshly prepared, and RNase-free conditions were maintained throughout. Deparaffinization was performed according to the steps listed in Table (5.1).

Table 5.1: Deparaffinization and Rehydration Steps

Step	Reagent/Condition	Duration
Deparaffinization	100% Roti®-Histol	2 x 5 minutes
Rehydration	100% Ethanol	10 minutes
	90% Ethanol	5 minutes
	70% Ethanol	5 minutes
Rinse	RNase-free distilled water	5 minutes

After rehydration, permeabilization and digestion steps were performed as outlined in Table 5.2.

Table 5.2: Permeabilization and Enzymatic Digestion

Step	Reagent/Condition	Duration	Temperature
Permeabilization	0.5% SDS	15 minutes	Room temperature
Wash	RNase-free distilled water	Thorough rinse	Room temperature
Enzymatic Digestion	0.2% Pepsin	15 minutes	37 °C
Stop Digestion	0.1 M Glycine in PBS (×2)	2 × 3 minutes	Room temperature
Final Wash	PBS	5 minutes	Room temperature

Following permeabilization, a hydrophobic barrier was drawn around each section using a Liquid Barrier Marker. DNase I (50 U/mL; Roche Diagnostics GmbH) was applied to the section with a hydrophobic barrier to degrade DNA and enable RNA-specific detection. Samples were incubated for 1 hour at 37 °C. For pre-hybridization, the buffer was freshly prepared according to Table 5.3.

Table 5.3: Pre-Hybridisation Buffer

Component	Volume (µL)
Formamide	500
20X SSC	100
0.5 M Sodium phosphate buffer ((1:1): NaH_2PO_4 and Na_2HPO_4)	100
10% SDS	50
50 mM EDTA	20
Salmon sperm DNA	3

Component	Volume (µL)
RNase-free water	227
Total	1000

Immediately beforehand, the Pre-Hybridisation mixture was heated to 95 °C for 2 minutes, and ~150 µL of the Pre-Hybridisation mixture was applied per section. Slides were then incubated at 90 °C for 2 minutes, followed by incubation at room temperature (humidified chamber) for 1–2 hours without washing. For probe hybridization, the hybridization mixture was denatured at 95 °C for 2 minutes. Approximately 150 µL was applied per section. Hybridization was performed overnight at 42 °C in the dark using 1 µL of fluorophore-labeled LNA probe (10 µM, Table 5.4) diluted in 250 µL of hybridization buffer.

Table 5.4: LNA Probes Used for RNA-FISH

Probe Name	Sequence (5′–3′)	Modification
E6SI (HPV16-E6*I)	/5TYE665/ATACACCTCACTGCGAATACT	5′-TYE665
E6FULL (HPV16-E6)	/5TYE563/ATCTCTATATACATGCATA	5′-TYE563
BETA-ACTIN (positive-contro)	/5TYE665/CTGATCTGAGAGGGTGTGTGCCCA	5′-TYE665
SCRAMBLE-ISH (negative-contro)	/5TYE665/GTGTAAGGCCTGTAAGCCCA	5′-TYE665

Finally, post-hybridisation washes were conducted as described in Table (5.5). Slides were mounted using ProLong™ Glass Antifade Mountant with NucBlue™ and imaged using Zeiss AxioObserver, Carl Zeiss fluorescence microscope.

Table 5.5: Wash Steps

Wash Step	Buffer	Duration	Temperature
Wash 1	2X SSC	15 minutes × 2	42 °C
Wash 2	1X SSC	15 minutes	42 °C
Wash 3	0.5X SSC	15 minutes	42 °C

5.7 Statistics

Statistical analyses were performed to assess the significance of differences observed across experimental groups. Clinicopathological data were analysed using cross-tabulation methods, including Pearson's chi-squared and Fisher's exact tests, as appropriate. These analyses were conducted using SPSS Statistics for Mac, version 28.0.1.0 (IBM Corp., Armonk, NY, USA). Additional statistical analyses were performed using GraphPad Prism, version 6.0 (GraphPad Software, La Jolla, CA, USA). Differences between experimental groups were evaluated using two-way analysis of variance (ANOVA), followed by Tukey's post hoc test for multiple comparison. A p-value of <0.05 was considered statistically significant. All experimental procedures were independently repeated, with each experiment performed in biological duplicates (ddPCR as recommended by the manufacturer) or triplicates (all other experiments).

5.8 Data availability

All datasets generated or analysed during this study, including both raw and processed data (e.g. imaging and sequencing files), are securely stored on servers of the University of Cologne. Detailed descriptions of data processing and analysis procedures are provided in the “2 Materials and Methods” section. Custom macros used for analyses are archived on the same server infrastructure. Information

regarding laboratory protocols followed during the experiments is documented in the eLabJournal system.

5.9 List of Reagents, Equipment, Antibodies, and Plasmids

Table 6: Comprehensive List of Reagents and Kits Used in Cell Culture, Molecular, and Imaging Assays

Reagent	Company / Distributor (location)	Concentration
DMEM	Thermo Fisher Scientific (Schwerte, Germany)	—
L-Glutamine	Thermo Fisher Scientific (Schwerte, Germany)	2 mM
Fetal Bovine Serum (FBS)	Pan-Biotech (Aidenbach, Germany)	—
Penicillin-Streptomycin	Pan-Biotech (Aidenbach, Germany)	—
Non-essential amino acids (NEAA)	Thermo Fisher Scientific (Schwerte, Germany)	—
MycoAlert® Mycoplasma Detection Kit	Lonza GmbH (Cologne, Germany)	—
5-PBSA (bromo-5-phenylsalicylic acid)	Sigma-Aldrich Chemie GmbH (Taufkirchen, Germany)	2000 mM
3-(4-(trifluoromethyl)phenyl-amino)-benzoicacid	Sigma-Aldrich Chemie GmbH (Taufkirchen, Germany)	20 µM
Cell Line Nucleofector™ Kit C	Lonza GmbH (Cologne, Germany)	—
G418 Sulphate	Sigma-Aldrich Chemie GmbH (Taufkirchen, Germany)	500 µg/mL
Agarose	Sigma-Aldrich Chemie GmbH Taufkirchen, Germany)	3 % (w/v)
Sanger Sequencing Service	Eurofins Genomics Europe Shared Services GmbH (Ebersberg, Germany)	—
RNeasy Mini Kit	Qiagen GmbH (Hilden, Germany)	—
RNA ScreenTape Analysis	Agilent Technologies Deutschland GmbH (Waldbronn, Germany)	—
iScript™ cDNA Synthesis Kit	Bio-Rad Laboratories GmbH (Feldkirchen, Germany)	—
iTaq™ Universal SYBR Green Supermix	Bio-Rad Laboratories GmbH (Feldkirchen, Germany)	—

Reagent	Company / Distributor (location)	Concentration
ddPCR Supermix for Probes (No dUTP)	Bio-Rad Laboratories GmbH (Feldkirchen, Germany)	—
Droplet Generation Oil	Bio-Rad Laboratories GmbH (Feldkirchen, Germany)	—
10× RIPA Lysis Buffer	Sigma-Aldrich Chemie GmbH (Taufkirchen, Germany)	1×
Pierce™ BCA Protein Assay Kit	Thermo Scientific™ (Dreieich, Germany)	—
4× Laemmli Sample Buffer	Bio-Rad Laboratories GmbH (Feldkirchen, Germany)	—
β-Mercaptoethanol	Sigma-Aldrich Chemie GmbH (Taufkirchen, Germany)	—
Criterion™ TGX™ Precast Midi Protein Gel (26-well)	Bio-Rad Laboratories GmbH (Feldkirchen, Germany)	10 %
Trans-Blot Turbo Midi Nitrocellulose Transfer Packs	Bio-Rad Laboratories GmbH (Feldkirchen, Germany)	0.2 µm
EveryBlot Blocking Buffer	Bio-Rad Laboratories GmbH (Feldkirchen, Germany)	—
Clarity Western ECL Substrate	Bio-Rad Laboratories GmbH (Feldkirchen, Germany)	—
2 Well 24 Culture Insert	Ibidi GmbH (Gräfelfing, Germany)	—
8-Well Detachable Chambers	Ibidi GmbH (Gräfelfing, Germany)	—
4 % Paraformaldehyde	Sigma-Aldrich Chemie GmbH (Taufkirchen, Germany)	4 %
Triton X-100	Carl Roth GmbH + Co. KG (Karlsruhe, Germany)	0.5 %
ProLong™ Glass Antifade Mountant with NucBlue™	Invitrogen, Fisher Scientific (Schwerte, Germany)	—
Corning® Cell-Tak™ Cell & Tissue Adhesive	Fisher Scientific (Schwerte, Germany)	—
Dimethyl Sulfoxide (DMSO, anhydrous)	Sigma-Aldrich Chemie GmbH (Taufkirchen, Germany)	—
Hank's Balanced Salt Solution (HBSS)	Invitrogen, Fisher Scientific (Schwerte, Germany)	—

Reagent	Company / Distributor (location)	Concentration
MitoSOX™ Red Mitochondrial Superoxide Indicator	Thermo Scientific™ (Dreieich, Germany)	500 nM
Hoechst 33342	Thermo Scientific™ (Dreieich, Germany)	—
Seahorse XF Base Medium	Agilent Technologies Deutschland GmbH (Waldbronn, Germany)	—
Seahorse XF Cell Mito Stress Test Kit	Agilent Technologies Deutschland GmbH (Waldbronn, Germany)	—
XF Calibrant	Agilent Technologies Deutschland GmbH (Waldbronn, Germany)	—
Seahorse XFe96 / XF Pro FluxPak Mini	Agilent Technologies Deutschland GmbH (Waldbronn, Germany)	—
Glucose (Seahorse supplement)	Agilent Technologies Deutschland GmbH (Waldbronn, Germany)	10 mM
Sodium Pyruvate	Agilent Technologies Deutschland GmbH (Waldbronn, Germany)	2 mM
Oligomycin	Agilent Technologies Deutschland GmbH (Waldbronn, Germany)	1.5 µM
FCCP	Agilent Technologies Deutschland GmbH (Waldbronn, Germany)	2.5 µM
Rotenone / Antimycin A	Agilent Technologies Deutschland GmbH (Waldbronn, Germany)	1.5 µM
Hydrogen Peroxide in Methanol	Carl Roth GmbH + Co. KG (Karlsruhe, Germany)	3 % (v/v)
Citrate Buffer, 0.01 M, pH 6.0	Carl Roth GmbH + Co. KG (Karlsruhe, Germany)	0.01 M
Vectastain® Elite ABC Kit	Vector Laboratories (Burlingame, USA)	—
DAB Substrate Kit	Vector Laboratories (Burlingame, USA)	—
Haematoxylin	Carl Roth GmbH + Co. KG (Karlsruhe, Germany)	—
Roti® Histokit	Carl Roth GmbH + Co. KG (Karlsruhe, Germany)	—
Roti®-Histol	Carl Roth GmbH + Co. KG (Karlsruhe, Germany)	100 % (v/v)
Ethanol (≥ 99.8 %)	Merck KGaA (Darmstadt, Germany)	100 %, 90 %, 70 % (v/v)
RNase-free distilled	Thermo Fisher Scientific (Dreieich, Germany)	—

Reagent	Company / Distributor (location)	Concentration
water		
SDS	Carl Roth GmbH + Co. KG (Karlsruhe, Germany)	0.5 % in PBS; 10 % stock for hybridisation mix
PBS	Thermo Fisher Scientific (Dreieich, Germany)	—
Pepsin	Sigma-Aldrich Chemie GmbH (Taufkirchen, Germany)	0.2 % (w/v) in 0.2 M HCl
Hydrochloric acid (HCl)	Merck KGaA (Darmstadt, Germany)	0.2 M
Glycine	Carl Roth GmbH + Co. KG (Karlsruhe, Germany)	0.1 M in PBS
DNase I	Roche Diagnostics GmbH (Mannheim, Germany)	50 U mL^{-1}, 1 h @ 37 °C
Formamide	Thermo Fisher Scientific (Dreieich, Germany)	500 µL per 1 mL pre/hybridisation mix
20 × SSC	Sigma-Aldrich Chemie GmbH (Taufkirchen, Germany	Stock; washes 2×, 1×, 0.5× SSC
Sodium-phosphate buffer	Merck KGaA (Darmstadt, Germany)	0.5 M NaH_2PO_4 + 0.5 M Na_2HPO_4 (1 : 1)
EDTA	Thermo Fisher Scientific (Dreieich, Germany)	50 mM
Salmon sperm DNA	Thermo Fisher Scientific (Dreieich, Germany)	3.33 µg $µL^{-1}$
LNA Probes (E6 / E6*I & controls)	Qiagen GmbH (Hilden, Germany)	5 µM stock; 1 µL probe + 250 µL hybridisation mix
ProLong™ Antifade Mountant (no NucBlue)	Thermo Fisher Scientific (Dreieich, Germany)	—
Ibidi Mounting Medium	Ibidi GmbH (Gräfelfing, Germany)	—
VectaShield® Hard-Set	Vector Laboratories (Burlingame, USA)	—

Reagent	Company / Distributor (location)	Concentration
Mounting Medium with DAPI		

Table 7: Extensive List of Instruments and Equipment Used in Molecular, Imaging, and Functional Assays

Reagent / Equipment	Company / Distributor (Location)
M220 Focused-ultrasonicator	Covaris Ltd. (Brighton, United Kingdom)
4150 TapeStation System	Agilent Technologies Deutschland GmbH (Waldbronn, Germany)
CFX96 Equipment	Bio-Rad Laboratories GmbH (Feldkirchen, Germany)
PX1™ Plate Sealer	Bio-Rad Laboratories GmbH (Feldkirchen, Germany)
C1000 Touch Thermal Cycler	Bio-Rad Laboratories GmbH (Feldkirchen, Germany)
QX200™ Droplet Reader	Bio-Rad Laboratories GmbH (Feldkirchen, Germany)
Sonicator (Bioruptor® Plus)	Diagenode S.A. (Seraing, Belgium)
Zeiss AxioObserver Microscope with O_2control	Carl Zeiss Microscopy Deutschland GmbH (Oberkochen, Germany)
Zeiss LSM 980 Airyscan2 Confocal Microscope	Carl Zeiss Microscopy GmbH (Oberkochen, Germany – via CECAD)
CLARIOstar® Plate Reader	BMG LABTECH GmbH (Ortenberg, Germany)
XFe96 Analyzer	Agilent Technologies Deutschland GmbH (Waldbronn, Germany)
Microtome	Profcontrol GmbH (Schönwalde-Glien, Germany)
Fluorescence Microscope for Localization/Staining	Carl Zeiss Microscopy GmbH (Jena, Germany)

Table 8: List of the Antibodies used in Western blot and Immunofluorescence assays

Antibody (target)	Host / Clonality	Company / catalog number	WB dilution	IF dilution
HK1	Rabbit pAb	Sigma-Aldrich, HPA007044	1:500	—
PKM2	Rabbit pAb	Cell Signaling Technology, 3198	1 : 1000	—
H6PD	Rabbit pAb	Sigma-Aldrich, HPA005440	1 : 250	—
ATP5B	Rabbit pAb	Sigma-Aldrich, HPA001528	1 : 250	—
COX1 / MT-CO1	Rabbit pAb	Cell Signaling Technology, 62101	1 : 1000	—
LDH (H-160)	Mouse pAb	Santa Cruz Biotechnology, sc-33781	1 : 1000	—
NRF2	Rabbit pAb	Sigma-Aldrich, SAB4501984	1 : 500	1 : 500
AKR1C1	Rabbit pAb	Abcam, ab192785	1 : 500	1 : 1000
AKR1C3	Rabbit pAb	Novus Biologicals, NBP1-31378	1 : 1000	1 : 1000

Table 9: List of Oligonucleotide Primers

Sequence name	Sequence (5'→3')
HPV16-E6*I-RT, F	aatgtttcagcacccacagg
HPV16-E6*I-RT, R	gttaatacactcacgtcgcag
HPV16-E6FL-RT, F	aatgtttcaggacccacagg
HPV16-E6FL-RT, R	cacacaacggtttgttgtattgctg
HPV16-E7-RT, F	gctcagaggaggaggatgaa
HPV16-E7-RT, R	tggggcacacaattcctagc
m cherry 1, F	ccccgtaatgcagaagaaga
m cherry 1, R	ttggtcaccttcagcttgg
HPRT-1, F	tgacactggcaaaacaatgca
HPRT-1, R	ggtccttttcaccagcaagct
147-tu.8, F	agactgaggcaggagactcg
147-tu.8, R	agatgaacccaccaggaaga
147-tu.9, F	ggtactcctggccagacc
147-tu.9, R	ggcagctgtttccagtgata
90.1, F	ctctgtccggttctgcttg

Sequence name	Sequence (5'→3')
90.1, R	aagaagctcaaccttattggtca
90.11, F	tgccagtacgcctagaggtt
90.11, R	gtggtggctgatgcttgtaa
90.12, F	cctagcaaatataagaaacacagca
90.12, R	gcctttaatgtataaatcgtctgg
90.13, F	agtggcacgcctaggattat
90.13, R	gtggcatgctgctaaaacaa
90.14, F	tgcatatgaaggtatagatgtgga
90.14, R	cgggatctggcagctact
90.15, F	aaaacacaatggggaaagga
90.15, R	cagtagttgcacatagtgcagtg
90.16, F	caggggatgctatatcagatgac
90.16, R	aattgccaaaacttggaagc
90.3, F	cgttgaagacagagcgacag
90.3, R	cagccatggtagattatggtttc
90.4, F	accgaagcgtagagtcacac
90.4, R	gcagaggagctgtggaagtt
90.8, F	taaaggatggccactaatgc
90.8, R	tccttgcaatacagatgtacacac
TLA154.1, Hu, F	acagccccaaacccagggga
TLA154.1, Hu, R	tgtgccagagagttccattaggca
TLA154.1, Int, R	atcacagatggtacaatgggcctacg
TLA154.2, Hu, F	tggtgtttccaaaccttccgtgagc
TLA154.2, Hu, R	ttggggtagtggcatggatgga
TLA154.3, Int, F	gcttccaatcacctccatcatctaccc
TLA154.3, Hu, F	tgggcctcagtctcttctccct
TLA154.2, Hu, R	ggatcctggagacattgcaagtcagg
TLA1.2, Int, R	cagttttaggttcacagtaaaacatct
TLA1.3, Int, F.N	cagattctaggtggccttatttaca
TLA1.3, Int, R	tcacataaggtttcattataacaagtc
TLA2.1 New Int, F	cgtctacatggcattggacagga
TLA2.1 New Int, R	gcaactcaagtgcccgtgga
TLA2.2 New Int, F	tgaaagtgtaaaatgccctccag
TLA2.2 New Int, R	gactgccctataactcccaaca

Sequence name	Sequence (5'→3')
TLA2.3 New Int, F	tctgggggaatggaaggtaca
TLA2.3 New Int, R	tgcaccctgttggtatttcac
TLA2.4 New Int, F	aacgatggagactctttgcca
TLA2.4 New Int, R	agtggcaacctccttagcctat
TLA3.1, Int, R	gcccaccagcccatacct
TLA3.2, Int, R	ggaagctgggacttcgttctt
TLA4.1, Hu, F	accactgcactcccgcctga
TLA4.1, Hu, R	tgatccgcccaccttggcct
TLA4.1, Int, F	ggaaatccagtgtatgagcttaatg
TLA4.1, Int, R	tcccaaagtgctgggattac
TLA4.2, Hu, F	gctggagtgcggtggtgcaa
TLA4.2, Hu, R	gcggcagctcacgcctgtaa
TLA4.2, Int, F	catattacagacccttgcagaaa
TLA4.2, Int, R	cggatcatgaggttaggaga
TLA4.3, Hu, F	gtgccacagcgcccagctaa
TLA4.3, Hu, R	cccagcactttgggaggccg
TLA4.3, Int, F	cattccccatgaacatgcta
TLA4.3, Int, R	gtggtgagccgagatcgt
TLA4.4, Hu, F	tagttggccatagtggtgcat
TLA4.4, Hu, R	catagctcactgaagccttgaa
TLA4.4, Int, F	tggacattacaagacgttagcc
TLA4.4, Int, R	catagctcactgaagccttgaa
TLA4.5, Hu, F	cagcaacctggatagaattagaga
TLA4.5, Hu, R	cctcataacttggctcccatt
TLA4.5, Int, F	cctttaaatttacttcccaaaaagtg
TLA4.5, Int, F.N	ggggatcttctttaggtgctggaggt
TLA4.5, Int, R	gcatcctcataacttggctcccatt
TLA4.6, Hu, F	tttctgtttttaattctgtttatgtgg
TLA4.6, Hu, R	caccatgttcaagtgggtttc
TLA4.6, Int, F	caaccattagcagatgccaaaa
TLA4.6, Int, R	tccacatgtcagtacaagtgatg
TLA4.7, Hu, F	gcccaaacttctgcaccttcggt
TLA4.7, Hu, R	ggaggcggaggttgcaggga
TLA4.7, Int, R	tcctgtgacctttctccaaca

Sequence name	Sequence (5'→3')
TLA5.1, Int, F	acactggctgtatcaaagaataaa
TLA5.1, Int, R	ccgtctgttcttggctctact
TLA5.2, Int, F	cttcgttgctgctaaacacag
TLA5.2, Int, R	gacagaagcgtttcattttcag
TLA5.3, Int, F	gaaaaacaaagtagagctgcaaa
TLA5.3, Int, R	acaggccaatttctgcattt
TLA5.3, Int, new, F	aaaaacaaagtagagctgcaaaaag
TLA5.3, Int, new, R	aacaggccaatttctgcatt
TLA5.4, Int, F	ggatttccgttttcgtcaa
TLA5.4, Int, R	ttgatggcttatatgcaaaagg
TLADIPS.1 Int F	gcaattgaactgcaactaacg
TLADIPS.1 Int R	cggcttcagtggaaattgat
TLADIPS.2 Int F	atggaggtgattggaagcaa
TLADIPS.2 Int R	tggatgggatctttctcacc
TLADIPS.3 Int F	actgtggtagagggtcaagt
TLADIPS.3 Int R	gctcagagcatcagtccatct

Table 10: List of ddPCR Probes

Bio-Rad Probe Assay Name	Bio-Rad Probe Assay ID	Probe Fluorophore
AKR1C1	dHsaCPE5059278	FAM
AKR1C2	dHsaCPE5192449	FAM
AKR1C3	dHsaCPE5031242	FAM
NFE2L2	dHsaCPE5031452	FAM
HK1	dHsaCPE5045666	FAM
PKLR	dHsaCPE5037746	FAM
PKM	dHsaCPE5059028	FAM
LDHA	dHsaCPE5044580	FAM
HPRT	dHsaCPE5192872	HEX

Table 11: List of Plasmids

Plasmid	Origin / Source
pEGFP-C1	Clontech #2487
pEGFP-C1-HPV16-E6-GFP	Available from AG Akgül
pEGFP-N1-HPV16-E6*I-HIS-GFP	Available in house (Ziogas et al. 2024)

6 Results

Sections 6.1 to 6.5 were adapted from (Demers, Balaji et al., 2024)

6.1 Cell-based TLA Pinpoints HPV16 Insertion Points in HNSCC Models

To comprehensively map HPV16 integration sites and associated genomic alterations, TLA, followed by NGS, was applied to seven HPV^+ HNSCC cell lines (Figure 8). The median read coverage across the viral genome ranged from 61 to 9,292, with 98% of nucleotides covered at a depth of at least 30× (Table S4 and Figure S1). In the UM-SCC-47 cell line, a deletion of approximately 500 bp (HPV16: 3212–3718), spanning the E2/E4 region, was detected. TLA recovered genomic fragments extending hundreds of kb around each integration site. All previously reported loci identified by DIPS-PCR in the study by (Olthof et al. 2014) were confirmed, and several additional integration sites were identified. Moreover, the majority of HPV16 insertion loci detected by prior WGS were also confirmed (Table 11, Figure S2) (Akagi et al. 2014). In four of the seven cell lines previously examined by (Akagi et al. 2014), TLA reproduced the same integration sites (Table 11), with only minor discrepancies in precise breakpoint coordinates. A complete list of individual breakpoints is provided in Table S5.

Table 11: Identified HPV16 integration sites and their corresponding genes in HPV$^+$ HNSCC cell lines, as determined by cell-based TLA, WGS and DIPS PCR (Demers, Balaji et al., 2024).

	DIPS PCR (Olthof, 2015)		TLA			WGS (Akagi, 2014)		
Cell line	Locus	gene	Locus	HPV-human breakpoint(s)	Gene(s)	Locus	HPV-human breakpoint(s)	Gene(s)
UD-SCC-2	Xq21.33	DIAPH2	Xq21.33	6 breakpoints (96,215,117-chrX:96,380,876)	DIAPH2	Xq21.33	6 breakpoints (96,214,932-96,380,894)	DIAPH2
UM-SCC-47	3q28	TP63	3q28	2 breakpoints (189,596,814-189,612,849)	TP63	3q28	5 breakpoints (189,596,808-189,620,988)	TP63
UPCI:SCC090	9q22.33	TRMO	9q22.33	12 breakpoints (100,575,617-100,714,372)	PTCS2, TRMO, HEMGN	9q22.33	19 breakpoints (100,575,616-100,706,106)	TRMO, HEMGN
			6p21.2	5 breakpoints (36,878,572-37,164,550)	C6orf89	6p21.2	8 breakpoints (36,878,571-37,164,468)	C6orf89
			3p12.2	2 breakpoints (82,041,282-82,275,717)	LINC0008	3p12.2	4 breakpoints (81,834,933 -82,275,924)	Intergenic
						2q23.3	1 breakpoint (151,992,389-151,992,569)	Intergenic

	DIPS PCR (Olthof, 2015)		TLA			WGS (Akagi, 2014)		
UPCI:SCC152	9q22.33	TRMO	9q22.3	10 breakpoints (100,575,617-100,714,372)	PTCS2, TRMO, HEMGN	n.d.	n.d.	n.d.
			3p12.2	4 breakpoints (81,834,934-82,275,717)	LINC0008			
UM-SCC-104	No integration	-	17p11.2	2 breakpoints (19,609,637-19,609,646)	SLC47A2	17p11.2	2 breakpoints (19,609,450-19,609,917)	SLC47A2
UPCI:SCC154	21q11.2	NRIP1	21q21.1	2 breakpoints (16,645,539-16,688,012)	intergenic	n.d.	n.d.	n.d.
93-VU-147T	17q12	Intergenic	17q12	1 breakpoint (36,423,208)	Intergenic	n.d.	n.d.	n.d.
			15q13.3	2 breakpoints (31,627,224-31,627,391)	KLF13			
			3p21.2	4 breakpoints (51,537,011-51,577,389)	RAD54L2			
			2q11.2	1 breakpoint (101,595,323)	NPAS2			

	DIPS PCR (Olthof, 2015)		TLA			WGS (Akagi, 2014)		
			Xp21.1	2 breakpoints (33,479,828-33,479,83)	Intergenic			

6.2 FFPE-TLC Maps HPV16 Integration Events in OPSCC Specimens

After establishing integration of HPV in HPV$^+$ HNSCC cell lines, the modified version of TLA suitable for FFPE termed FFPE-TLC was applied to 27 preselected FFPE HPV$^+$ OPSCC specimens. Viral presence was confirmed in every sample. Median read coverage across the HPV genome ranged from 101× to 29095×, with approximately 99 % of bases covered at a depth greater than 30× (Table S6 and Figure S3). While complete E2 deletions, frequently observed in cervical cancer, were specifically investigated, none were detected in this cohort.

HPV16 integration was identified in 15 of 27 tumours (56 %), yielding 54 unique human loci and a total of 139 virus–host junctions (Table 12, Table S7). Breakpoints were evenly distributed across the viral genome, with no positional bias (Chi-square test, $p = 0.274$) (Figure 10 (A), (B)). The distribution of HPV integrations revealed a uniform dispersal across the human genome, with no evidence of hotspots indicative of repeated integrations. It was observed at each integration locus that virus-host junctions clustered into 1 to 10 breakpoints (Figure10 (C) ,(D)). The number of virus-host breakpoints varied significantly between tumours, with individual samples showing between two and 63 breakpoints. The median number of breakpoints was 4 (Figure 10 (D)). The TLA enabled the sequencing of several hundred kbs surrounding each integration site, providing a comprehensive structural context. In 73 of the 139 breakpoints (53%), short areas of microhomology (1–5 bp) were identified between viral and human sequences. In 36 out of 54 integration events (67%), the viral genome integrated itself into a gene. The majority of these genes are implicated in DNA repair pathways, EMT and metastasis, or anti-apoptotic/oncogenic signalling, suggesting a potential impact on tumour biology. In the remaining 12 out of 27 samples (44%), no HPV integration was detected (Table 12). This may indicate that the HPV genome remained in an episomal state within these cases, consistent with a subset of transcriptionally active, non-integrated viral genomes frequently reported for HPV$^+$ OPSCC. 23 of the 27 patients in the study had previously undergone HPV integration testing using DIPS-PCR on matching fresh-frozen tumour samples (Olthof

et al. 2014). The analysis revealed that 13 of the 23 tumours exhibited a perfect match with the profiles generated by our FFPE-TLC assay, when a comparison was made between the two sets of results. In 6 additional cases, FFPE-TLA confirmed all DIPS-identified integration sites and uncovered additional sites. In 4 cases, discrepancies were observed: one sample (case 15) exhibited an integration event that was not detected by DIPS-PCR, and three samples (cases 21, 22, and 23) divergent integration patterns between the two methods (Table 12).

Table 12: Comparative analysis of HPV integration sites and associated genes in HPV⁺ oropharyngeal tumours from FFPE samples identified using FFPE-TLC and DIPS-PCR methods (Demers, Balaji et al., 2024).

	DIPS-PCR			FFPE-TLC		
Patient#	**Int.**	**Locus**	**Gene**	**Int.**	**Locus**	**Gene**
1	No	no integration	-	No	no integration	-
2	No	no integration	-	No	no integration	-
3	No	no integration	-	No	no integration	-
4	No	no integration	-	No	no integration	-
5	No	no integration	-	No	no integration	-
6	No	no integration	-	No	no integration	-
7	No	no integration	-	No	no integration	-
8	No	no integration	-	No	no integration	-
9	No	no integration	-	No	no integration	-
10	No	no integration	-	No	no integration	-
11	No	no integration	-	Yes	6q12	LINC02549
					9p24.2	VLDLR
12	No	no integration	-	Yes	2q12.1	TMEM182
					2q24.1	NR4A2
13	No	no integration	-	Yes	3q13.2	CD200
14	No	no integration	-	Yes	2p16.1	BCL11A
					5q14.2	XRCC4
15	Yes	13q21	Intergenic	No	no integration	-

	DIPS-PCR			FFPE-TLC		
16	Yes	3q28	LEPREL1/TP63	Yes	3q28	Intergenic
17	Yes	2p23.2	BABAM2	Yes	2p23.2	BABAM2
18	Yes	17q21.2	Intergenic	Yes	17q21.2	Intergenic
19	Yes	22q12.3	SYN3	Yes	2q32.1	Intergenic
					22q12.3	DEPDC5
20	Yes	6p22.3/7p15	Intergenic/GARS	Yes	1p31.1	Intergenic
					6p22.3	Intergenic
					17p13.3	HIC1 & SMG6
					Yq11.23	Intergenic
21	Yes	1q32.1	GOLT1A	Yes	1q31.1	ODR4
		3p14.3	ERC2		1p35.3	Intergenic
		Yq11.23	Intergenic		2q21.1	FAM168
					4q23	TSPAN5
					8q12.3	LINC01414
					16p13.11	NDE1, MYH11
22	Yes	18q12.2	INO80C	Yes	3q23	PAQR9-AS1
					8q11.21	UBE2V2
23	Yes	6q21	HDAC2	Yes	2p12	LRRTM4
					14q32.32	TRAF3
					Yq11.221	Intergenic
24	-	n.d.		No	no integration	-

	DIPS-PCR			FFPE-TLC		
25		n.d.		Yes	1q24.3	RABGAP1L
					13q21.2	Intergenic
					17q21.33	LINC002073
26	-	n.d.		Yes	1p22.3	PRKACB
					14q11.2	Intergenic
					20q11.21	CCML2L, HCK
27	-	n.d.		Yes	2p16.1	Intergenic
					2p23.3	Intergenic
					2p24	CENPA
					2p11.2	KCMF1
					2q35	TNS1
					3p24.1	TGFBR2
					3p21.2	DOCK3
					4p13	ATP8A1
					4q28.3	Intergenic
					5p14	Intergenic
					5p15.2	Intergenic
					7q11.22	Intergenic
					8q23.3	TRPS1
					9q22.1	Intergenic
					9q34.12	NUP214

	DIPS-PCR			FFPE-TLC		
					12q24.33	Intergenic
					13q34	CDC16, CHAMP1
					14q24.1	RAD51B
					15q25.3	AKAP13
					18p11.31	Intergenic
					22q13.31	LINC01644

n.d. = not determined

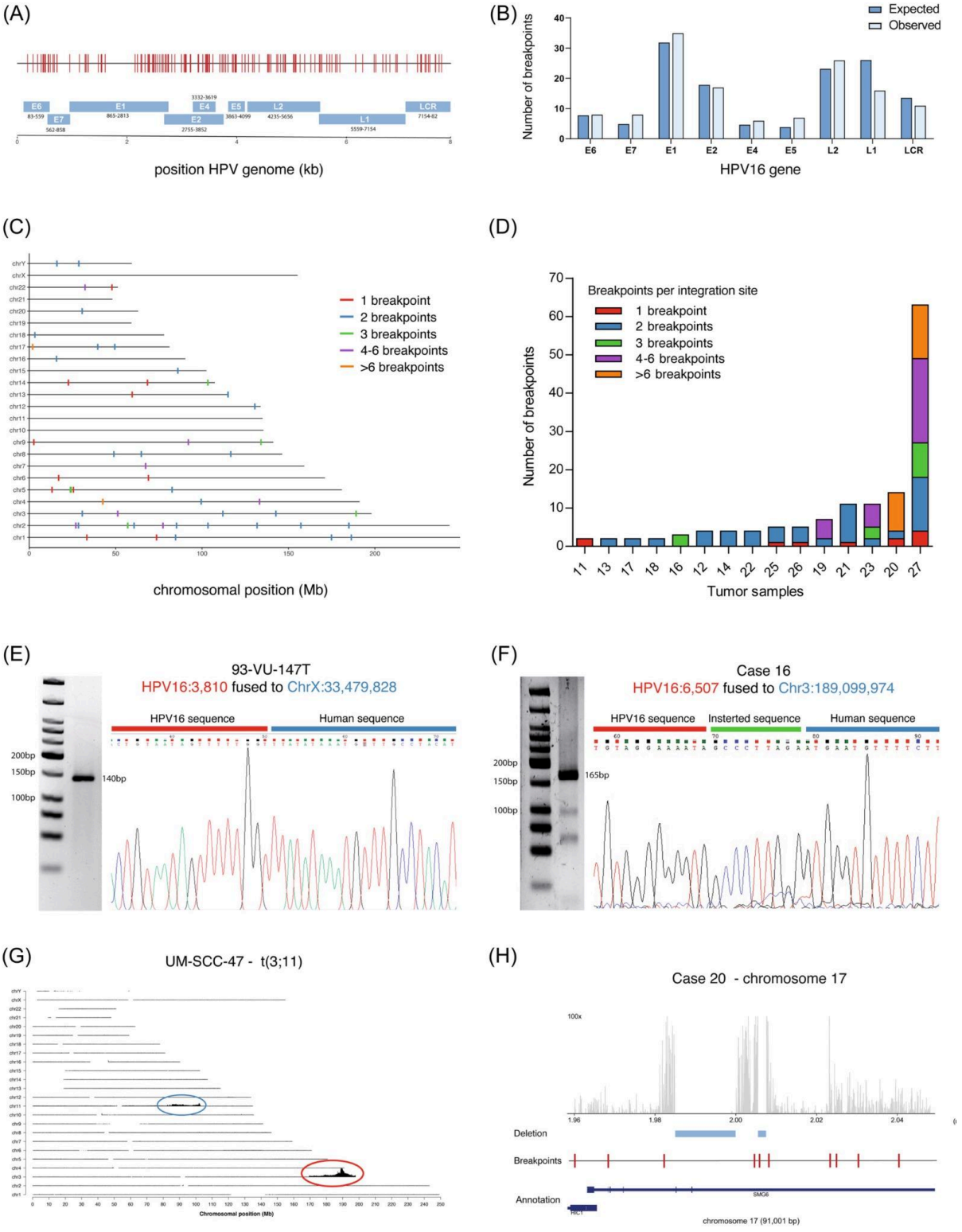

Figure 10. HPV integration breakpoints in OPSCC. (A) A total of 139 breakpoints identified in 27 FFPE HPV16$^+$ OPSCC specimens were mapped along the HPV16 genome. (B) Observed breakpoint frequencies for each viral gene were compared with values expected from a random, length-normalized distribution; no significant difference was detected (Chi-square test, *p*: 0.274). (C) Overview of 54 HPV integration loci and their 139 corresponding breakpoints across the human

genome. (D) Quantity and distribution of breakpoints and breakpoints per cluster across 15 tumours with HPV integration. (E–F) Validation of cell-based TLA results by PCR followed by Sanger sequencing in (E) the 93-VU-147T cell line and (F) patient sample 16. (G) Whole human genome coverage plot for cell line UM-SCC-47 showing elevated read depth on chromosomes 3 and 11, consistent with an inter-chromosomal translocation. (H) Approximately 100 kb surrounding the integration site on chromosome 17 in case 20 exhibits multiple breakpoints and structural variants; NGS read depth is shown on the y-axis, and complete deletions are highlighted in blue (Demers, Balaji et al., 2024).

6.3 Verification of Integration Loci Determined by TLA/TLC

Given the absence of a standardized method for detecting HPV integration events in FFPE samples - and the frequent discrepancies observed between DIPS-PCR and FFPE-TLA/TLC - an independent validation of selected integration loci was performed. A total of 17 breakpoints identified by TLC in five tumours, spanning eight integration sites, were examined using PCR followed by Sanger sequencing. In addition, 12 breakpoints identified by TLA in three cell lines were similarly validated. This approach allowed for the robust assessment of the integration sites for both sample types. Notably, in cases 15, 22, and 23, three integration sites previously reported exclusively by DIPS-PCR could not be confirmed by PCR in the FFPE samples. These events are therefore considered potentially artifactual or absent in the current dataset (Tables S8). To increase confidence in the mapping results, all TLA/TLC reactions employed two independent primer sets targeting regions within HPV16-E1 and E7, ensuring assay robustness across different genomic contexts. In addition, seven FFPE samples were re-analyzed using random endonuclease digestion in place of NlaIII, which had been used in the initial restriction-based protocol. The integration profiles derived from these alternative digestions were fully consistent with the original TLA/TLC results, providing additional support for their accuracy.

6.4 Structural Variation at HPV Integration Sites

Previous studies on fresh-frozen samples have shown that HPV frequently integrates into genomic regions previously impacted by structural variations (SVs), including deletions, insertions, inversions, duplications, and inter-chromosomal translocations (Symer et al. 2022). Accurate detection of virus–host fusions is often complicated

when the adjacent host sequences are short, repetitive, or complicated, making SV identification particularly challenging in FFPE-derived material (Allahyar et al. 2021). Among the examined cell lines, all but one showed HPV insertions in close proximity to other structural variations, such as copy-number alterations, duplications, translocations, or more complex rearrangements. For example, UM-SCC-47 harbored an HPV16 insertion at chromosome 3q28 (Figure. 10 (G), red), accompanied by an approximately 20 Mb amplification on chromosome 11 (Figure. 10 (G), blue). Notably, no virus–host junctions were detected on chromosome 11, suggesting that the amplified segment may have been translocated near the 3q28 integration site, corroborating prior observations (Olthof et al. 2014; Arenz et al. 2019). In 93-VU-147T, TLA identified a 22 kb read-enriched region on chromosome 17, consistent with previously published DIPS-PCR data. However, there was an absence of coverage in the adjacent chromosome 17 sequence, indicating that this segment has likely been translocated, potentially to chromosomes 9, 10, or 11, where increased coverage was observed without corresponding breakpoints. In the tumour samples, 54 HPV insertion sites were identified, with 47 (87%) next to structural variations: deletions (44%), insertions (2%), inversions (6%), duplications (19%), and translocations (6%). Additionally, 30% of integration sites exhibited complex genomic rearrangements involving multiple breakpoints. A representative example is shown for chromosome 17 in case 21 (Figure. 10 (H)).

6.5 Overlapping HPV Integration Sites and HPV16–HPV16 Fusion Sites Link Primary OPSCC with Distant Metastases

HPV^+ HNSCC characteristically exhibit a reduced frequency of point mutations and copy-number alterations when compared with HPV^- HNSCC (Klussmann et al. 2009). Nevertheless, in cases where HPV^+ OPSCC recur or metastasise to distant sites, they often present with mutation profiles that diverge from the primary tumour (Reder et al. 2021). This complicates the application of conventional tracking methods, which are typically limited to the analysis of somatic variations. To overcome this limitation, we investigated whether shared virus–host integration junctions could serve as stable clonal markers. A cohort of four patients who had been diagnosed with primary tonsillar cancer and subsequently developed metastases in distant organs (lung, liver,

bone) was analyzed. In three of the four metastatic cases, HPV DNA was found to be integrated into the host genome. In each of these integration-positive cases, TLC revealed at least one HPV integration breakpoint that was identical in both the primary tumour and the matched metastatic site (Figure 11 (A), (B); Table S9). Furthermore, cases 25 and 27 exhibited 2 and 3 identical HPV16-HPV16 fusion junctions, respectively (see Table S10), further supporting a common clonal origin. The data demonstrate that the presence of analogous HPV integration events provides compelling evidence for a single clonal origin, even in cases where other genomic traits do not provide unequivocal evidence.

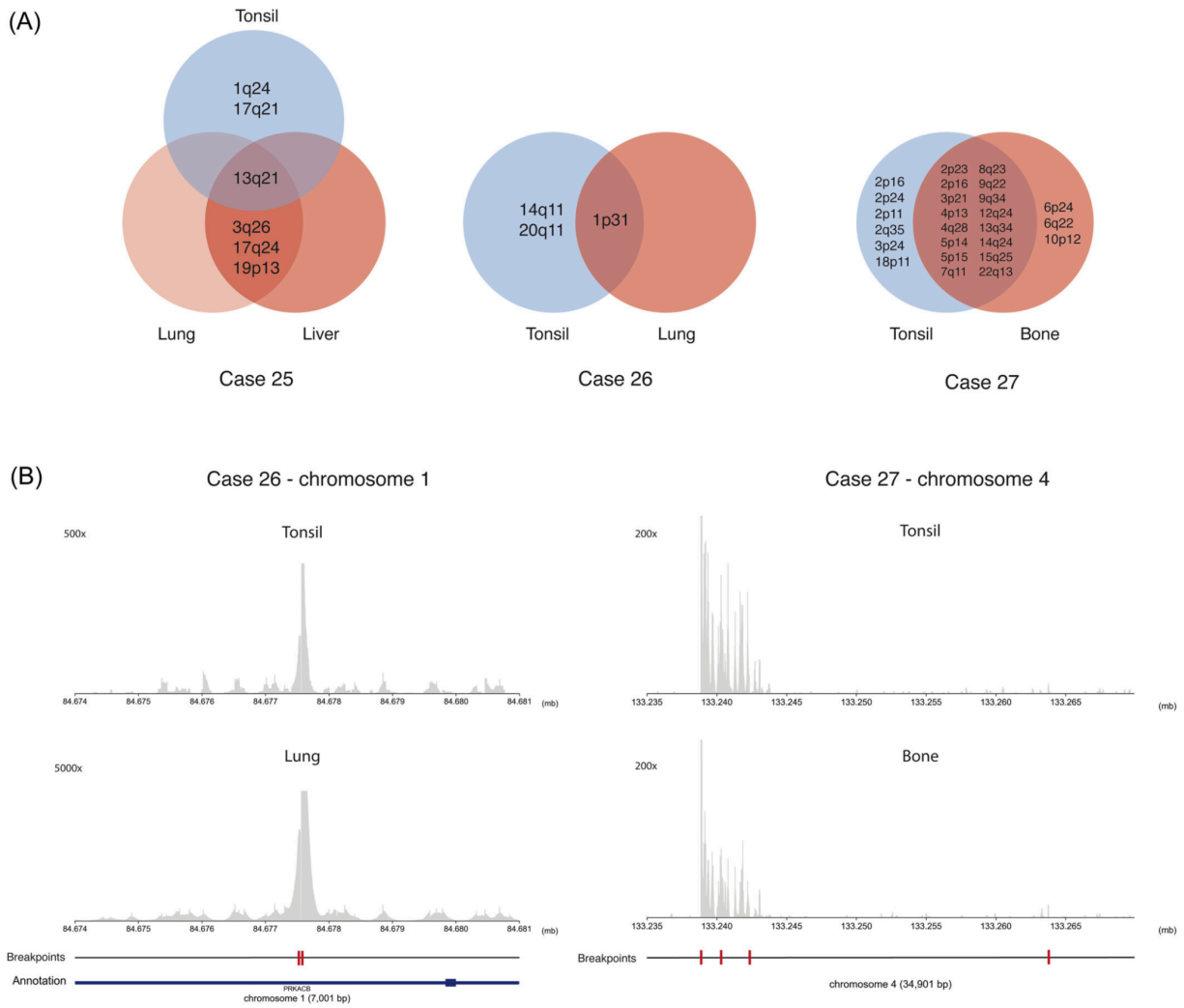

Figure 11: FFPE-TLC examination of the clonality of initial OPSCC lesions and matching metastases. (A) A Venn diagram showing the HPV16 integration loci found in the primary tumours of the tonsils and their lung, liver and bone metastases. (B) Examples of NGS read-depth plots showing the same HPV16 insertion spots and shared virus-host breakpoints on chromosomes 1 and 4 in

patients 26 and 27, respectively. This supports the idea that they all came from the same clone (Demers, Balaji et al., 2024)

6.6 Generation and Validation of HEK 293 Cell Lines Stably overexpressing HPV16-E6 and HPV16-E6*I

HPV16-E6*I has been shown to disrupt redox homeostasis and cellular metabolism in cervical cancer cells, thereby contributing significantly to chemoresistance (Wanichwatanadecha et al. 2012). To investigate the specific alterations in ROS metabolism and metabolic reprogramming induced by HPV16-E6*I, stable clones of HEK 293 were established, overexpressing GFP (control), HPV16-GFP-E6, or GFP-HPV16-E6*I-His. RT-qPCR analysis confirmed robust transgene expression, with transcript levels increased approximately 80-fold and 60-fold for HPV16-E6 and HPV16-E6*I, respectively (Figure 1B). Importantly, no off-target splice variants were detected in these cell models. HEK 293 cells, which endogenously express wild-type p53 (Sun et al. 2010), represent a suitable system for evaluating the impact of HPV16-E6 driven p53 degradation. To confirm that the full-length HPV16-E6 construct, unlike HPV16-E6*I, induces p53 degradation, immunofluorescence staining and confocal microscopy was performed to examine p53 localization and abundance (Figure 12 (A)). As expected, nuclear p53 staining was retained in both the control and HPV16-E6*I-overexpressing cells. In contrast, the p53 signal was markedly reduced in cells overexpressing full-length HPV16-E6. This result is consistent with the established role of HPV16-E6 in mediating proteasomal degradation of p53 in vivo.

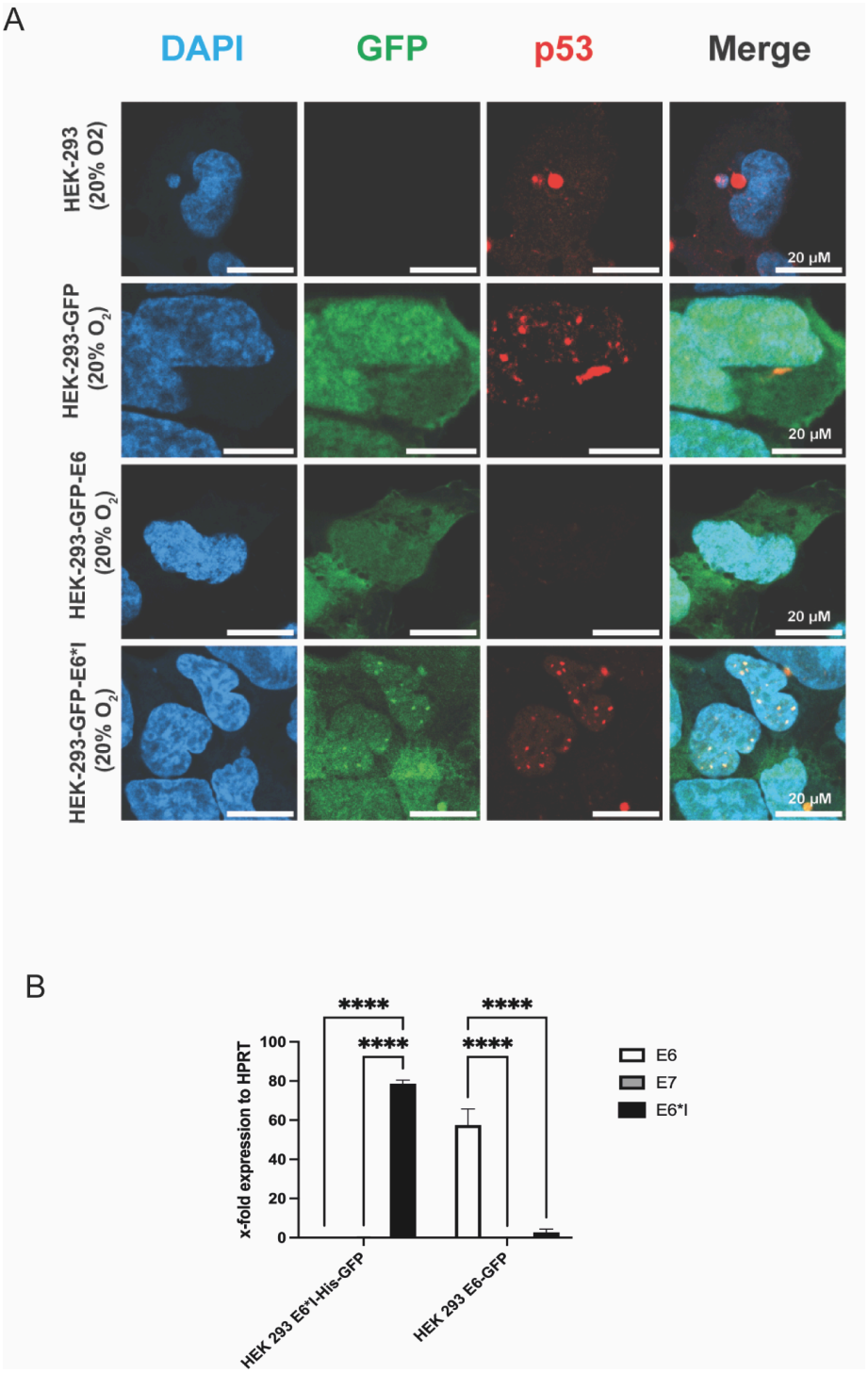

Figure 12. Characterization of stable HEK 293 clones overexpressing HPV16-E6 and HPV16-E6*I. (A) Immunofluorescence images of p53-stained cells. Nuclei were counterstained with DAPI. Images were acquired using confocal microscopy. Scale bar: 20 µm. (B) RT-qPCR analysis of HPV16-E6 and HPV16-E6*I transcript levels. Expression levels were normalized to HPRT. Data represent the mean ± (standard deviation) SD of three biological replicates. A two-way ANOVA followed by a Tukey's post hoc test was performed to assess statistical significance. * $p \leq 0.05$, ** $p \leq 0.01$, *** $p \leq 0.001$, **** $p \leq 0.0001$.

After validating the engineered HEK 293 system, we compared viral oncogene expression to that of HPV16-positive tumour-derived cell lines to evaluate physiological relevance.

6.7 Comparative Analysis of HPV16-E6, -E6*I, and -E7 Transcript Levels in CSCC and HNSCC cell lines

To compare HPV16-E6 and -E6*I gene expression levels in the engineered HEK 293 cell models with those in established HPV16-positive cancer cell lines, mRNA expression in a panel of well-characterised CSCC and HNSCC cell lines was analyzed. This panel included the CSCC cell lines SiHa and CaSki, and the HNSCC lines UM-SCC-104, UM-SCC-47, UM-SCC-90, 93-VU-147T, and UDSCC2.

Notably, the CSCC line CaSki exhibited markedly elevated HPV16-E6*I transcript levels (~40-fold relative to HPRT). Among the HNSCC lines, UDSCC2, UM-SCC-104, and UM-SCC-90 also showed substantial HPV16-E6*I expression (~10-fold over HPRT-1), whereas all other lines expressed HPV16-E6*I at approximately baseline levels (~1-fold relative to HPRT-1).

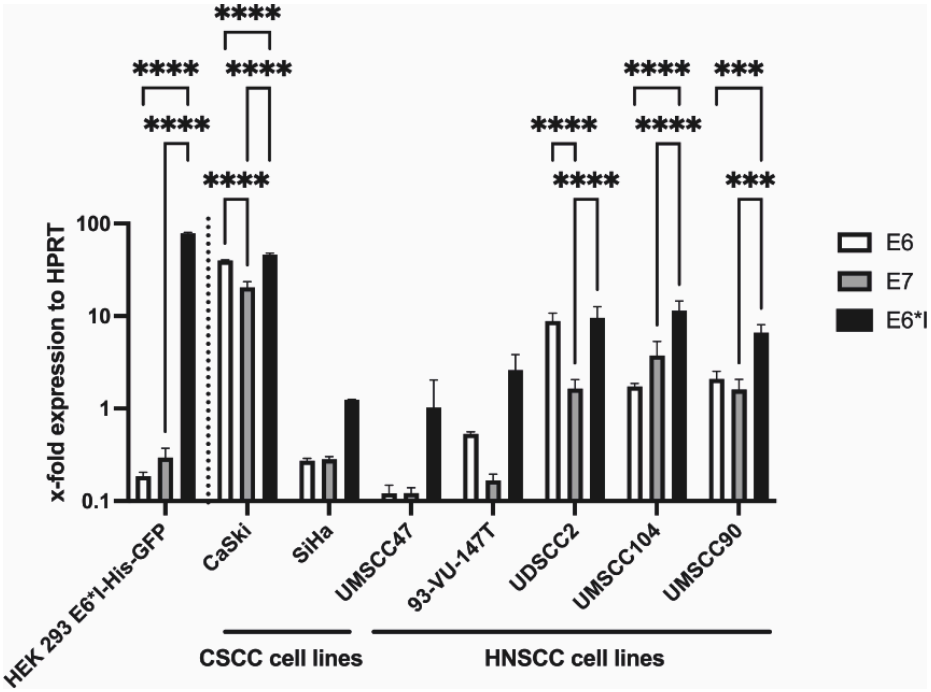

Figure 13. RT-qPCR profiling of HPV16$^+$ CSCC and HNSCC cell lines. mRNA transcript levels of HPV16-E6, -E6*I, and -E7 were quantified in CSCC and HNSCC cell lines and normalized to HPRT-1. For comparison, HPV16-E6*I mRNA expression level in the HEK 293 cell model was also assessed. Data represent one of three biological replicates. A two-way ANOVA followed by a Tukey's post hoc test was performed to assess statistical significance. * $p \leq 0.05$, ** $p \leq 0.01$, *** $p \leq 0.001$, **** $p \leq 0.0001$.

Given that varying O_2 concentrations - such as those found in physiological versus tumoural environments - are known to modulate intracellular ROS levels, we next investigated whether these differences contribute to the transcriptional regulation of HPV16 oncogenes. To address this, HPV16-E6 and -E6*I expression was analysed under controlled O_2 conditions mimicking native and tumour tissue oxygenation (McKeown 2014).

6.8 Variable mRNA expression of HPV16-E6, -E6*I, and -E7 under different O_2 levels in CSCC and HNSCC cell lines

The effect of O_2 concentration on HPV16 oncogene expression was evaluated by culturing the CSCC cell lines SiHa and CaSki, as well as the HNSCC cell lines UM-SCC-090 and 93-VU-147T, under previously described O_2 conditions for a duration of seven days. RT-qPCR analysis revealed substantial O_2-dependent variations in the mRNA expression levels of HPV16-E6, -E6*I, and -E7 in CaSki, UM-SCC-090, and 93-VU-147T cells. In contrast, SiHa cells demonstrated minimal fluctuations in transcript levels across varying O_2 conditions (Figure 14).

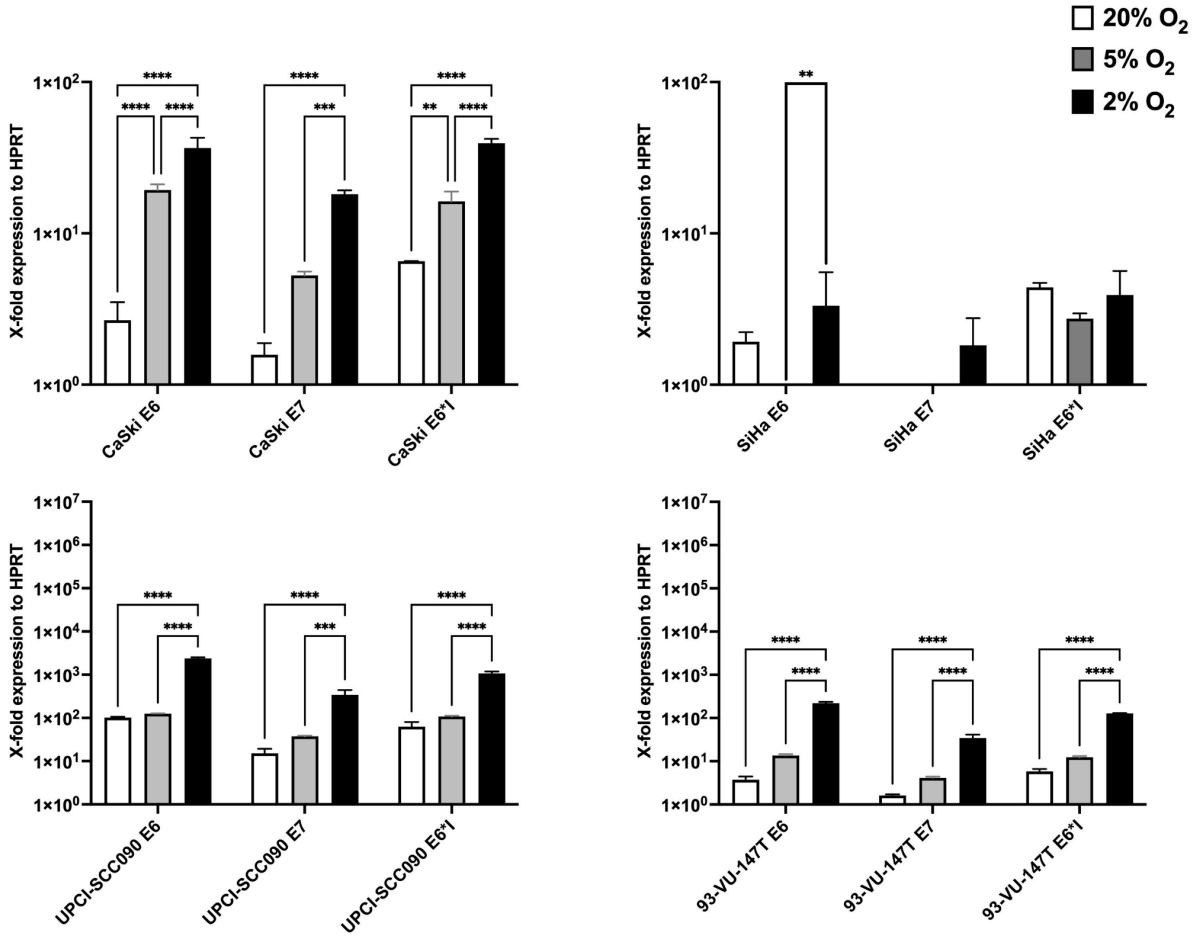

Figure 14. mRNA expression of HPV16 oncogenes E6*I, E6, and E7 under varying O_2 concentrations. (A) CaSki and SiHa CSCC cell lines; (B) UPCI-SCC-090 and 93-VU-147T HNSCC cell lines. The cells were cultured for seven days under the indicated O_2 conditions. mRNA expression levels were assessed by RT-qPCR and normalised to HPRT-1. Bars represent mean ± SD of three technical replicates; data are representative of three independent biological experiments. Statistical

analysis: two-way ANOVA with post-hoc testing. Significance: * $p \leq 0.05$, ** $p \leq 0.01$, *** $p \leq 0.001$, **** $p \leq 0.0001$.

6.9 O_2-modulated regulation of cell proliferation and migration by HPV16-E6 and -E6*I in HEK 293 cells

Since we observed different doubling rates between the different cell lines, wound healing assays were performed to investigate how HPV16-E6 and -E6*I affect cell proliferation and migration under different O_2 concentrations. All cultures were preconditioned for seven days under the defined O_2 concentrations, as described previously. As shown in Figure 15(A), wound-closure dynamics were significantly influenced by both O_2 concentration and viral construct. Quantitative time-course analysis (Figure 15(B)) revealed that HPV16-E6*I-overexpressing cells exhibited significantly accelerated wound closure compared to the HPV16-E6-overexpressing and control cells both under hyperoxia and hypoxia. In contrast, under physiological normoxia, HPV16-E6*I expression was associated with reduced proliferation rates, similar to those of the other cell constructs. To compare migration kinetics, cell front velocity at 14 hours post-scratch was calculated (Figure 15(C)). Under hyperoxic conditions, HPV16-E6*I-overexpressing cells migrated at a velocity of 51.07 pixels/h; significantly faster than HPV16-E6-overexpressing cells (37.52 pixels/h, $p \leq 0.001$) and control cells (HEK 293-GFP 47.67 pixels/h, $p \leq 0.01$; HEK 293 47.07 pixels/h, $p \leq 0.001$). A similar trend was observed in hypoxia (56.31 pixels/h for HPV16-E6*I compared to HPV16-E6-overexpressing cells (25.61 pixels/h, $p \leq 0.001$; HEK 293-GFP 38.38 pixels/h, $p \leq 0.001$; HEK 293 40.01 pixels/h, $p \leq 0.001$). In normoxia, however, the HPV16-E6*I overexpressing cells culture model displayed significantly reduced velocity, matching the slower migration observed in both control and HPV16 -E6-overexpressing cells, and proliferated no faster than their counterparts. In hypoxic conditions, the trend continued: HPV16 -E6*I-overexpressing cells advanced at a velocity of 56.31 pixels/h, but in physiological normoxia, their proliferation was significantly slower, resembling the velocities of both HPV16-E6-overexpressing cells and vector controls. Taken together, these results indicate that HPV16-E6*I confers an O_2-sensitive migratory and proliferative phenotype in HEK 293 cells.

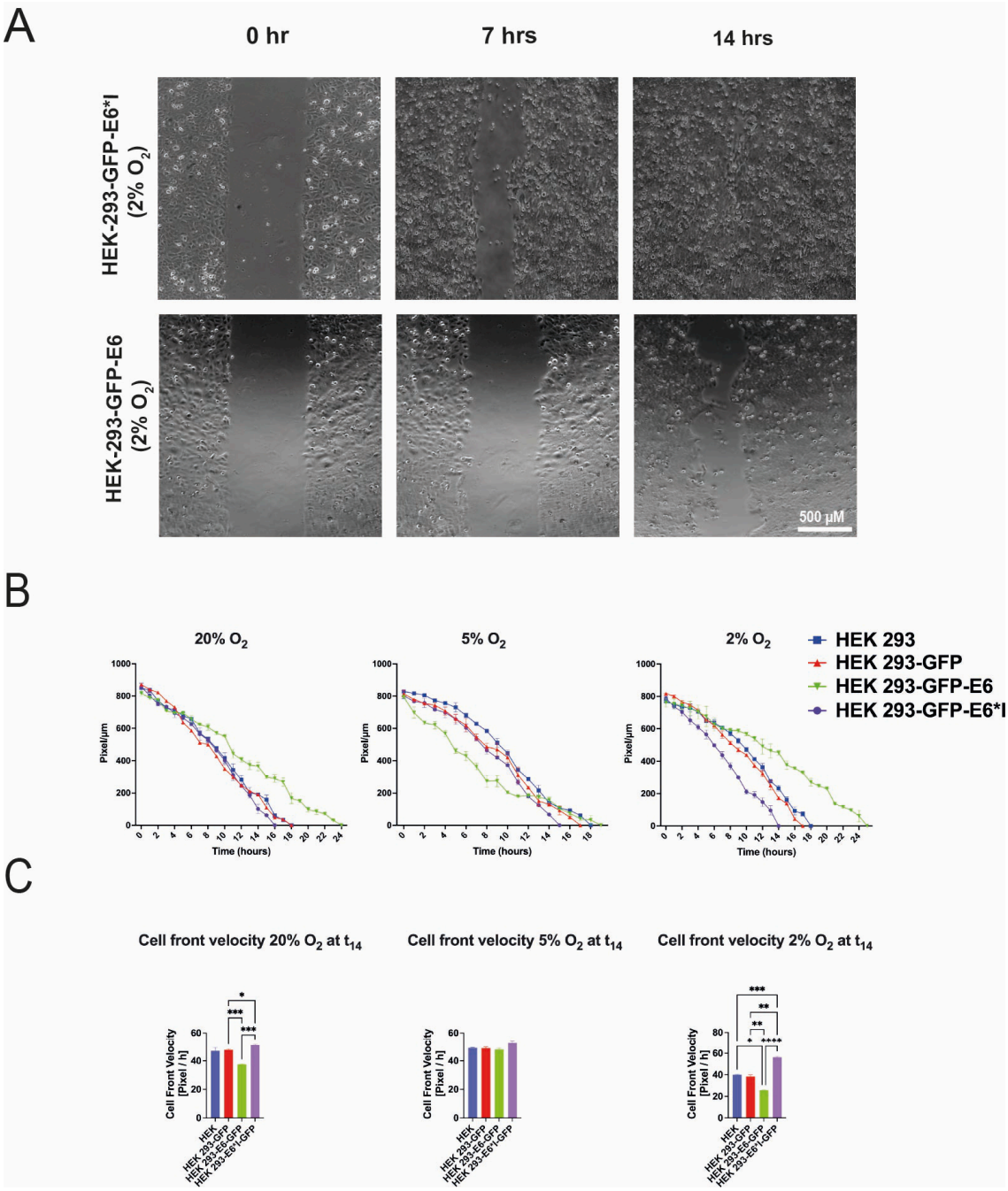

Figure 15. Wound healing assay of cell culture models under defined O_2 concentrations. HEK 293 cells stably overexpressing HPV16-E6*I, HPV16-E6, or an empty vector control were cultured under defined oxygen conditions for seven days prior to the assay. Cells were seeded into two-chamber culture inserts placed in 24-well plates. At t_0, the inserts were removed to create a uniform wound gap. Wound closure was monitored hourly using an automated live-cell imaging system while maintaining O_2-specific conditions. (A) Representative images are shown for 2% O_2. Images illustrate the wound healing progression in HPV16-E6*I-overexpressing cells compared to HPV16-E6-overexpressing cells at 0 hrs (initial gap formation), 7 hrs (intermediate closure), and 14 hrs (near-complete closure in HPV16-E6*I cells under hypoxia). scale bar = 500 µm. (B) Wound closure kinetics were quantified across 20%, 5%, and 2% O_2 using hourly measurements to calculate time to confluence. (C) Cell front velocity was computed as the distance migrated between t_0 and t_{14} post-scratch. Experiments were performed in three biological replicates an representative data are

shown. Data are presented as mean ± SD from three technical replicates. Statistical analysis: two-way ANOVA with post hoc testing. Significance: *p ≤ 0.05, **p ≤ 0.01, ***p ≤ 0.001, ***p ≤ 0.0001.

6.10 Inhibition of AKR1C1 and AKR1C3 reverses HPV16-E6*I-induced migration and gene expression in HEK 293 cells

In order to establish whether the HPV16-E6*I-induced migratory phenotype could be reversed using a pharmacological approach, wound healing assays were conducted following treatment with AKR1C1 and AKR1C3 inhibitors under varying O_2 concentrations. As demonstrated in Figure 16.1(A), HPV16-E6*I-overexpressing cells treated with the AKR1C1 inhibitor no longer exhibited enhanced wound closure under hyperoxic or hypoxic conditions, contrasting with the untreated HPV16-E6I-overexpressing cells observed previously. Similarly, AKR1C3 inhibition (Figure 16.1(B)) suppressed the accelerated migration seen in HPV16-E6*I-overexpressing cells. Quantitative analysis of cell front velocity at 14 hours post-scratch confirmed that both AKR1C1 and AKR1C3 inhibitors significantly reduced the enhanced migratory phenotype observed in HPV16-E6*I-overexpressing cells under hyperoxia and hypoxia. This reversal indicates that AKR1C activity plays a key role in mediating the O_2-sensitive migration and proliferation phenotypes induced by HPV16-E6*I. Importantly, no significant increase in migration velocity was observed in control cells upon inhibitor treatment, indicating a selective effect on the HPV16-E6*I-driven phenotype. These findings support the conclusion that pharmacological inhibition of AKR1C1 and AKR1C3 is sufficient to attenuate the enhanced migration conferred by HPV16-E6*I, further implicating AKR1C enzymes in the regulation of HPV-mediated cell motility under varying O_2 tensions.

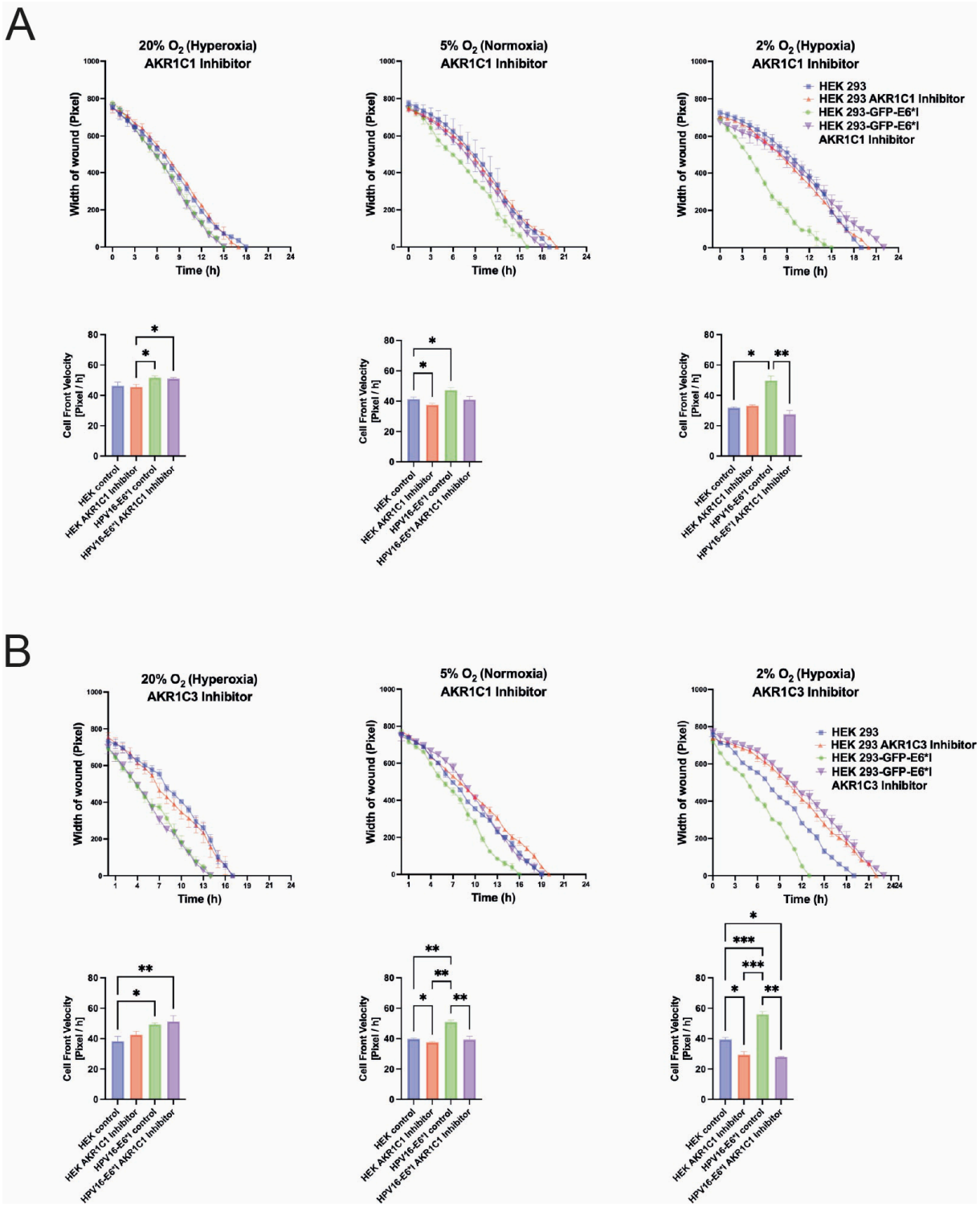

Figure 16: Wound healing assay to assess the impact of AKR1C1 and AKR1C3 inhibition on proliferation and migration of HPV16-E6*I-overexpressing cells under varying O_2 levels. Cells were preconditioned for seven days under predefined O_2 concentrations. Cells were seeded into culture inserts 24 hours prior to the start of the assay. At t_0, the inserts were removed to create a standardised wound gap and wound closure was monitored hourly until confluence was reached. Cells were treated with the respective inhibitors before the assay, and O_2 conditions were maintained throughout. (A) Wound healing assays conducted under 20% O_2, normoxic 5% O_2, and 2% O_2

conditions in the presence of an AKR1C1 inhibitor. (B) Wound healing assays conducted under identical O_2 conditions with AKR1C3 inhibitor treatment. Cell front velocities were calculated 14 hours post-scratch. The data presented are the mean ± SD from three technical replicates. Statistical significance was assessed using two-way ANOVA followed by Tukey's post hoc test. Significance thresholds were defined as $p \leq 0.05$, $p \leq 0.01$, and $p \leq 0.001$.

6.11 Differential modulation of OS genes by HPV16-E6 and -E6*I in cell culture models under variable O_2 conditions

To investigate how HPV16-E6 and its splice variant HPV16-E6*I remodel the OS transcriptome, cell culture models were incubated for seven days under defined O_2 conditions as described earlier in Section 2.6. Absolute transcript levels of NRF2, AKR1C1, AKR1C2, and AKR1C3 - key genes involved in ROS metabolism - were quantified using droplet digital PCR (ddPCR), a highly sensitive method that allows precise detection of isoform- and O_2-dependent transcript changes (Figure 17). NRF2, a master transcription factor that coordinates antioxidant and detoxification programmes in response to ROS, was significantly upregulated in HPV16-E6*I-overexpressing cells at hypoxia and normoxia. In contrast, HPV16-E6 increased NRF2 expression only at hyperoxia. These findings indicate distinct, O_2-dependent regulatory effects of the two viral isoforms on NRF2 expression. AKR1C1 expression remained low across all O_2 conditions in HPV16-E6*I-overexpressing cells but was strongly induced by HPV16-E6-overexpressing cells, particularly at hyperoxia, suggesting that full-length HPV16-E6, rather than HPV16-E6*I, drives AKR1C1-associated metabolic rewiring. In contrast, AKR1C3 was significantly upregulated by HPV16-E6*I under hypoxic conditions; full-length HPV16-E6 only produced a modest increase. At normoxia, HPV16-E6-overexpressing cells repressed AKR1C3, whereas HPV16-E6*I overexpressing cells showed an upward trend. At hyperoxia, both isoforms reduced AKR1C3 expression below control levels, pointing to a hypoxia-specific regulatory effect mediated by HPV16-E6*I. AKR1C2 followed a pattern similar to AKR1C3, supporting their potential co-regulation under HPV16-E6*I influence. Taken together, these data reveal distinct and sometimes opposing roles of HPV16-E6 and -E6*I in modulating OS gene expression. While both isoforms exert some regulatory

influence, HPV16-E6*I emerges as the principal driver of ROS metabolism under hypoxic conditions. This supports a model in which the two isoforms may act in a predominantly antagonistic manner to fine-tune redox balance and metabolic adaptation in HPV^+ cells.

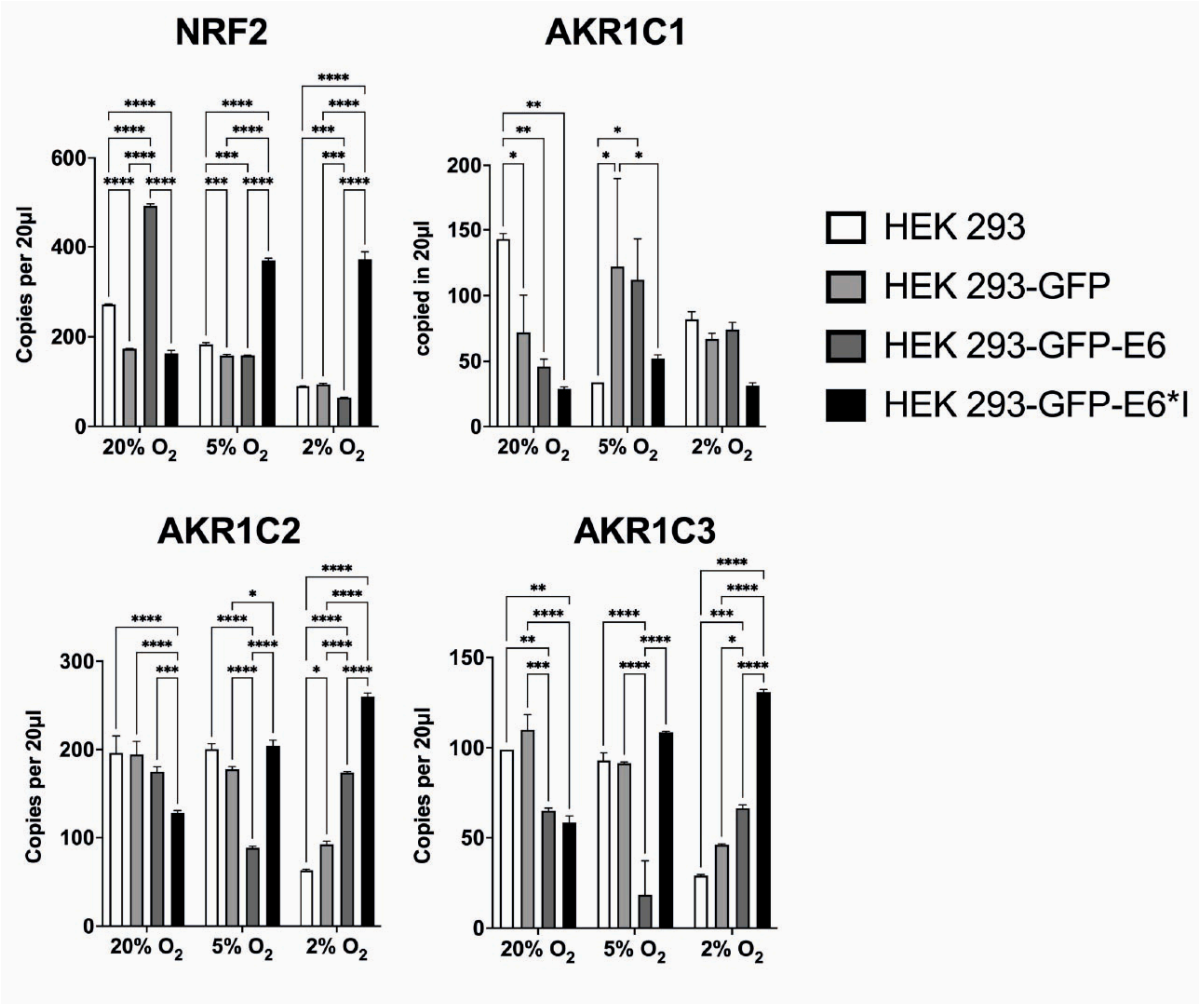

Figure 17. Quantitative profiling of OS transcripts under variable O_2 conditions. ddPCR was performed on cDNA from cell culture models incubated for seven days under varying O_2 levels as indicated. Absolute transcript counts for NRF2 and AKR1C1, AKR1C2, AKR1C3 were measured and expressed as copy number per 20 µl ddPCR reaction. Bars represent the mean ± SD of three technical replicates. The experiment was independently repeated as biological duplicates; a representative dataset is shown. Statistical significance was assessed using two-way ANOVA followed by Tukey's post hoc test. Significance thresholds were defined as $p \leq 0.05$, $p \leq 0.01$, and $p \leq 0.001$.

6.12 Evaluation of ROS biomarkers NRF2 and AKR1C3 in cell models cultured under variable O_2 conditions

6.12.1 Western-Blot Evaluation of NRF2 and AKR1C3 Protein Levels in Cell Models Cultured Under Variable O_2 Conditions

NRF2 and AKR1C3 protein levels were assessed in the HEK 293 models after seven days under the previously described O_2 conditions. AKR1C1 remained undetectable by Western blot (data not shown). As shown in Figure 18(A), NRF2 was barely detectable across all models at hyperoxia. A pronounced increase was observed specifically in HPV16-E6*I-overexpressing cells at normoxia, while control and HPV16-E6-overexpressing cells showed only minimal changes. At hypoxia, NRF2 levels returned to near baseline. Densitometry normalized to HPRT-1 (Figure 18.1(A) – (B)) confirmed this distinct NRF2 peak in HPV16-E6*I-overexpressing cells.

AKR1C3 exhibited a different pattern: its expression rose sharply in HPV16-E6*I-overexpressing cells at hyperoxia but showed only slight variation in the other lines. At normoxia and hypoxia, AKR1C3 levels decreased consistently across all models. Quantification corroborated these results, and the uniform HPRT-1 bands verified correct loading and transfer. These findings indicate that NRF2 and AKR1C3 are differentially regulated in an O_2-dependent manner, with HPV16-E6*I expression conferring distinct responsiveness.

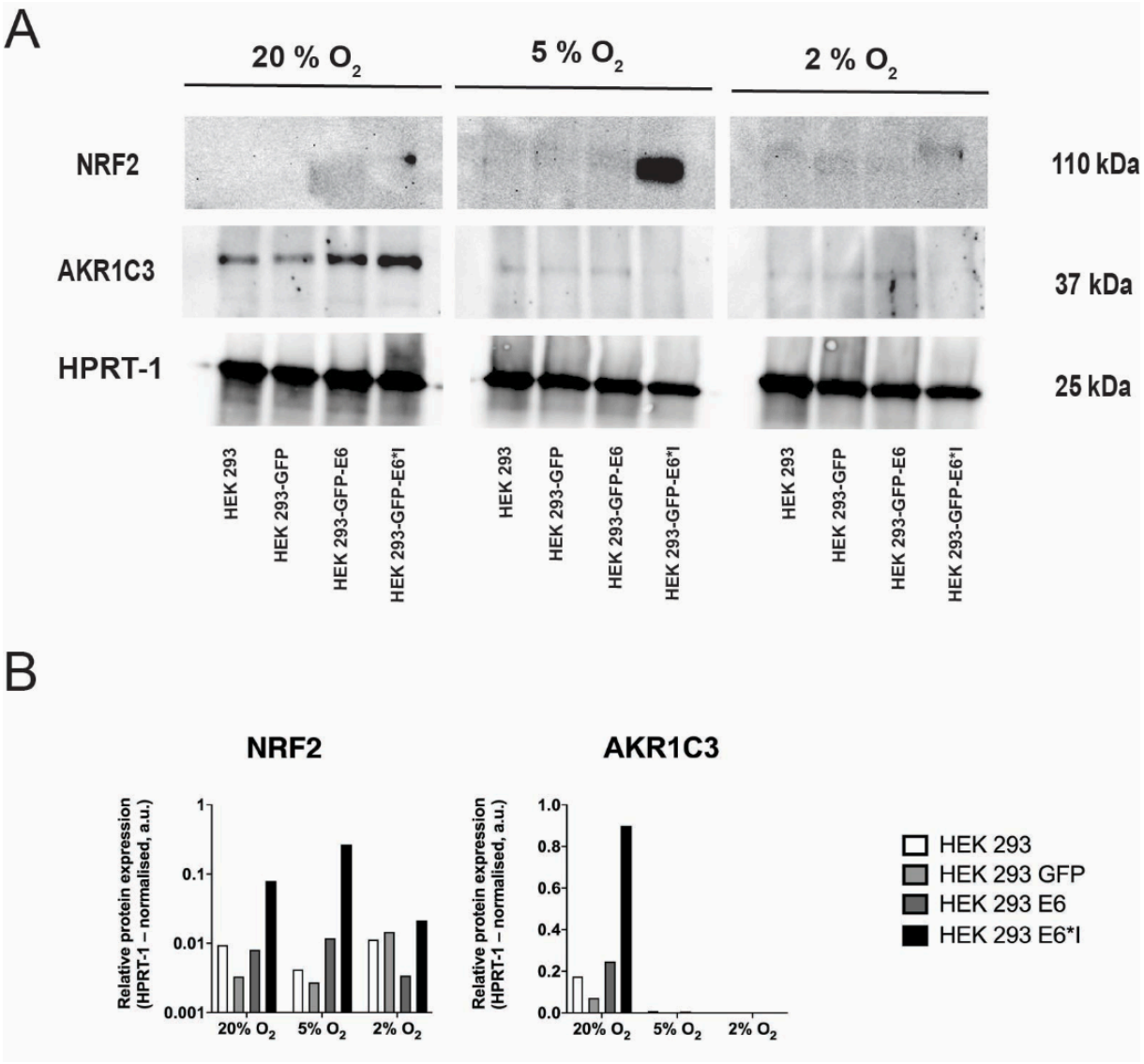

Figure 18.1. Western blot analysis and densitometric assessment of ROS biomarkers subjected to graded O_2 levels. Figure 18.1. Western blot analysis and densitometric assessment of ROS biomarkers subjected to graded O_2 levels. (A) Immunoblots showing NRF2 and AKR1C3 from HEK293 derivatives (HEK 293, HEK 293-GFP, HEK 293-E6 and HEK 293-E6*I), which were cultured for seven days in an atmosphere containing 20%, 5% or 2% O_2. SDS-PAGE was used to separate equal amounts of protein (25 µg per lane), which was then transferred to nitrocellulose and probed with the antibodies shown. HPRT-1 was used as a loading control. (B) Densitometric measurement of band intensities adjusted to HPRT-1 and shown as relative protein expression (arbitrary units (a.u.)). NRF2 expression is low at 20% O_2, peaks selectively in HPV16-E6*I at 5% O_2, and returns towards baseline at 2% O_2. AKR1C3 expression is high in HPV16-E6*I at 20% O_2 and decreases with lower O_2 levels. Uniform HPRT-1 verifies stable loading and transfer. The experiments were performed as separate biological duplicates or triplicates (n = 2–3). The blots and graphs shown here are from one biological replicate

6.12.2 Immunofluorescent Evaluation of NRF2 and AKR1C3 Protein Expression in Cell Models across Variable O_2 Levels

As previously described, NRF2 functions as a master transcriptional regulator of cellular antioxidant response (Huebbers et al. 2019). To assess the effect of high-level HPV16-E6*I expression on NRF2 activation under OS, immunofluorescence staining was performed in cell culture models preconditioned for seven days under defined O_2 concentrations. Confocal imaging followed by cell-size-normalised fluorescence quantification in Fiji (ImageJ®) revealed a marked increase in nuclear NRF2 signal in HPV16-E6*I-overexpressing cells compared to both HPV16-E6-overexpressing and control cells, specifically under hypoxic conditions (Figure 18.2). These results suggest that HPV16-E6*I enhances NRF2 cytoplasmic accumulation in response to hypoxia-induced OS.

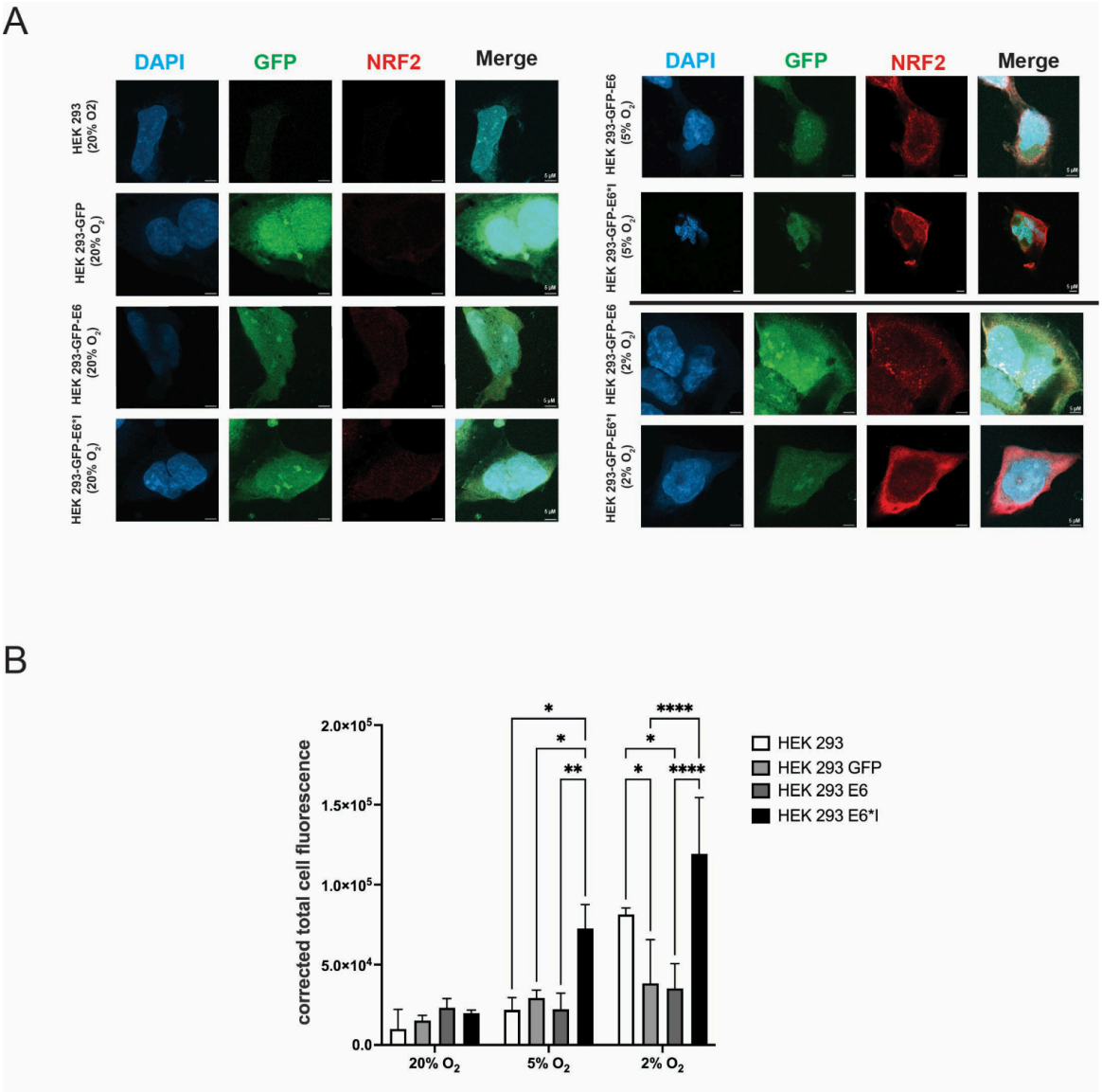

Figure 18.2. Hypoxia significantly increases NRF2 levels in HPV16-E6*I-overexpressing cell culture models. (A) Representative confocal images of the indicated cell lines immunostained for NRF2 after seven days of incubation under defined O_2 concentrations; scale bar = 5 µm. (B) Quantification of corrected NRF2 fluorescence intensity. Statistical significance was assessed using two-way ANOVA followed by Tukey's post hoc test. Bars represent the mean ± SD of three randomly chosen viewing fields. Statistical significance : * $p \leq 0.05$; ** $0.01 > p \geq 0.001$; *** $0.001 > p \geq 0.0001$; **** $p \leq 0.0001$.

Building on these findings, we next examined AKR1C3, a downstream target of NRF2 and a key enzyme involved in OS adaptation (Huebbers et al. 2019). The same O_2 conditioning protocol and analytical procedures were applied as indicated above. Confocal imaging and Fiji-based fluorescence quantification revealed a pronounced induction of AKR1C3 in HPV16-E6*I-overexpressing cells, most prominently under

hypoxic conditions, when compared with both HPV16-E6-overexpressing and control cells (Figure 18.3). Building on these findings, we next examined AKR1C3, a downstream target of NRF2 and a key enzyme involved in OS adaptation.

Under hyperoxia, HPV16-E6*I-overexpressing cells exhibited a significantly elevated level of AKR1C3 fluorescence in comparison to control cell lines, and HPV16-E6-overexpressing cells. A similar pattern was seen under normoxic conditions, where AKR1C3 levels in HPV16-E6*I-overexpressing cells remained increased above both HPV16-E6-overexpressing and control lines, but with significantly reduced intensity compared to hyperoxia. Under hypoxia, there was a significant increase in AKR1C3 expression in HPV16-E6*I-overexpressing cells. These cells exhibited the most intense fluorescence in the cytoplasm when compared to all the other groups and circumstances.

In contrast, control cell lines and HPV16-E6-overexpressing cells demonstrated relatively consistent, diminished levels of AKR1C3 expression across varying O_2 conditions, with only marginal increases observed under hypoxic settings. The research findings showed that HPV16-E6*I-overexpressing cells trigger a significant, O_2-sensitive increase in AKR1C3 levels in the cytoplasm, with peak expression levels being reached during periods of hypoxia. The observations support the hypothesis that, particularly in conditions of hypoxia, HPV16-E6*I enhances the NRF2 pathway, leading to increased production of cytoprotective enzymes, such as AKR1C3, in response to OS.

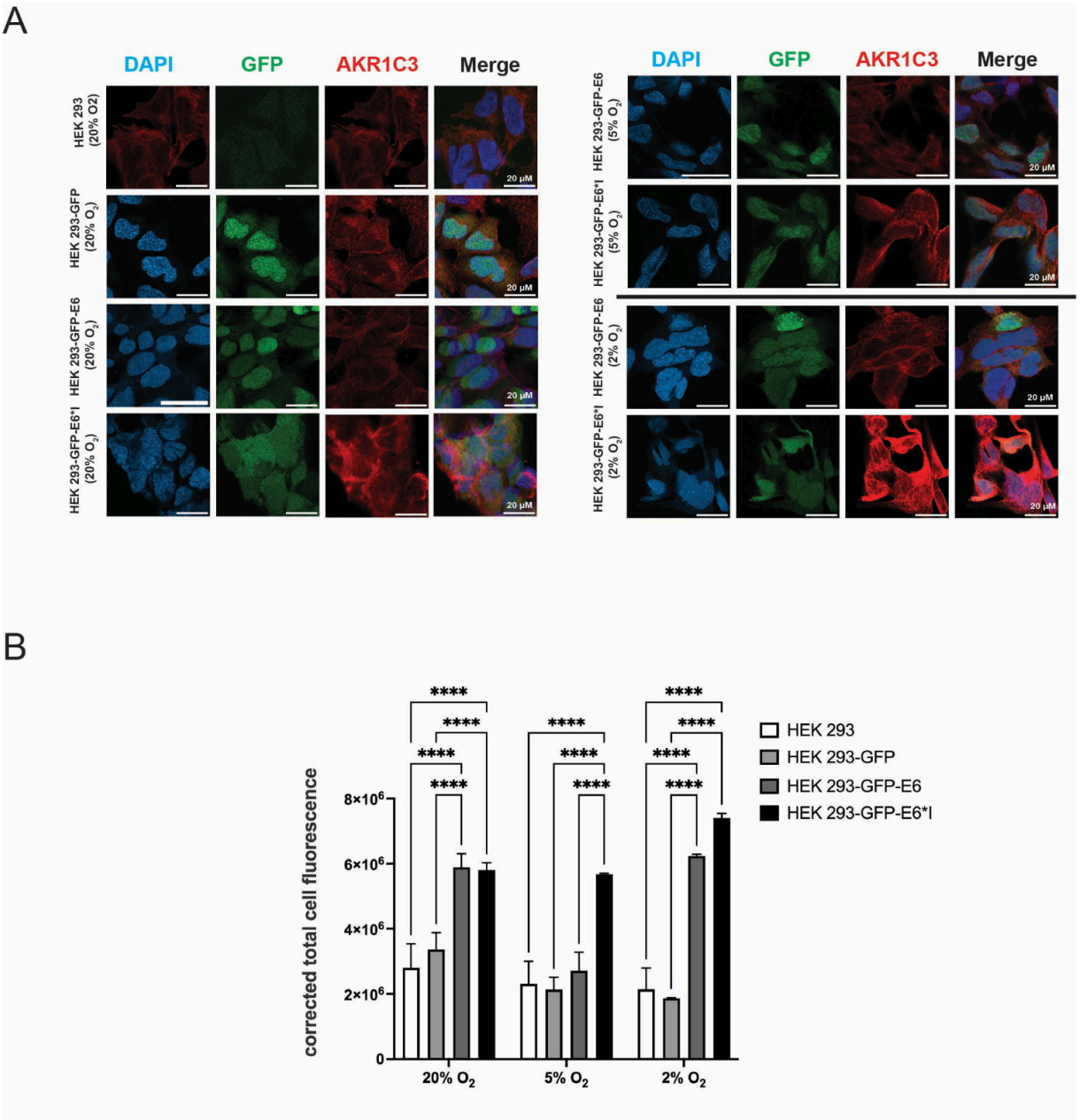

Figure 18.3 AKR1C3 levels are increased in HPV16-E6*I-overexpressing cell culture model under hypoxia (A) Representative confocal images of cells immunostained for AKR1C3 after seven days of exposure to defined O_2 levels; scale bar = 5 µm. (B) Quantified AKR1C3 fluorescence, and bars represent the mean ± SD of three randomly chosen viewing fields. Statistical significance was assessed using two-way ANOVA followed by Tukey's post hoc test. Statistical significance: * $p \leq 0.05$; ** $0.01 > p \geq 0.001$; *** $0.001 > p \geq 0.0001$; **** $p \leq 0.0001$.

6.13 Measurement of mitochondrial ROS in O_2-conditioned cell culture models

To assess whether the observed expression and protein activity changes transcriptional and protein alterations were accompanied by changes in mitochondrial OS, we performed the MitoSOX™ Red assay on cell culture models preconditioned under defined O_2 concentrations. Mitochondrial superoxide levels were measured using a multimode plate reader, with fluorescence intensities normalized to cell number via Hoechst 33342 nuclear staining (Figure 19(A). These measurements were independently corroborated by confocal microscopy (Figure 19(B), (C) and (D)). Across all O_2 conditions, HPV16-E6*I-overexpressing cells consistently exhibited significantly higher mitochondrial ROS levels compared to both HPV16-E6 and control models. These findings suggest that the increased NRF2 and AKR1C3 activity observed in previous sections coincides with a measurable elevation in mitochondrial ROS. This supports the notion that HPV16-E6*I expression perturbs redox homeostasis and induces OS within mitochondria, further underscoring the splice variant’s role as a potent modulator of redox signaling.

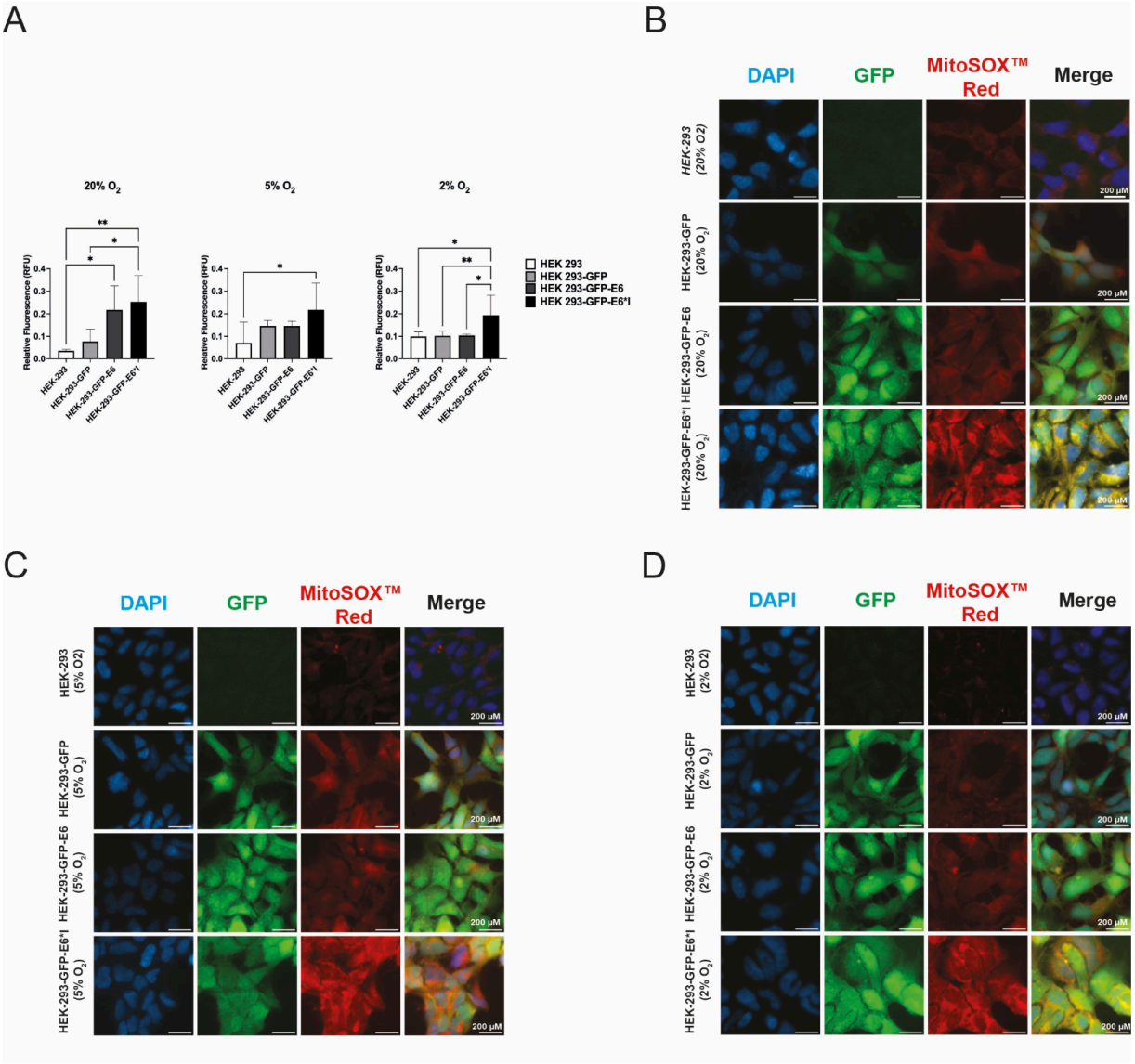

Figure 19. Mitochondrial ROS levels are elevated by HPV16-E6*I expression. (A) Quantification of MitoSOX™ Red fluorescence intensity in cell culture models (HEK 293, HEK 293-GFP, HEK 293-GFP-E6, and HEK 293-GFP-E6*I) after seven days of exposure to defined O_2 concentrations (20%, 5%, and 2% O_2). Data represent mean ± SD of seven technical replicates. The experiment was independently conducted in 3 biological replicates; a representative dataset is shown. Statistical analysis: two-way ANOVA with post hoc testing. Significance: *p ≤ 0.05, **p ≤ 0.01, ***p ≤ 0.001, ***p ≤ 0.0001. (B–D) Representative confocal images of cells stained with MitoSOX™ Red to detect mitochondrial ROS under different O_2 conditions. Following fixation with 4% paraformaldehyde, nuclei were counterstained with DAPI. Images were acquired with a Zeiss AxioObserver microscope (Carl Zeiss Microscopy, Germany). Scale bar = 50 µm. (B) 20% O_2 condition. (C) 5% O_2 condition.(D) 2% O_2 condition.

6.14 Evaluation of bioenergetic parameters in HEK 293 cell models under varying O_2 levels using the Seahorse XF Analyzer

The Seahorse XF Analyzer was employed to functionally assess metabolic alterations induced by HPV16-E6*I expression. Specifically, the oxygen consumption rate (OCR) and the extracellular acidification rate (ECAR) were measured in the cell-culture models treated at predefined O_2 concentrations. These parameters provided quantitative insight into mitochondrial respiration and glycolytic flux, respectively. Analysis of OCR (Figure 20(A)) revealed increased mitochondrial respiratory activity in HPV16-E6*I-overexpressing cells compared to control models, particularly at baseline and across several time points. Moreover, ECAR measurements (Figure 20(B)) demonstrated an elevated glycolytic activity in HPV16-E6*I-overexpressing cells relative to controls. To further dissect mitochondrial function, key parameters were evaluated: mitochondrial activity, respiration, maximum respiration, ATP generation, proton leak, and baseline extracellular acidification (Figure 20(B)). Cells expressing HPV16-E6*I exhibited significantly elevated basal respiration and ATP production compared to other cell lines. Basal extracellular acidification was also markedly increased in HPV16-E6*I-overexpressing cells. In contrast, maximal respiration and proton leak did not show statistically significant differences across models. Collectively, these findings suggest that HPV16-E6*I enhances mitochondrial bioenergetic capacity, promoting both basal respiratory activity and ATP generation, while simultaneously increasing glycolytic output.

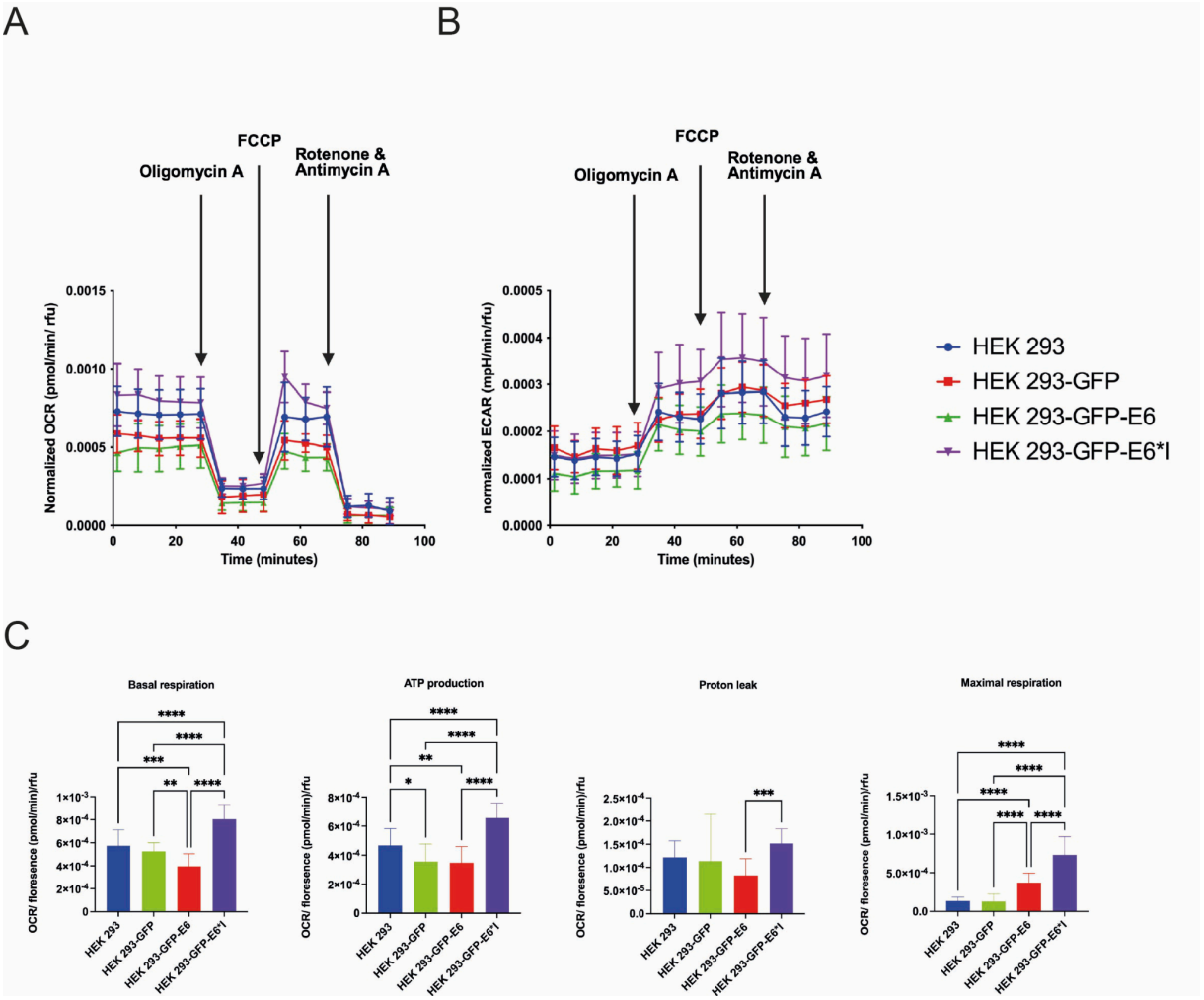

Figure 20. HPV16-E6*I enhances mitochondrial respiration and glycolysis in HEK 293 cell models. (A) Seahorse XF Analyzer assessment of OCR (B) ECAR over time in cell culture models under varying O_2 conditions. Each point represents the mean ± SD of 24 technical replicates. (B) Quantification of mitochondrial function parameters: basal respiration, ATP production, maximal respiration and proton leak. Bars represent mean ± SD of 24 technical replicates. Data shown are representative of three independent biological experiments. Statistical analysis: two-way ANOVA with post hoc testing. Significance: *p ≤ 0.05, **p ≤ 0.01, ***p ≤ 0.001, ***p ≤ 0.0001.

6.15 Assessment of HPV16-E6*I-induced changes in metabolic transcripts using ddPCR

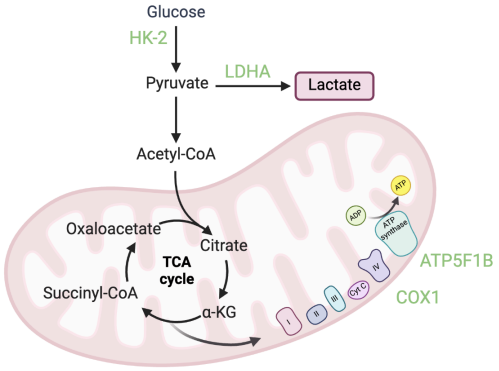

Figure 21.1. Schematic representation of key enzymes linking glycolysis, pyruvate metabolism, and mitochondrial oxidative phosphorylation (OXPHOS). HK-2 phosphorylates glucose, initiating glycolysis. Pyruvate can be converted to lactate via LDHA or enter mitochondria, where the pyruvate dehydrogenase complex produces acetyl-CoA for the TCA cycle. Within the electron transport chain (ETC), COX1 (Complex IV) mediates electron transfer to oxygen, while ATP5F1B (Complex V) catalyzes ATP production via proton-driven phosphorylation. Created in https://BioRender.com.

To investigate whether HPV16-E6 and its splice variant -E6*I supports a metabolic shift toward glycolysis or mitochondrial OXPHOS, selected mRNA transcripts of genes involved in central carbon metabolism were profiled by ddPCR. The glycolytic arm of the panel comprised HK-2, which catalyses the entry step of glycolysis, PKM2, which controls the terminal pyruvate-producing step, and LDHA, which converts pyruvate to lactate. For mitochondrial respiration, expression levels of COX1, a subunit of cytochrome c oxidase (Complex IV), responsible for the terminal transfer of electrons to oxygen in the electron transport chain (ETC) and ATP5F1B, the β-subunit of ATP synthase (Complex V), essential for ATP production via proton-driven phosphorylation during OXPHOS) were assessed (Figure 21.1). Cell culture models were pre-treated for seven days under defined O_2 concentrations, after which ddPCR was performed to determine the absolute transcript levels with high analytical sensitivity (Figure 21.2). Interestingly, hypoxic conditions led to a

significant upregulation of HK-2, COX1, and ATP5F1B transcripts in HPV16-E6*I-overexpressing cells, suggesting a coordinated enhancement of both glycolytic and mitochondrial energy pathways. In contrast, the same transcripts were significantly repressed by full-length HPV16-E6, particularly under hypoxia, implying divergent and potentially antagonistic metabolic reprogramming by the two isoforms.

These results reinforce the notion that HPV16-E6*I, rather than HPV16-E6, actively promotes a flexible metabolic phenotype, enhancing both anaerobic and oxidative metabolism under hypoxic stress - potentially supporting cell survival and proliferation in the hypoxic tumour microenvironment.

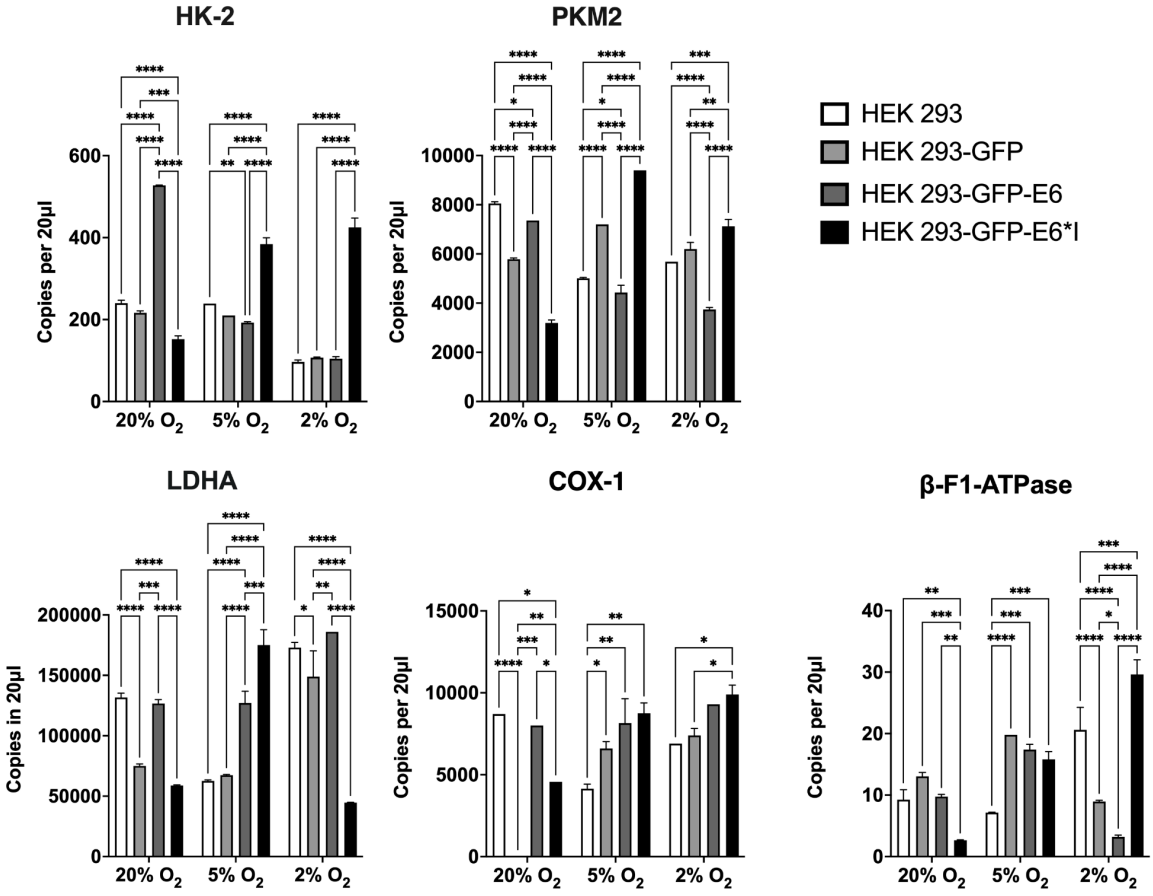

Figure 21.2. Quantitative ddPCR analysis of metabolic gene transcripts under varying O_2 conditions. Cell culture models were incubated for seven days under predefined O_2 concentrations as indicated. Total RNA was reverse-transcribed and analysed via ddPCR to determine the absolute copy numbers per 20 µL reaction for HK-2, PKM2, LDHA, COX1 and ATP5F1B (Complex V). Bars represent mean ± SD of three technical replicates. The experiment was repeated as biological

duplicates, and a representative data set is shown. Statistical significance: * $p \leq 0.05$; ** $0.01 > p \geq 0.001$; *** $0.001 > p \geq 0.0001$; **** $p \leq 0.0001$.

6.16 Western-Blot Evaluation of Glycolytic and Mitochondrial Protein Levels in Cell Models Cultured Under Variable O_2 Conditions

Protein levels of HK-2, PKM2, LDHA, and β-F1-ATPase were assessed in HEK 293 cell culture models after culturing for seven days at predefined O_2 conditions (Figure 22(A) – (B)). HK-2 was strongly upregulated in HPV16-E6*I-overexpressing cells at hyperoxia but decreased markedly at lower O_2 across all cell lines. PKM2 showed the same pattern, with highest levels in HPV16-E6*I-cells under hyperoxia and reduced expression at normoxia and hypoxia. LDHA was detectable under all conditions, with moderately increased expression at hypoxia, particularly in HEK 293 and HEK 293-GFP controls. β-F1-ATPase was highest in HPV16-E6*I cells at hyperoxia but declined in all models under reduced O_2. These data suggest O_2-dependent regulation of glycolytic and mitochondrial proteins, with HPV16-E6*I conferring a distinct hyperoxic response.

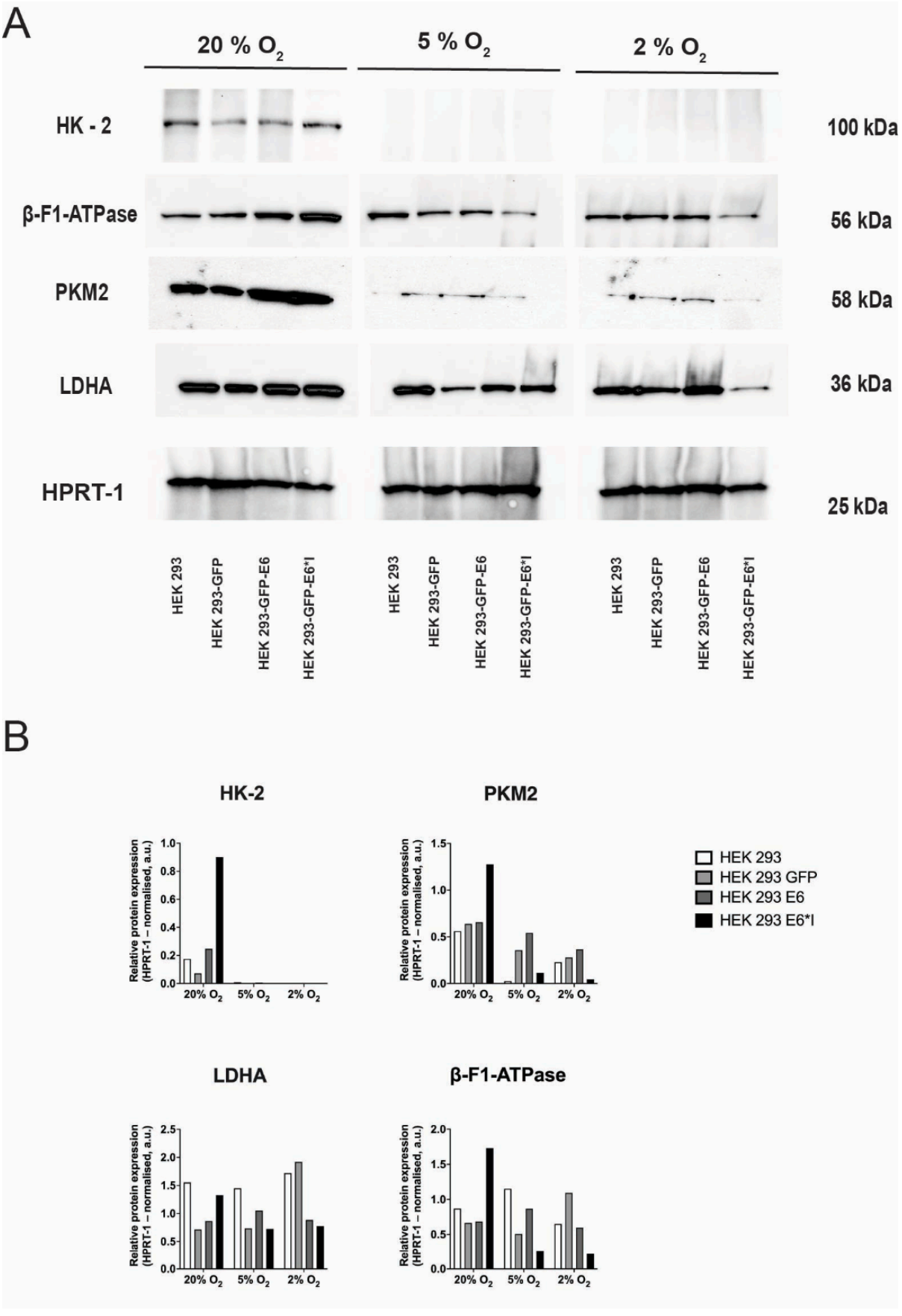

Figure legend in next page

Figure 22. **Western-blot analysis alongside a densitometric evaluation of metabolic markers under varying O_2 levels.** (A) Immunoblots display HK-2, PKM2, LDHA, and β-F1-ATPase from cell culture models incubated for seven days under 20%, 5%, or 2% O_2 conditions. Equal amounts of protein (25 µg per lane) were subjected to SDS-PAGE. HPRT-1 was used for loading control. (B) Densitometric quantification of band intensities was normalised to H and expressed as relative protein expression in arbitrary units (a.u.). Under various conditions, HK-2, PKM2, and β-F1-ATPase signals are most pronounced in HPV16-E6*I at 20% O_2, showing a decrease under hypoxic conditions (5–2% O_2). LDHA is consistently detectable across all conditions, exhibiting slight variations associated with hypoxia. Experiments were conducted as independent biological duplicates or triplicates (n = 2–3); the blots and graphs presented are representative of a single biological replicate.

6.17 O_2-driven shifts in glucose uptake, lactate production, and ATP yield reveal distinct metabolic signatures of HPV16-E6 and HPV16-E6*I in cell culture models.

Modulating the O_2 concentration induced significant metabolic adaptations in cell culture models. As detailed in section 5.5.4, these changes were quantified using Promega assays—CellTiter-Glo® for intracellular ATP levels, Glucose Uptake-Glo™ for glucose uptake, and Lactate-Glo™ for extracellular lactate production. Luminescent signals were recorded using a CLARIOstar® plate reader with orbital averaging to ensure precision and reproducibility.

6.17.1 Glucose uptake:

A marked increase in glucose uptake was observed in all cell culture models exposed to normoxia or hypoxia compared to those maintained at hyperoxia (Figure 23(A)). Under normoxia, this increase was particularly pronounced in HPV16-E6-overexpressing cells, which exhibited approximately threefold higher glucose uptake than the other models. Although glucose absorption was reduced under hypoxia compared to normoxia, levels remained elevated relative to hyperoxia across all conditions. Notably, HPV16-E6*I cells demonstrated the highest glucose uptake at hypoxia, suggesting a shift in their metabolic preference under more severe hypoxia.

6.17.2 Lactate production:

Lactate accumulation increased by approximately tenfold in response to 5% and 2% O_2 exposure, consistent with enhanced glycolytic flux (Figure. 23(B)). However, there were no significant differences in lactate output between the four cell culture models, indicating that neither HPV16-E6 nor -E6*I expression enhanced lactate secretion beyond the effect of hypoxia alone.

6.17.3 ATP levels:

At hyperoxia, HPV16-E6*I-overexpressing cells produced significantly more ATP than all other models, indicating enhanced OXPHOS (Figure. 23(C)).

In conclusion, these results demonstrate that both HPV16-E6 isoforms and ambient O_2 concentration shape the metabolic state of the cell. HPV16-E6 enhances glucose uptake particularly at normoxia, while HPV16-E6*I confers a selective advantage by promoting ATP production under hyperoxia. However, this benefit is abolished under more severe hypoxia. Collectively, the data suggest distinct, O_2-dependent bioenergetic functions for HPV16-E6 and HPV16-E6*I.

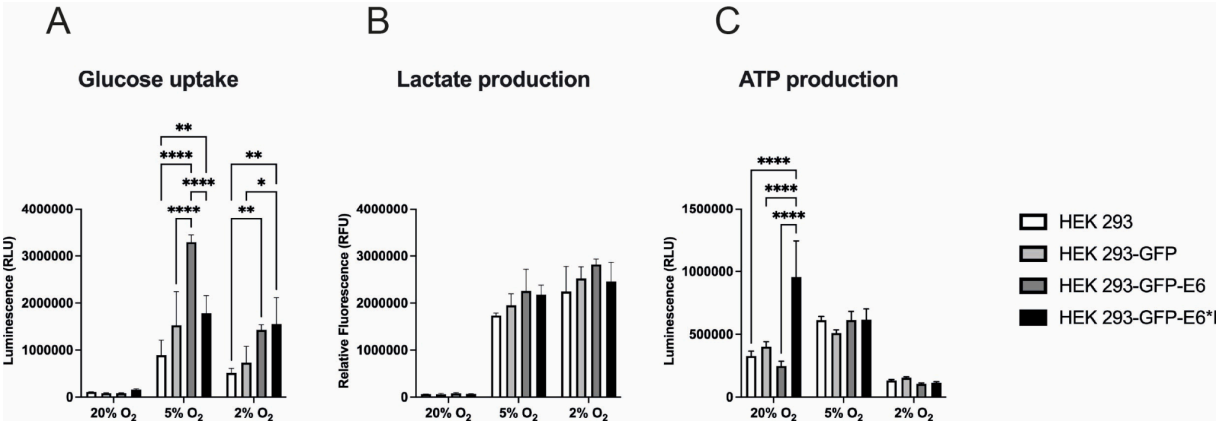

Figure 23: O_2-dependent effects of HPV16-E6 and E6I on bioenergetic parameters in cell culture models. (A) Glucose uptake , (B) lactate production and (C) intracellular ATP levels were quantified in cells incubated for 7 days under defined O_2 conditions. Glucose uptake and ATP content were assessed using luminescence-based assays (reported as relative light units (RLU)), whereas lactate release was measured using fluorometry (reported as relative fluorescence units (RFU)). Data represent mean ± SEM of three biological replicates, each performed in technical triplicate. Statistical significance was assessed using a two-way ANOVA followed by a Tukey's multiple comparison test (*p < 0.05, **p < 0.01, ****p < 0.0001).

6.18 RNA-FISH Probe Validation in Fixed UD-SCC-2 Cells for Subsequent FFPE Application

RNA-FISH was developed to spatially and quantitatively assess the expression of HPV16-E6 and HPV16-E6*I transcripts in FFPE patient samples. This approach aims to link viral integration status with HPV16-E6*I-mediated redox and metabolic reprogramming observed in cell culture models, thus translating mechanistic findings into clinically relevant tissue contexts. For initial assay validation, paraffin-embedded UD-SCC-2 cells, known to express both HPV16-E6 and HPV16-E6*I at comparable levels, were used. This served to verify both probe specificity and transcript localization (Figure 24). A Cy5-labelled probe targeting the exon unique to the unspliced HPV16-E6 transcript produced a signal exclusively in the Cy5 channel. Conversely, a DsRed-labelled probe spanning the HPV16-E6*I-specific splice junction yielded signal exclusively in the DsRed channel, indicating specific detection of the spliced isoform. Negative controls, including a scrambled probe and a no-probe condition, yielded no detectable fluorescence, confirming minimal background and high hybridization specificity. A β-actin probe (DsRed-labelled) served as an internal positive control, producing consistent signal in all cells, thereby confirming effective hybridization and appropriate imaging settings. Nuclei were counterstained with DAPI (blue). The signal intensities for Cy5 and DsRed were comparable, consistent with the ~1:1 E6:E6*I transcript ratio previously quantified by RT-qPCR. Both isoforms localized predominantly to the cytoplasm, consistent with the distribution of mature mRNA transcripts. Taken together, these findings confirm that each probe selectively detects its intended target isoform, with minimal off-target binding or autofluorescence. Furthermore, UD-SCC-2 cells maintain stable, isoform-specific expression levels, validating their use as a control for subsequent analyses in FFPE patient tissue.

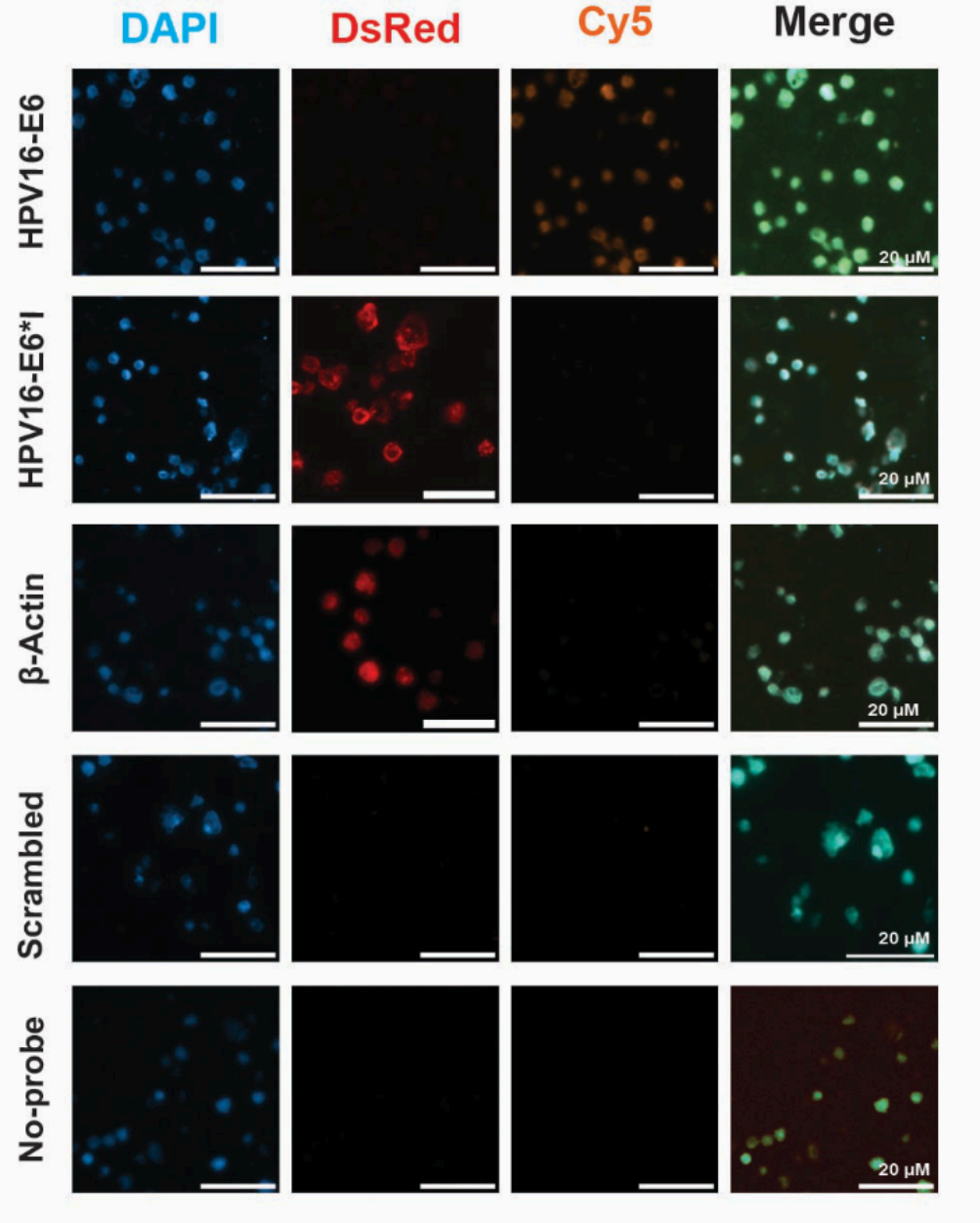

Figure 24. Validation of HPV16-E6 and -E6*I RNA-FISH probes in FFPE-fixed UD-SCC-2 cells. LNA RNA-FISH was performed using probe sets specific for HPV16-E6 (Cy5) and HPV16-E6*I (DsRed). Nuclei were counterstained with DAPI (blue). A β-actin probe (DsRed) served as a positive control. Scrambled-sequence and no-probe controls were included to assess nonspecific hybridization and background autofluorescence, respectively. Images were acquired with a Zeiss AxioObserver microscope (Carl Zeiss Microscopy, Germany) and are displayed in individual fluorescence channels and as a composite. Rows represent experimental conditions; columns show single-channel and merged images, as indicated.

7 Discussion

7.1 TLA/FFPE-TLC enables precise, unbiased mapping of HPV integration in oropharyngeal carcinoma.

Section 7.1 was adapted from (Demers, Balaji et al., 2024).

The integration of HPV DNA into the host genome is a hallmark of HPV-driven OPSCC. However, the functional implications and prognostic relevance of these integration events remain incompletely understood. One major limitation has been the lack of suitable methods for reliable detection of viral-host fusion sites, especially in FFPE tissues. Traditional assays often suffer from limited sensitivity, bias toward known junctions, or incompatibility with degraded nucleic acids. To address these limitations, we invented a proximity ligation-based long-read sequencing approach (TLA) and it's adaption for FFPE tissue (TLC) that enables high-resolution, unbiased mapping of HPV integration directly from FFPE specimens. This method represents a significant technical advance and provides, for the first time, a comprehensive overview of integration patterns in routinely archived OPSCC samples. The FFPE-TLC approach represents a significant methodological advance, addressing a long-standing gap in the literature. It provides a reliable and unbiased method for the integration analysis of highly fragmented FFPE DNA, thereby enabling robust investigation of HPV host genome integration status in real-world diagnostic specimens.

7.1.1 Methodological development: long-read proximity ligation assays (TLA/FFPE-TLC) surpass traditional tests.

This approach reliably identifies viral-host breakpoints and maps SVs (structural variations) adjacent to the insertion site, without knowledge of the viral integration locus. This is achieved by collecting and sequencing continuous genomic regions that are hundreds of kbs long. Proof-of-concept analyses in cell lines and FFPE OPSCC samples demonstrated that integration sites and related SVs could be located precisely. Notably, FFPE-TLC identified identical integration breakpoints in primary tumours and distant metastases. A direct comparison with a traditional method was

performed on clinical samples: DIPS-PCR was previously applied to 23 out of 27 FFPE OPSCCs that were later analysed by FFPE-TLC. 13 tumours exhibited identical fusion patterns with both assays, while 6 displayed the same fusions plus additional sites with FFPE-TLC. In 4 cases, DIPS-PCR reported breakpoints that were not captured by FFPE-TLC. Potential explanations for this include mis-mapping of short, non-specific DIPS amplicons, the conservative breakpoint-calling criteria used for TLC, or intra tumour heterogeneity, given that DIPS was performed on fresh-frozen tissue, whereas TLC used FFPE blocks from adjacent regions. All FFPE-TLC-specific breakpoints were validated by targeted PCR and Sanger sequencing. Furthermore, digestion with alternative restriction enzymes reproduced the same integration profiles, underscoring the robustness and reproducibility of the FFPE-TLC method. It is evident from the above comparisons that the pipeline is able to identify both clonal and subclonal events with high specificity and reproducibility.

7.1.2 Biological and clinical insights derived from high-resolution integration profiles

The integration characteristics uncovered by FFPE-TLC mirror the SVs observed in fresh-frozen sample series. HPV DNA was integrated in 56% of cases, which is consistent with recent reports citing frequencies of 60–75% (Balaji et al. 2021). Breakpoints were dispersed throughout the viral genome rather than clustering in E2, and most integrations were simple, involving only one or two HPV-host junctions. As reported in earlier studies, HPV integration loci frequently exhibited genomic instability, including local SVs or focal copy-number gains. Viral DNA was often inserted within or near genes implicated in DNA repair (XRCC4, BABAM2, RAD51B), epithelial-to-mesenchymal transition (EMT) (CD200, TMEM182, RAPGAP1L, ATP8A1), or oncogenic signalling or apoptosis regulation (NR4A2, HIC1, TRAF3, BCL11A, TGFBR2). Several of these genes (e.g. RAD51B, NR4A2, TGFBR2 and TRAF3) coincide with previously reported HPV integration 'hotspots' (Balaji et al. 2021). A recurrent integration site was likewise observed, located ~195 kb upstream of TP63 in the 3q28 region, previously identified by our group in three independent tumours (Olthof et al. 2014). The detection of identical integration sites in both primary tumours and and their corresponding metastatic lesions suggests a common

clonal origin, providing a potentially valuable tool for assessing clonality in routine diagnostics. Furthermore, the coexistence of unique integration events within these tumours indicates that HPV insertion is dynamic. This supports the theory that viral integration drives intratumour heterogeneity and clonal evolution by promoting aberrant DNA replication and recombination (Balaji et al. 2021). These observations are aligned with epidemiological trends in HPV^+ OPSCC (Jemal et al. 2013; Faraji et al. 2019; Lim and D'Silva 2024) and with studies showing that HPV^+ tumours progress via distinct molecular pathways (Leemans et al. 2011; Karbalaie Niya et al. 2018; Balaji et al. 2021), thereby highlighting integration as a quantifiable aspect of that heterogeneity. In summary, FFPE-TLC offers clear advantages over earlier techniques for mapping HPV integration in routinely processed tissue. Its ability to generate high-resolution fusion maps from archival FFPE blocks enables large-scale, prospective studies on the causes and consequences of HPV integration, and provides a practical tool for determining clonal relationships among HPV-associated tumours in a clinical setting. This builds on previous research from our group, which identified that HPV16 integration and HPV16-E6*I overexpression are associated with unfavourable disease outcome.

Following the establishment of this precise methodology for HPV integration mapping, we next examined how HPV16 viral oncoproteins - particularly HPV16-E6*I, which is frequently overexpressed in patient cohorts with HPV genome integration - influence metabolic and redox remodeling under physiologically relevant O_2 levels (Huebbers et al. 2019). This line of investigation is particularly relevant because metabolic reprogramming and oxidative stress are increasingly recognized as key features of HPV-driven carcinogenesis, and may interact with viral integration to promote tumour progression, therapy resistance, and clonal diversification. Understanding the contribution of HPV16-E6*I to these processes could uncover novel biomarkers or therapeutic vulnerabilities specific to integrated HPV^+ OPSCC. Accordingly, the following sections position our findings within the framework of established HPV biology (Woodman et al. 2007; Ozbun 2019; Speel 2017; Balaji et al. 2021; Demers et al. 2024; Groves et al. 2021; Campbell et al. 2018; Penning 2017; Jung et al. 2017; Cruz-Gregorio et al. 2019; Huebbers et al. 2019; Zhang et al.

2016; Vazquez-Vega et al. 2013; Umnajvijit et al. 2021; Muñoz-Bello et al. 2018; Paget-Bailly et al. 2019; Pim and Banks 2010), indicating where our data corroborate prior reports and where they refine or extend current models.

7.2 Establishing HPV16-E6/E6*I Overexpressing Cell Models and Characterising HPV$^+$ HNSCC/CSCC Lines under Differential O_2 to Probe Oxidative Stress and AKR1Cs-Driven Migration

7.2.1 Generation of cell models

In a subset of HPV$^+$ OPSCC tumours with high expression of the HPV16-E6*I splice variant, the transcriptional profiles of oxidative and metabolic stress closely resemble those observed in certain HPV$^-$ OPSCCs (Leemans et al. 2011; Zhang et al. 2016; Huebbers et al. 2019). To elucidate the molecular mechanisms underlying this similarity, we established stable in vitro models. Overexpression of HPV16-E6*I in the HEK 293 cells resulted in an 80-fold increase in HPV16-E6*I mRNA levels (mean ± SD, n = 3 biological replicates, ΔΔCt, $p < 0.001$ by two-way ANOVA), a level comparable to that observed in HPV$^+$ CSCC line CaSki. This demonstrates that the engineered cell models faithfully reproduce clinically relevant biological conditions, a key feature of their design. By contrast, the HPV$^+$ CSCC line SiHa demonstrated the lowest HPV16-E6*I expression among tested cell lines. The HPV$^+$ HNSCC cell lines, UDSCC2, UMSCC104 and UMSCC90 showed significantly higher HPV16-E6*I mRNA levels compared to 93-VU-147T, UM-SCC-47, UPCI-SCC-152 and UPCI-SCC-154. This variability is consistent with known differences in HPV16 integration status and host-pathway activation (Table. 13) (Zhang et al. 2016; Olthof et al. 2014).

Table 13: Summary of HPV$^+$ CSCC/HNSCC Cell Lines: Integration Status and HPV16-E6*I Expression Classification

	HPV$^+$ HNSCC/CSCC Cell Lines	Integration Status	HPV16-E6*I Expression
HPV$^+$ CSCC cell lines	CaSki	Yes	Very High
	SiHa	Yes	Low
HPV+ HNCC cell lines	UMSCC47	Yes	Low
	93-VU-147T	Yes	Moderate
	UD-SCC-2	Yes	High
	UM-SCC-104	Unknown	High
	UPCI-SCC090	Yes	High

This comparative landscape provides a rationale for subsequent stratified analyses based on integration status and HPV16-E6*I abundance, thereby directly linking cellular models to clinically observed heterogeneity.

*7.2.2 O_2-conditioning and its effect on HPV16-E6*I expression*

In light of the evidence that expression of HPV16-E6*I is influenced by oxidative stress (OS) and metabolic stress (Muñoz-Bello et al. 2018), O_2-controlled in vitro culture systems offer valuable insight into how it is regulated under physiologically relevant conditions. Using these physiologically relevant O_2 conditions can help to bridge the gap between observations made in vitro and the tumour microenvironment in vivo. Thus, to simulate the in vivo O_2 conditions relevant to HPV$^+$ HNSCC pathology, the transfected HEK 293 cell culture models as well as CSCC and HNSCC cell lines were pre-conditioned for 7 days under either physiological normoxia (5% O_2, reflecting the O_2 tension in healthy tonsillar mucosa) or tumour-mimicking hypoxia (2% O_2). Standard cultures maintained at 20% O_2 served as a hyperoxic reference. tumour oxygenation is a dynamic and spatially heterogeneous process in HNSCC, and fluctuations in O_2 levels can critically influence viral gene expression, cellular metabolism, and redox signaling. Prolonged exposure to both hypoxia and hyperoxia significantly upregulated spliced HPV16-E6*I mRNA expression in the CSCC cell line CaSki and in HNSCC cell lines UM-SCC-90 and 93-VU-147T. These findings indicate that both extremes of O_2 tension can promote ROS generation, stabilizing HIF-1α and

NRF2. This redox-mediated stabilization facilitates metabolic reprogramming associated with carcinogenesis and may be significantly affected by increased HPV16-E6*I expression (Cruz-Gregorio et al. 2019; Li et al. 2024). When considered alongside the Introduction (Section 3.7), these findings support the concept that HPV^+ tumours exploit redox-sensitive pathways to adapt to microenvironmental stress, with HPV16-E6*I acting as an enhancer of this response.

*7.2.3 O_2-dependent regulation of gap closure and migration by HPV16-E6*I*

To assess whether HPV16-E6*I modulates cell migration in an O_2-sensitive manner, wound-healing assays were performed under defined O_2 conditions. The experiments demonstrated that the pro-migratory and proliferative effects of HPV16-E6*I are particularly pronounced under hypoxia. Wound gaps were closed at a rate 1.4 times faster in HPV16-E6*I-overexpressing cells compared to control cells at 2% O_2 ($p < 0.001$). In contrast, only marginal increases were observed at 5% O_2 (1.06-fold, n.s.) and 20% O_2 (1.08-fold, $p \approx 0.04$). Cell-front velocity calculations further confirmed a significant motility component, particularly under hypoxic conditions. HPV16-E6*I thus appears to confer an O_2-sensitive phenotype with maximal activity in low-O_2 environments, supporting the hypothesis that this splice variant enhances cancer aggressiveness by promoting cellular motility and/or proliferation under conditions of limited oxygen and disturbed redox homeostasis (Qin et al. 2020). This behaviour, which is further enhanced under hypoxic conditions, aligns with the NRF2/AKR1C-mediated migration reported in the literature (Huebbers et al. 2019). These observations suggest that HPV16-E6*I may couple redox adaptation to invasive potential. Further studies distinguishing proliferation from motility (e.g., via vimentin assays) would help to validate this association.

*7.2.4 Specific inhibition of AKR1C rescues cell motility associated with HPV16-E6*I*

The aldo-keto reductases AKR1C1 and AKR1C3 are key regulators of redox homeostasis and lipid-derived reactive aldehyde detoxification, processes that are frequently hijacked by cancer cells to support proliferation and migration under

oxidative stress. Given their transcriptional upregulation by HPV16-E6*I and their known role in metabolic adaptation, these enzymes were investigated as potential downstream effectors of the HPV16-E6*I phenotype.

As previously reported, HPV16-E6*I transcriptionally activates AKR1C1 and AKR1C3, either directly via SP1-binding elements in their promoters, or indirectly through increased ROS metabolism (Wanichwatanadecha et al. 2012; Huebbers et al. 2019). To investigate whether selective inhibition of these enzymes could mitigate the molecular and phenotypic changes induced by HPV16-E6*I, pharmacological inhibitors were applied to HPV16-E6*I-overexpressing cell models. Treatment with the AKR1C1-selective inhibitor bromo-5-phenylsalicylic acid (5-PBSA, 2 mM) and the AKR1C3 inhibitor 3-(4-trifluoromethylphenylamino)benzoic acid (20 µM) was performed under predefined O_2 conditions.

Subsequent wound healing assays revealed that inhibition of either AKR1C1 or AKR1C3 abrogated the HPV16-E6*I-mediated enhancement of wound closure. Following inhibitor treatment, the cell-front velocity of HPV16-E6*I-overexpressing clones returned to baseline levels in both hypoxic and hyperoxic conditions (Fig. 16). These findings demonstrate that AKR1C activity is required for the O_2-sensitive, HPV16-E6*I-driven migratory/proliferative phenotype.

Collectively, the data position AKR1C1 and AKR1C3 downstream of HPV16-E6*I within an oxidative stress regulatory circuit that accelerates both ROS metabolism and cell migration. Pharmacological blockade of either enzyme reduces the motility of HPV16-E6*I-overexpressing cells, supporting their potential as therapeutic targets in HPV^+ tumours with high HPV16-E6*I expression (Wanichwatanadecha et al. 2012; Huebbers et al. 2019). From a translational perspective, these results suggest the use of combinatorial strategies that combine AKR1C inhibition with redox-modulating agents. However, it should be recognised that selectivity, dosing and off-target effects will require careful preclinical validation.

7.3 O_2-Dependent Modulation of Oxidative-Stress Pathways by HPV16- E6/E6*I

7.3.1 Transcriptional re-programming

Building on the observed O_2-dependent regulation of AKR1C enzymes and their role in mediating HPV16-E6*I-associated phenotypes, we next sought to define the broader transcriptional reprogramming of OS pathways by HPV16-E6 and -E6*I under controlled O_2 conditions. To enable accurate, parallel quantification across multiple O_2 levels and cell models, ddPCR was employed for the absolute quantification of mRNA transcripts. Absolute mRNA copies of the ROS-responsive genes NRF2, AKR1C1, AKR1C2, and AKR1C3 in the HEK 293 cell models were determined addressing the previously specified O_2 concentrations (Fig. 17). The analysis revealed three distinct O_2-dependent regulatory patterns, consistent with earlier findings from patient derived tumour samples that high HPV16-E6*I expression exhibit transcriptional signatures indicative of OS (Huebbers et al. 2019). First, NRF2, the master transcription factor governing antioxidant and detoxification responses, was significantly upregulated in HPV16-E6*I-overexpressing cell models under both normoxic and hypoxic conditions. In contrast, NRF2 expression in HPV16-E6-overexpressing cells was elevated only under hyperoxic stress. This suggests that HPV16-E6*I primes cells for redox adaptation across a broader range of O_2 tension, whereas HPV16-E6 activates NRF2 primarily under artificially hyperoxic conditions that are uncommon in physiological tissues.

Second, AKR1C1 expression was consistently downregulated in HPV16-E6*I-overexpressing cells across all O_2 levels. Conversely, it was significantly upregulated in HPV16-E6-overexpressing cells, with peak expression under hyperoxic conditions. Given AKR1C1's role in NADPH-dependent detoxification processes (Penning 2017), this pattern may reflect a compensatory mechanism in response to HPV16-E6-mediated p53 degradation and associated oxidative stress. The differential regulation implies distinct redox-metabolic reprogramming strategies employed by the two HPV16-E6 splice variants.

Third, AKR1C2 and AKR1C3 were significantly upregulated in HPV16-E6*I-overexpressing cells under hypoxic conditions, but only modestly

affected by HPV16-E6 overexpression. Under normoxia, HPV16-E6 suppressed AKR1C3 expression, whereas HPV16-E6*I induced a slight increase. Under hyperoxic conditions, both isoforms led to a reduction in AKR1C3 expression below control levels. Given AKR1C3's involvement in prostaglandin and steroid metabolism, its hypoxia-specific upregulation by HPV16-E6*I further supports the hypothesis that this splice variant modulates redox and lipid signalling pathways to promote cellular adaptation in O_2-deficient microenvironments (Penning 2017).

Together, these findings highlight the distinct O_2-dependent transcriptional programs driven by HPV16-E6 and -E6*I, underscoring the role of HPV16-E6*I in fine-tuning redox and metabolic responses in microenvironments characterized by low O_2 availability. Crucially, this HPV16-E6*I specificity mirrors the mutation-independent NRF2 activation observed in HPV^+ tumours (Campbell et al. 2018), potentially providing a mechanistic bridge between clinical observations and cellular phenotypes.

7.3.2 Protein localisation and abundance

In line with previous studies reporting elevated OS markers in HPV16-E6*I high tumours (Paget-Bailly et al. 2019; Qin et al. 2020; Williams et al. 2011), IF revealed a pronounced cytoplasmic accumulation of NRF2 in HPV16-E6*I-overexpressing cells under hypoxia. This observation aligns with the established role of NRF2 as a master regulator of cellular antioxidant defence mechanisms (Huebbers et al. 2019). Quantitative confocal analysis (Fig. 18.2(B)) demonstrated a ~4-fold increase for NRF2 in HPV16-E6*I-overexpressing cells compared to all controls and other O_2 concentrations. This suggests that the HPV16-E6*I splice variant enhances NRF2 protein levels, presumably via binding to antioxidant-response element (ARE), which induce transcription of detoxifying enzymes such as AKR1C1 and AKR1C3 especially under hypoxia (Wanichwatanadecha et al. 2012). Notably, fluorescence remained predominantly cytoplasmic (Fig. 18.2(A)). In contrast, HPV16-E6 expression led to only a modest NRF2 increase under hyperoxic conditions, whereas vector controls consistently exhibited low NRF2 levels. At physiological normoxia, NRF2 expression

remained uniformly low across all models, indicating that basal redox homeostasis is largely independent of viral oncogene expression. These protein-level observations are consistent with the NRF2 mRNA data described above and are corroborated by western blotting, which revealed negligible NRF2 levels at 20% O_2 across all lines, a selective induction in HPV16-E6*I at 5% O_2, and a reversion to baseline at 2% O_2 (Figure 18.1(A)–(B)).

At the protein level, AKR1C3 - a direct NRF2 target and key NADPH-dependent oxidoreductase - mirrored the mRNA expression pattern. Under hypoxia, HPV16-E6*I overexpression resulted in a nearly 6-fold increase in AKR1C3 fluorescence intensity trend (Fig. 18.3(B)). As with NRF2, staining was restricted to the cytoplasm. The most pronounced AKR1C3 increase in HPV16-E6-overexpressing cells was observed under hyperoxia, while normoxic conditions resulted in only minor changes consistent with transcript data. In contrast, western blot analysis revealed that the AKR1C3 protein was most abundant in HPV16-E6*I cells at hyperoxia, decreasing at normoxia and hypoxia across backgrounds, as confirmed by densitometry (Figure 18.1(A)-(B)). The parallel changes in NRF2 localisation and AKR1C3 abundance point to a coordinated antioxidant programme orchestrated by HPV16-E6*I.

HPV16-E6*I modulates the O_2-dependent redox programme at transcriptional and post-transcriptional levels. NRF2 transcripts increase at normoxia and hypoxia, while protein levels peak at normoxia and decline at hypoxia, consistent with hypoxia-depth control via translational regulation and KEAP1-mediated turnover (Pakos-Zebrucka et al. 2016; Baird and Yamamoto 2020). AKR1C3, an NRF2-responsive gene (Penning 2017), shows hypoxia-enhanced cytoplasmic localisation despite reduced total protein, suggesting regulation by localisation, responder fraction, and activity rather than abundance alone. Elevated AKR1C3 at hyperoxia likely reflects hyperoxia-induced OS, whereas maximal NRF2 induction occurs at normoxia, and severe hypoxia limits protein accumulation despite high transcripts. These patterns support an optimal O_2-response window rather than a monotonic hypoxia effect, consistent with cycling hypoxia in tumours (Michiels et al. 2016). Pharmacological inhibition of AKR1C enzymes abolished the HPV16-E6*I-associated migratory

phenotype, identifying AKR1C3 as a pivotal NRF2 effector and linking O_2 tension to its abundance, localisation, and functional output.

7.3.3 Functional redox read-outs

HPV16-E6*I has been shown to enhance mitochondrial OS in an O_2-independent manner. To determine whether the transcriptional and enzymatic alterations described above lead to measurable changes in mitochondrial redox status, superoxide production was quantified using the MitoSOX™ Red assay. MitoSOX dyes are cationic, mitochondria-targeted hydroethidine (HE) derivatives that become fluorescent upon oxidation by superoxide in the mitochondrial matrix, providing a sensitive read-out of intramitochondrial ROS production. Under normoxic conditions, low levels of ETC-derived ROS function as signalling molecules. However, excessive O_2^- can overwhelm antioxidant defences, resulting in protein oxidation, DNA damage and genomic instability (Checa and Aran 2020; Robinson et al. 2006).

Fluorescence intensities obtained from MitoSOX™ Red staining were normalised to cell number using Hoechst nuclear counterstaining, ensuring comparability across experimental conditions. Confocal microscopy further confirmed the mitochondrial localisation of the MitoSOX signal, thereby validating the specificity of the assay for mitochondrial superoxide detection (Fig. 19(A) - (D)). Quantitative analysis revealed that HPV16-E6*I-overexpressing cells exhibited a consistent and significant elevation in mitochondrial ROS levels across all O_2 tensions when compared to both HPV16-E6-overexpressing cells and controls ($p < 0.01$ for all comparisons). Notably, while the most pronounced increase occurred under hypoxic conditions, elevated ROS levels persisted under normoxic and hyperoxic settings. These findings suggest that HPV16-E6*I drives mitochondrial redox imbalance independently of environmental O_2 concentration, likely as a consequence of altered mitochondrial metabolism or impaired ETC efficiency.

This phenotype aligns with the previously observed upregulation of NRF2 and its downstream effector AKR1C3 in HPV16-E6*I-overexpressing models (sections 6.11–6.12), suggesting a compensatory activation of antioxidant pathways in

response to persistent oxidative pressure. In contrast, the lack of comparable mitochondrial ROS accumulation in HPV16-E6-overexpressing cells - despite moderate NRF2 activation under hyperoxia - underscores a splice variant-specific mechanism of mitochondrial stress induction. The data support a model in which HPV16-E6*I establishes a heightened basal oxidative state, necessitating sustained NRF2–AKR1C3 axis engagement, and potentially contributing to the oncogenic redox rewiring observed in HPV^+ OPSCC. Methodologically, we recognise that MitoSOX can be influenced by non-superoxide oxidants; however, the concordant trends across O_2 levels and the alignment with NRF2/AKR1C3 read-outs mitigate this concern and argue for a biologically meaningful signal.

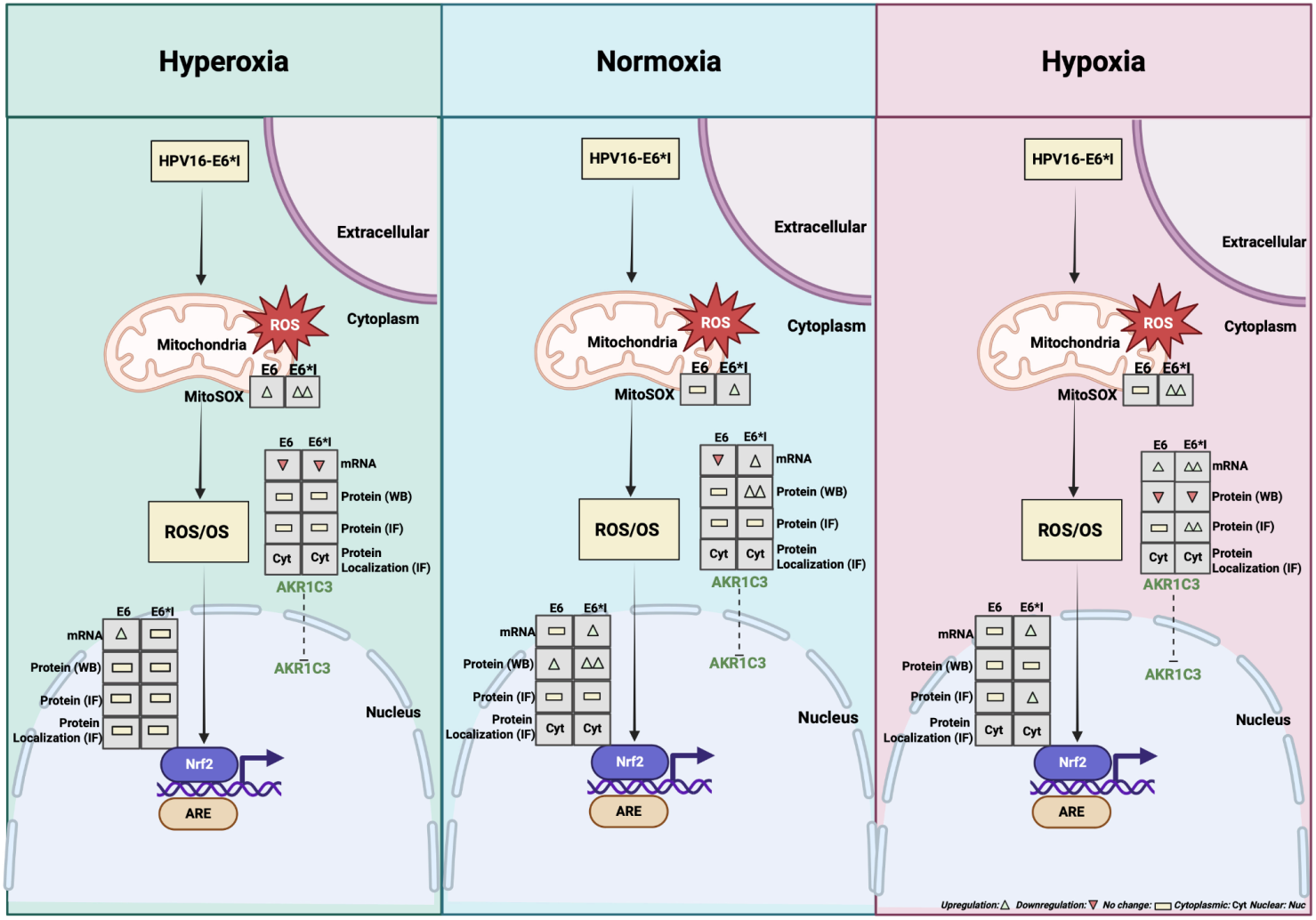

Figure legend in next page

Figure 24.The modulation of oxidative stress pathways by HPV16-E6 and -E6*I in relation to varying O_2 levels. The panels indicate the conditions of hyperoxia, normoxia and hypoxia. It is possible that mitochondria are one of the primary generators of ROS. Connectors with arrows indicate the direction from the source to the target. The dashed T-bar indicates direct, indirect or hypothesised relationships. Indicators of change are represented by call-outs (for example, ▲ for increase, ▼ for decrease, — for no change) for mRNA, WB, and IF. ddPCR discerned three unique patterns: In conditions of normoxia and hypoxia, HPV16-E6*I elevates NRF2, while in conditions of hyperoxia, HPV16-E6 does so. In conditions where there is a lack of O_2, HPV16-E6*I increases AKR1C3, but in conditions where there is an adequate supply of O_2, HPV16-E6 decreases AKR1C3, and both isoforms reduce AKR1C3 in conditions where there is an excess of O_2. Protein data and transcripts are identical. HPV16-E6*I generates around fourfold the NRF2 and sixfold the AKR1C3 levels in hypoxic conditions (predominantly cytoplasmic (cyt)), but HPV16-E6 induces just a slight elevation in NRF2 levels in hyperoxic conditions. MitoSOX™ tests indicate that HPV16-E6*I elevates mitochondrial superoxide across all oxygen tensions, with peak levels detected under hypoxic conditions. This finding supports the hypothesis of ongoing Nrf2–AKR1C interaction in HPV16-E6*I-overexpressing cells. Created in https://BioRender.com.

7.4 Regulation of Metabolic Pathways by HPV16-E6/E6*I Dependent on O_2 Concentration

*7.4.1 Investigating HPV16-E6*I-induced bioenergetic reprogramming: synergistic activation of OXPHOS and aerobic glycolysis in HEK 293 cells*

To assess whether HPV16-E6*I expression alters cellular energy metabolism, we employed the Seahorse XF Cell Mito Stress Test, a widely used platform for real-time quantification of mitochondrial respiration and glycolytic activity in living cells. The resulting data indicate that HPV16-E6*I substantially modifies the cellular bioenergetic profile. Under hyperoxic conditions, overexpression of HPV16-E6*I exhibited a markedly elevated OCR compared to HPV16-E6-overexpressing and vector control models. Specifically, significant increases were observed in basal respiration, ATP-linked respiration, and maximal respiration. In contrast, maximal respiratory capacity and proton leak remained unaffected, suggesting that OXPHOS is enhanced in a component-specific manner. This increase is unlikely to result from changes in mitochondrial content or membrane integrity. The pronounced elevation in basal respiration and ATP production under hyperoxia strongly supports the notion that HPV16-E6*I augments mitochondrial ETC activity without affecting reserve capacity. These findings are in agreement with previous studies showing that

HPV$^+$ HNSCC displays enhanced OXPHOS activity, including elevated COX expression and OCR compared to HPV$^-$ tumours (Huebbers et al. 2015; Jung et al. 2017). Although full-length HPV16-E6 has been reported to induce mitochondrial biogenesis via activation of the PGC-1α/ERRα transcriptional axis (Sannigrahi et al., n.d.; Huebbers et al. 2015), the current data suggest that HPV16-E6*I can also increase basal respiration, potentially via post-translational modulation of ETC components - an assumption that was subsequently examined at the mRNA, protein, and functional levels.

In parallel, HPV16-E6*I-overexpressing cell culture models also demonstrate a significant rise in ECAR, indicating that HPV16-E6*I promotes aerobic glycolysis. As ECAR primarily reflects proton extrusion due to lactate production, this observation implies increased glycolytic flux. These findings are consistent with previous reports that HPV16-E6 upregulates glycolytic flux, GLUT1 expression, and ECAR (Tang et al. 2020; Ma et al. 2019). The current data extend these observations to the HPV16-E6*I splice variant, which appears to support metabolic reprogramming by modulating ROS metabolism and stimulating glycolytic and the pentose-phosphate pathway activity (Wanichwatanadecha et al. 2012; Muñoz-Bello et al. 2018).

Clinically, HPV$^+$ HNSCC often exhibit high ^{18}F-FDG uptake and a glycolytic phenotype. This means they absorb large quantities of the radiolabelled glucose analogue 18F-FDG, which is visualised using PET-CT imaging to indicate increased glucose metabolism in tumours (Huebbers et al. 2015). The pronounced ECAR observed in HPV16-E6*I-overexpressing models suggests that this splice variant may contribute to that metabolic bias. By facilitating rapid ATP generation and biosynthetic precursor production, HPV16-E6*I may also promote a therapy resistance, including reduced sensitivity to radio- and chemotherapy (Kunkel et al. 2007; Li et al. 2012). Mechanistically, HPV16-E6*I retains the ability to cooperate with c-Myc and HIF-1α in upregulating glycolytic enzymes such as GLUT1, HK2, and LDHA despite lacking the PDZ-binding motif of full-length HPV16-E6 (Guo et al. 2014; Zhang et al. 2016). Additionally, NRF2 activation supports the expression of NADPH-producing enzymes,

while overexpression of AKR1C3 consumes NADPH. This dynamic NADPH cycling enables redox buffering and supports both glycolytic activity and anabolic growth by facilitating lactate production from excess pyruvate. HPV16-E6*I-high tumours depend on both elevated glycolysis (via LDHA, PDK1, and lactate export) and AKR1C3-mediated detoxification; hence, possible co-inhibiting both pathways may reveal synthetic-lethal vulnerabilities. (Balaji et al. 2021; Wanichwatanadecha et al. 2012).

Taken together, the Seahorse analysis served as an exploratory screen that identified aerobic glycolysis and OXPHOS as key metabolic pathways responsive to HPV16-E6*I expression. However, with the system available, it was not possible to analyze these responses under hypoxic conditions. Nevertheless, these results informed subsequent analyses of pathway components at the transcript, protein, and functional levels to further delineate their regulatory roles in HPV-driven metabolic reprogramming.

*7.4.2 Transcriptional metabolic flexibility: HPV-E6*I enhances glycolytic and OXPHOS gene expression at the mRNA level in hypoxic conditions*

To investigate whether HPV16-E6*I-induced bioenergetic changes are reflected at the transcriptional level under hypoxia, we analysed the expression of key glycolytic and mitochondrial genes using ddPCR. Results revealed significant increases in mRNA copy numbers of HK-2, COX1, and ATP5F1B for HPV16-E6*I-overexpressing cells under hypoxia, while corresponding decreases were observed in HPV16-E6 overexpressing cells (Fig. 21.2). In contrast, PKM2 and LDHA expression showed minimal variation across all O_2 concentrations. Absolute ddPCR copy counts confirmed the authenticity of these results, ruling out artefacts related to relative quantification.

The transcript pattern aligns with the Seahorse data (Fig. 20 (A) - (C)), in which increased basal, ATP-linked and maximum respiration were observed exclusively in HPV16-E6*I-overexpressing cells under hyperoxic conditions. Functionally, HK-2 localises to the outer mitochondrial membrane and catalyses the first step of glycolysis, trapping glucose and channelling it into both the glycolytic and pentose phosphate pathways. Its selective upregulation in HPV16-E6*I models suggests a preferential modulation of the initial phase of glycolysis, rather than the terminal steps catalysed by PKM2 and LDHA.

Concurrently, the increased expression of COX1 and ATP5F1B under hypoxia implies that HPV16-E6*I enhances or maintains mitochondrial electron transport capacity even under low O_2 conditions. It may even amplify this capacity, creating a “spare” pool of OXPHOS that can be tapped whenever transient O_2 becomes available. This may establish a “reserve” OXPHOS potential that can be mobilised during intermittent O_2 availability - a phenomenon described in tumour models undergoing cycling hypoxia (Huebbers et al. 2019). Such adaptive flexibility supports both ATP generation and redox balance when O_2 fluctuations occur in the tumour microenvironment.

Taken together, the ddPCR results suggest that HPV16-E6*I confers transcriptional metabolic flexibility by simultaneously upregulating glycolytic and OXPHOS genes under hypoxia. In contrast, HPV16-E6 appears to suppress both pathways under the same conditions. These findings are consistent with previous studies showing that HPV^+ HNSCC maintain elevated HK-2 and COX expression under hypoxia, whereas HPV16-E6 fosters a predominantly glycolytic or quiescent phenotype (Wanichwatanadecha et al. 2012; Jung et al. 2017). This form of metabolic dualism - characterised by the ability to engage both fermentative and oxidative metabolism - has been associated with treatment resistance in head-and-neck cancer models (Cruz-Gregorio et al. 2019; Mims et al. 2015), underscoring the clinical significance of the findings.

7.4.3 O_2-Dependent Regulation of Glycolytic and Mitochondrial Protein Expression in cell culture models

Western blot analysis revealed significant O_2 dependence in the expression of glycolytic and mitochondrial proteins in the evaluated cell culture models. Under hyperoxia, cells overexpressing HPV16-E6*I exhibited notably higher levels of HK-2, PKM2 and β-F1-ATPase proteins compared to cells from other models. However, LDHA expression remained consistent across all O_2 levels. When O_2 levels changed to normoxia or hyperoxia, the levels of HK-2, PKM2 and β-F1-ATPase proteins dropped markedly in all models. Conversely, LDHA protein levels rose slightly in some control cell culture models under hypoxia. Combining the data with ddPCR transcriptomic data reveals a more complex regulatory pattern. Although the amount of HK-2 protein decreased in both normoxia and hypoxia, cells overexpressing HPV16-E6*I exhibited a substantial increase in HK-2 mRNA copy number under hypoxic conditions. This suggests the presence of post-transcriptional or translational control mechanisms potentially involving mRNA stability, microRNA regulation, or hypoxia-dependent translational repression separating transcript abundance from protein abundance in low O_2 conditions. Such regulatory discordance is well known in cancer models with low O_2 levels, where selective translation inhibition alters the proteome to prioritise stress adaptation (Spriggs et al. 2010; Koritzinsky et al. 2006). Conversely, PKM2 and LDHA exhibited negligible variations in mRNA copy number across O_2 concentrations, corresponding with the relatively stable LDHA protein profile, but contrasting with the diminished PKM2 protein expression observed under normoxia and hypoxia. This further highlights the importance of oxygen-dependent translational control in regulating enzyme availability, especially for PKM2. This enzyme is known to be affected by post-translational modifications and protein-protein interactions, which can alter its stability and function without causing significant changes in mRNA levels (Dayton et al. 2016; Israelsen and Vander Heiden 2015).

Regarding mitochondrial markers, β-F1-ATPase protein levels were comparable to those of glycolytic enzymes, being highest in HPV16-E6*I-overexpressing cells under hyperoxia and dropping significantly under normoxia and hypoxia. Nevertheless, ddPCR analysis revealed increased levels of ATP5F1B and COX1 mRNA in HPV16-E6*I-overexpressing cells under hypoxic conditions, suggesting a potential anticipatory transcriptional upregulation of OXPHOS machinery. Although cyclic hypoxia was not tested directly in this study, the combined results obtained under hyperoxic, normoxic and hypoxic conditions may reflect transcriptional and metabolic flexibility, which mirrors tumour behaviour under cycling hypoxia. This condition is characterised by repeated fluctuations between low and reoxygenated states, which lead to transient reactivation of mitochondrial metabolism and adaptive survival mechanisms. This could create an "emergency" OXPHOS capacity that can be quickly utilised when O_2 levels are low, as has been observed in tumour models of cycling hypoxia (Höckel and Vaupel 2001; Michiels et al. 2016). Selective upregulation of HK-2 at the transcript level, alongside elevated COX1 and ATP5F1B levels in HPV16-E6*I-overexpressing cells, suggests metabolic dualism, which is the capacity to sustain or even enhance both glycolytic and mitochondrial pathways during hypoxia. This has been associated with metabolic plasticity in HPV^+ cancers (Jung et al. 2017; Wanichwatanadecha et al. 2012), allowing adaptation to fluctuating O_2 levels and facilitating tumour survival and growth. The observation that HPV16-E6-overexpressing cells inhibit both glycolytic and OXPHOS genes in hypoxic conditions is consistent with previous findings suggesting that HPV16-E6 promotes a predominantly glycolytic or quiescent phenotype (Cruz-Gregorio et al. 2019). This could potentially limit their ability to adapt within the hypoxic tumour microenvironment.

The ability to maintain dual metabolic pathways in hypoxic conditions has been linked to radioresistance and tolerance to chemotherapy in HNSCC (Mims et al. 2015), highlighting the importance of these findings in clinical practice. This study suggests that HPV16-E6*I-mediated metabolic flexibility, which is facilitated by the transcriptional activation of both glycolytic and OXPHOS genes yet regulated by

O_2-sensitive translational mechanisms, may provide a survival advantage in environments with variable O_2 levels. This could potentially influence treatment resistance.

*7.4.4 Functional-level metabolic profiling uncovers O_2-dependent functions of HPV16-E6 and E6*I*

To extend our transcript- and protein-level findings to cellular function, we next performed metabolic assays under defined O_2 conditions to characterise the bioenergetic behaviour of HPV16-E6 and HPV16-E6*I-overexpressing cells. Across both normoxic and hypoxic conditions, all cell culture models exhibited increased glucose uptake; however, the uptake pattern was genotype-specific. Under normoxia, cell overexpressing HPV16-E6 showed significantly higher glucose uptake than other models, whereas under hypoxia, the highest uptake was observed in HPV16-E6*I-overexpressing cells (Figure. 23(A)). This shift in substrate preference as O_2 availability declined suggests that HPV16-E6 and HPV16-E6*I differentially regulate glucose metabolism depending on environmental O_2 levels. These findings are consistent with earlier work demonstrating that HPV16-E6 enhances glucose import through GLUT transporters via activation of PI3K–AKT signalling and p53 inactivation (Wanichwatanadecha et al. 2012).

In contrast, lactate release increased approximately tenfold under hypoxia in all models, with no genotype-specific differences (Figure. 23(B)). This indicates that the terminal phase of glycolysis is predominantly driven by O_2 availability , as rather than directly regulated by either HPV16-E6 or HPV16-E6*I isoforms.

The ATP data offer further resolution. Under hyperoxic conditions, HPV16-E6*I-overexpressing cells produced the highest levels of ATP, consistent with their elevated OXPHOS activity. However, this energetic advantage was progressively lost under normoxia and hypoxia across all models (Figure. 23(C)). Together with the increased expression of COX1 and ATP5F1B transcripts in

HPV16-E6*I cells, these findings support the hypothesis that the splice variant maintains a “reserve” OXPHOS capacity that becomes functionally beneficial only when O_2 is plentiful (Vyas et al. 2016). By contrast, HPV16-E6-overexpressing cells demonstrate enhanced glucose uptake under normoxia without a corresponding increase in ATP, suggesting a shift towards aerobic glycolysis or the diversion of glucose into anabolic pathways. This phenotype has been described at both transcript and protein levels in HPV^+ keratinocytes (Cruz-Gregorio et al. 2019).

Under sustained hypoxia, HPV16-E6*I-overexpressing cells appear to implement a dual-fuel metabolic strategy. At the transcript level, it is evident that HK-2, COX1, and ATP5F1B mRNAs exhibit a significant increase, although PKM2 and LDHA levels remain unchanged. These transcript-level findings were corroborated by increased protein expression and enzymatic activity, including elevated HK2 and COX1 activity as confirmed by western blotting and complex-specific activity assays. Seahorse assays demonstrated corresponding increases in basal, ATP-linked, and maximal respiration, alongside enhanced performance in wound-healing and survival assays. Collectively, these results indicate that HPV16-E6*I-overexpressing cells can leverage transient O_2 availability via a preserved OXPHOS reserve, while simultaneously maintaining glycolytic flux through HK2-driven glucose entry and NADPH regeneration via the pentose phosphate pathway.

In contrast, HPV16-E6 overexpressing cells downregulate key OXPHOS genes and rely predominantly on glycolysis. These cells can survive under normoxia but fail to adapt under conditions of severe O_2 or glucose limitation. The combined data provide mechanistic insight into why HPV16-E6*I confers superior metabolic flexibility compared to HPV16-E6. This flexibility likely contributes to the survival advantage observed in specific tumour subpopulations and presents a greater therapeutic challenge. Importantly, the findings also suggest that the metabolic dependencies of HPV16-E6*I-overexpressing cells could be exploited to develop targeted combination therapies that induce synthetic lethality.

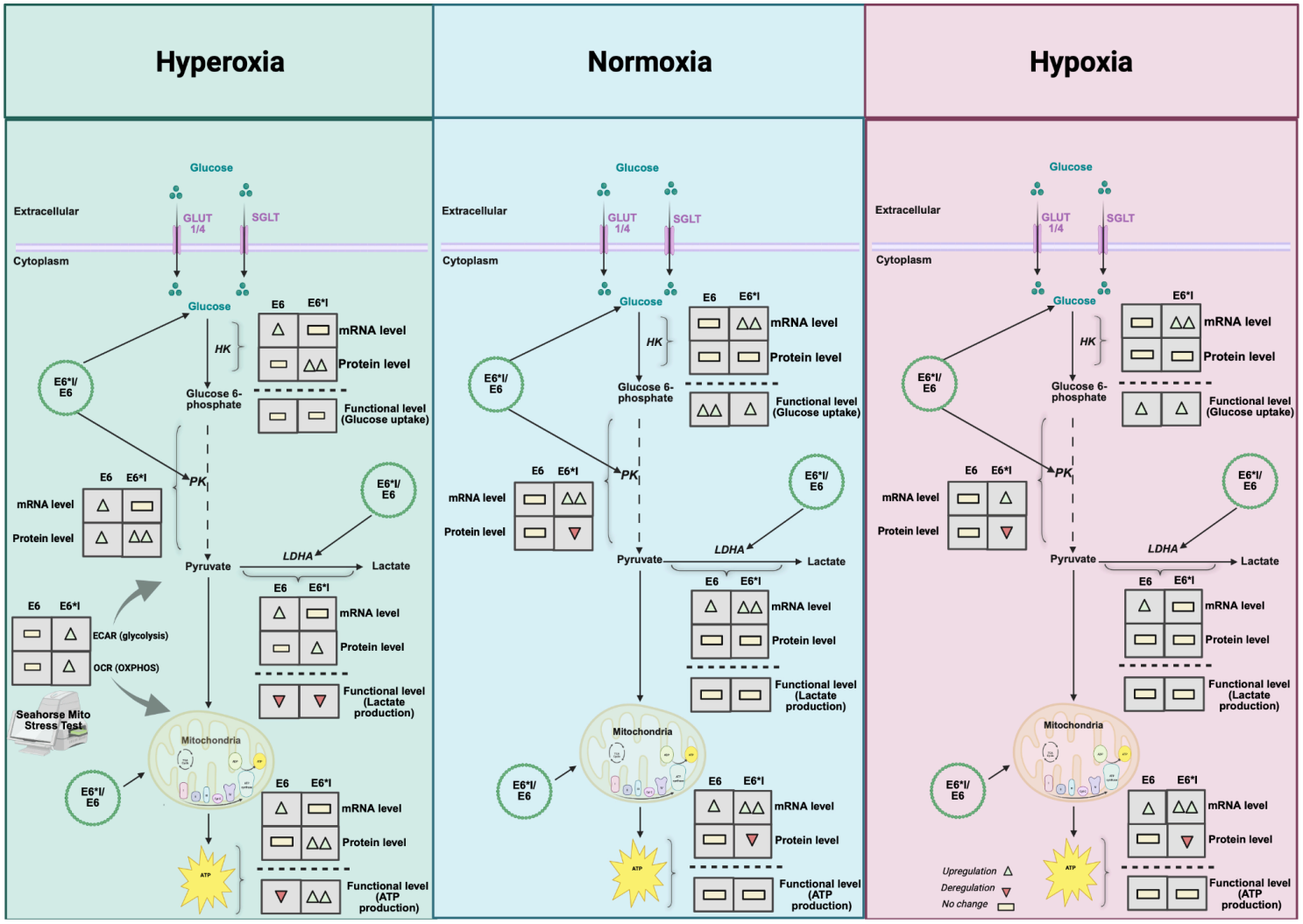

Figure legend in next page

Figure 25. **HPV16-E6 and HPV16-E6*I alter glycolytic and mitochondrial pathways in an O_2-dependent manner.** Panels show metabolism changes in HEK 293 models in the presence of hyperoxic (20%), normoxic (5%) or hypoxic (2%) O_2 levels. Seahorse XF analysis indicates that HPV16-E6*I enhances basal and ATP-linked mitochondrial respiration (OCR) and glycolytic activity (ECAR) in hyperoxic conditions without affecting maximal respiration or proton leak. Changes in function, transcript (mRNA) and protein (Western blot) levels are indicated by the symbols ▲ (increase), ▼ (decrease) and — (no change).

ddPCR shows that HPV16-E6*I increases HK-2, COX1 and ATP5F1B transcripts at hypoxia, while HPV16-E6 decreases them. Western blots reveal elevated HK-2, PKM2 and β-F1-ATPase protein levels in HPV16-E6*I cells under hyperoxia, while their expression diminishes under hypoxia in all models. LDHA levels remain constant across O_2 conditions. Subsequently functional metabolic assays are included. Glucose uptake assays demonstrate that HPV16-E6 increases glucose uptake more at normoxia than at hypoxia, whereas HPV16-E6*I peaks at hypoxia$_2$. Under normoxia and hypoxic conditions, all models demonstrate an approximate constant increase in lactate production, regardless of genotype compared to hyperoxia. Under hyperoxia, ATP levels are highest in HPV16-E6*I cells, supporting higher OXPHOS capacity. However, this benefit is lost under hypoxia. The data suggest that HPV16-E6*I promotes metabolic duality by supporting both glycolytic and oxidative pathways simultaneously, whereas HPV16-E6 exhibits a preference for glycolysis and has reduced adaptability to low O_2 conditions. Created in https://BioRender.com.

7.5 RNA-FISH validates HPV16-E6/-E6*I detection in FFPE cells and sets the stage for integration-linked ROS and metabolic mapping

To spatially link HPV integration sites identified by FFPE-TLA with transcript-level phenotypes, we employed LNA RNA-FISH as a tool to detect HPV16-E6 and HPV16-E6*I expression in FFPE tumour tissue, with the dual aim of identifying HPV16-E6*I-overexpressing tumours for mechanistic insight and potential diagnostic or therapeutic targeting.

Initial validation in paraffin-embedded UD-SCC-2 cells confirmed the high specificity of the HPV16-E6 and HPV16-E6*I probe sets, with minimal background and clean separation of Cy5 and DsRed signals. The observed signal ratio of approximately 1:1 matched the RT-qPCR data, thereby validating the performance of the probes, the accuracy of the splicing ratio, and the overall quality of the assay.

The successful implementation of this method supports its application to FFPE patient specimens, where integration hotspots have been mapped using FFPE-TLA. Previous studies, as well as our own cell culture findings, suggest that viral integration is frequently associated with elevated HPV16-E6*I expression in HPV^+ OPSCC (Zhang et al. 2016; Huebbers et al. 2015).

Notably, tumours with high HPV16-E6*I expression display enhanced proliferation, migratory potential, and altered ROS and metabolic profiles (Wanichwatanadecha et al. 2012; Huebbers et al. 2019; Cruz-Gregorio et al. 2019; Qin et al. 2020). These phenotypes mirror those observed in our HPV16-E6*I-overexpressing cell models, suggesting that HPV16-E6*I may act as a key effector of integration-driven metabolic reprogramming and redox adaptation.

Importantly, the same oxidative stress induced by HPV16-E6*I may further promote viral genome integration through DNA damage (Huebbers et al. 2019), creating a feed-forward loop between splicing, ROS, and genomic instability. By applying validated HPV16-E6*I LNA RNA-FISH probes to FFPE samples with known TLA-defined integration status, we can now begin to spatially correlate tumours with elevated HPV16-E6*I expression and correlate them with biomarkers of ROS metabolism (e.g., NRF2, AKR1C3), glycolysis (e.g., HK2, GLUT1) and OXPHOS (e.g., COX1, ATP5F1B) identified in vitro.

This integrative spatial approach offers a unique opportunity to dissect how HPV integration, transcript splicing, and metabolic phenotype intersect within the tumour microenvironment. By defining HPV16-E6*I-high metabolic niches, we may uncover biomarkers for aggressive tumour behaviour and identify candidates for therapeutic intervention. Such findings could refine molecular diagnostics and enable the development of combination therapies targeting metabolic and redox vulnerabilities specific to HPV16-E6*I-driven tumours

8 Conclusion

HPV$^+$ OPSCC is a clinically unique category of head and neck malignancies. Although most HPV$^+$ OPSCC patients exhibit a favourable response to therapy, a few will encounter relapses or metastases. This underscores the significance of employing molecularly informed risk stratification. The aim of this thesis was to examine the functional consequences of HPV16 genome integration and conducted a comprehensive analysis of HPV16-E6*I splice variant expression under differing O_2 conditions, focussing on cellular motility, redox regulation, and metabolic adaptability. This builds on previous research from our group, which identified that HPV16 integration into human genome and HPV16-E6*I overexpression is associated with unfavourable disease outcome.

A significant methodological enhancement was the introduction of FFPE-TLC, facilitating high-resolution identification of virus-host genome fusions in preserved FFPE OPSCC specimens. This demonstrated integration in approximately 56% of cases and revealed that viral integration patterns were consistent across matched metastatic lesions. These data confirm FFPE-TLC as a clinically relevant instrument for stratifying HPV$^+$ OPSCC according to structural viral-host interactions.

Stable overexpression of HPV16-E6*I in HEK 293 cells resulted in a unique, O_2 - sensitive migratory phenotype, facilitating expedited wound closure in hypoxic and hyperoxic environments, yet not in physiological normoxia. This was in contrast to the minor effects observed in HPV16-E6-overexpressing or control cells. Extensive analysis has identified that both NRF2 and AKR1C3 are elevated at the mRNA and protein levels in a O_2-dependant manner in HPV16-E6*I-overexpressing cells. Immunofluorescence revealed prominent cytoplasmic accumulation of NRF2 and AKR1C3 in HPV16-E6*I-overexpressing cells, particularly under hypoxic conditions. Notably, pharmacological inhibition of AKR1C1/3 abrogated the HPV16-E6*I-induced migratory phenotype, implicating these enzymes as functional mediators of redox-driven motility and metabolic adaptation.

Metabolic analyses demonstrated that HPV16-E6*I overexpresses glycolytic (HK-2) and mitochondrial (COX1, ATP5F1B) genes under hypoxia, supporting a dual-fuel

phenotype. Despite the attenuation of HK-2 and β-F1-ATPase at the protein level at hypoxia, HPV16-E6*I-overexpressing cells demonstrated sustained elevated mitochondrial respiration, ATP production, and glucose uptake, indicating functional metabolic flexibility. In contrast, HPV16-E6-overexpressing cells suppressed both pathways under hypoxia, favouring a less adaptive profile. The observed discrepancy between transcript and protein levels indicates the presence of O_2-sensitive translational regulation. These findings position HPV16-E6*I as a key modulator of bioenergetic adaptation, with the potential to sustain both oxidative and glycolytic metabolism in fluctuating O_2 environments, possibly enabling survival during cycling hypoxia, as observed in aggressive tumour microenvironments. This adaptive capacity may represent a clinically relevant metabolic vulnerability in HPV-driven cancers.

We have developed and validated isoform-specific RNA-FISH probes targeting HPV16-E6 and HPV16-E6*I. These probes facilitate transcript-specific spatial profiling in FFPE samples. This development enables the concurrent detection of integration status and isoform expression. When used with FFPE-TLC, this method allows for the effective grouping of patients in a clinical setting.

To summarise, this thesis identifies HPV16-E6*I as a central regulator of O_2-sensitive cell motility, redox signalling, and metabolic reprogramming, with mechanistic links to NRF2-AKR1C pathways. In combination with high-resolution integration mapping, these findings support a model in which viral integration, HPV16-E6*I expression, and downstream redox-metabolic adaptations converge to define distinct molecular subtypes within HPV^+ OPSCC, extending previous work from our group that associated HPV16-E6*I overexpression and viral host genome integration with unfavourable disease outcome. These features have translational potential for disease stratification and offer promising targets for personalized therapeutic strategies in HPV-driven malignancies.

9 Appendix

Figure S1-S3 and Table S2-S10 is based on Demers, Balaji et al., 2024

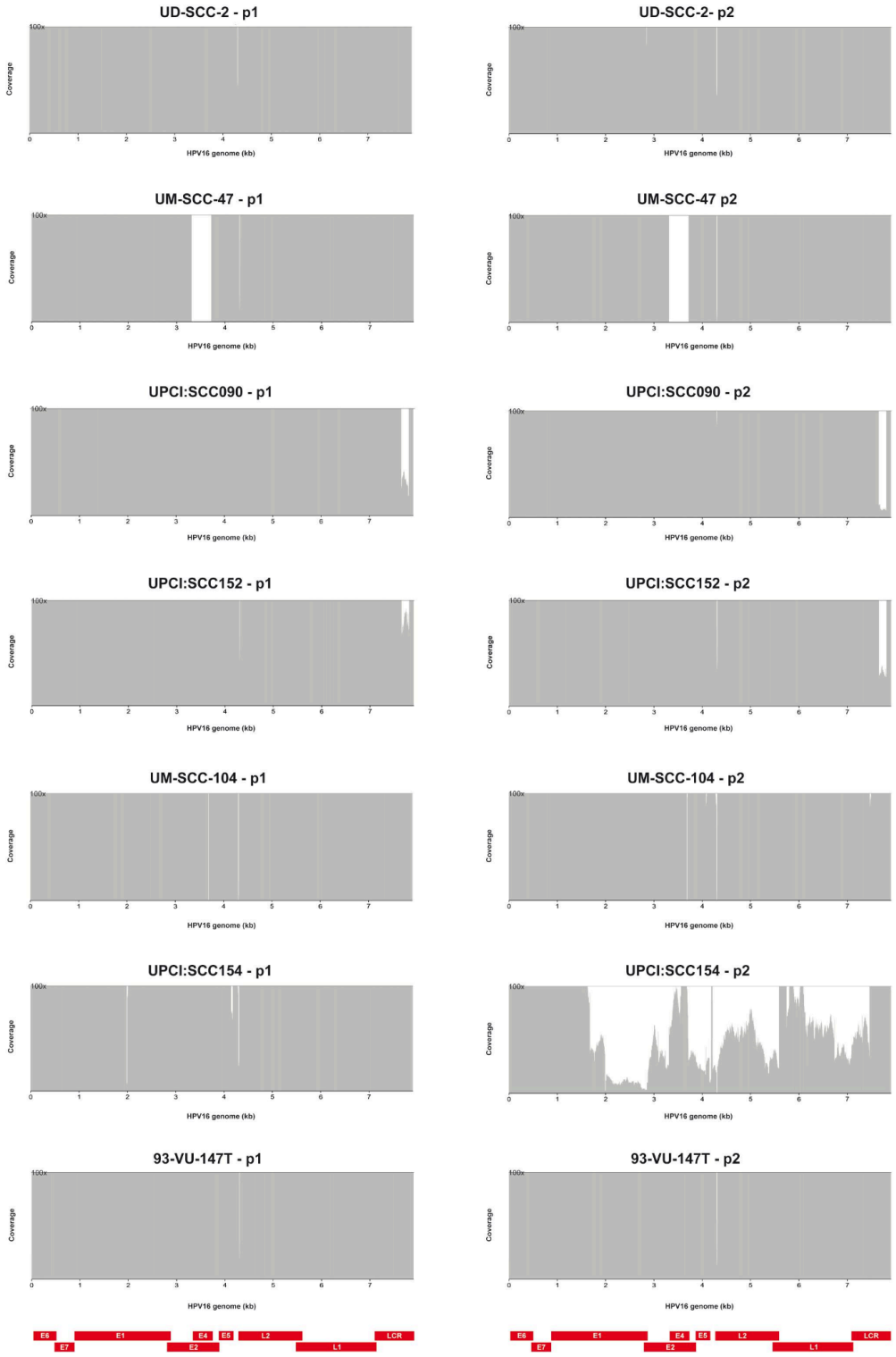

Figure S1. The HPV16 genome has been detected in HPV⁺ HNSCC cell lines and xenografts.The read coverage throughout the HPV16 genome has been displayed for certain HPV⁺ HNSCC cell lines.

Each panel displays a reproduction of a specific HPV⁺ HNSCC cell line, either panel 1 or panel 2. The x-axis represents the HPV16 genome (0–8 kb), while the y-axis indicates the read depth (up to 100×). The bottom panel illustrates the annotated structure of the HPV16 genome. It displays the early genes (E6, E7, E1, E2, E4, and E5) and the late genes (L2 and L1), as well as the long control region (LCR). The observed differences in coverage patterns indicate that the samples possess varying integration statuses and structural alterations in the HPV16 genome.

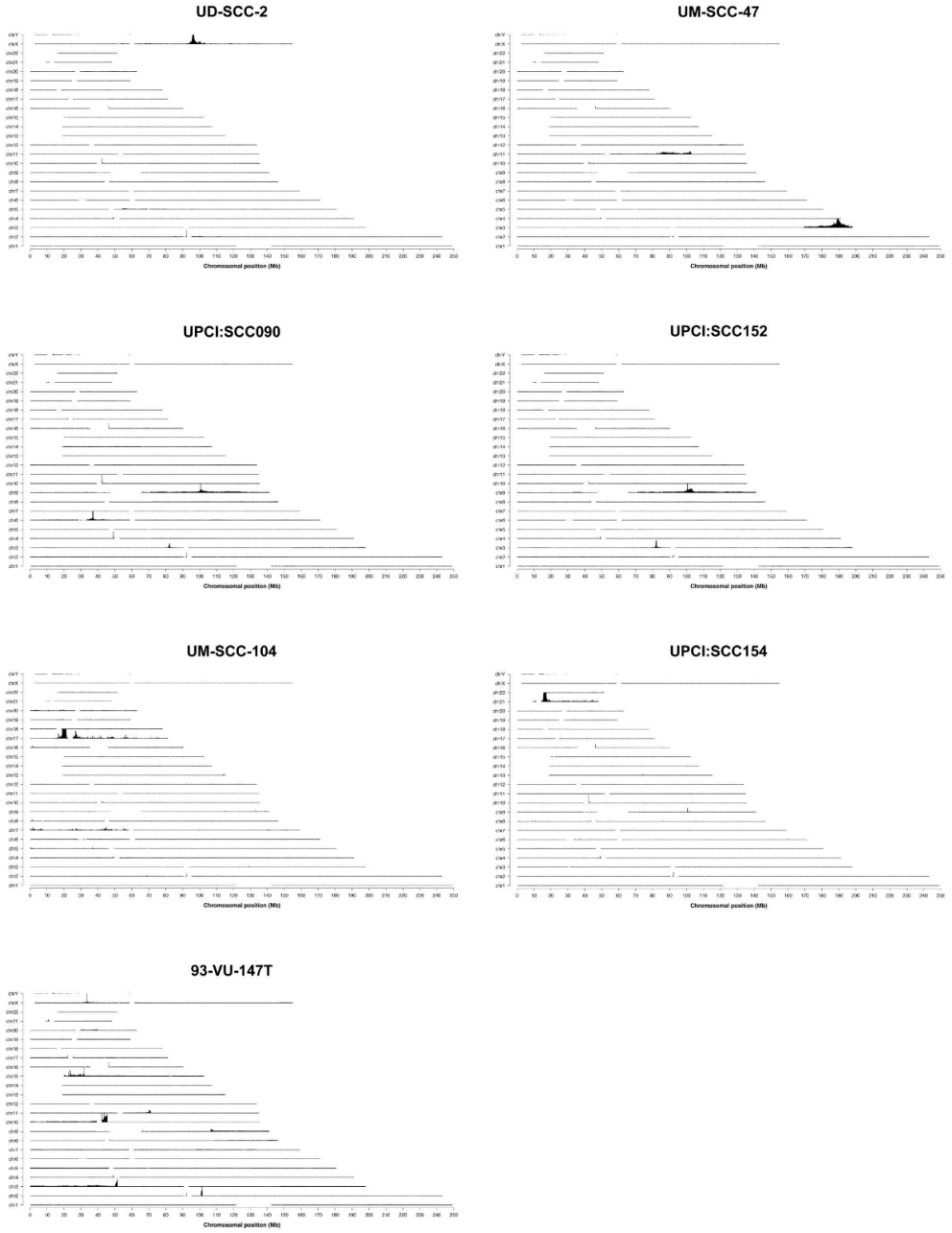

Figure S2. TLA sequencing of HPV⁺ HNSCC cell lines demonstrates the location of HPV16 integration into the genome. Each panel in the HPV⁺ HNSCC cell lines illustrates the distribution of

HPV16 integration events across the human genome, based on TLA. The x-axis displays the location of chromosomes on the basis of their bps, while the y-axis illustrates the human chromosome (chr1–22, X, Y). Each dot on the graph represents a chimeric read that links HPV16 to a specific location in the human genome. The presence of vertical clusters of dots that align along a chromosome indicates the existence of localised integration hotspots. These maps facilitate precise identification of HPV16 integration locations across the genome in HPV+ HNSCC cell lines.

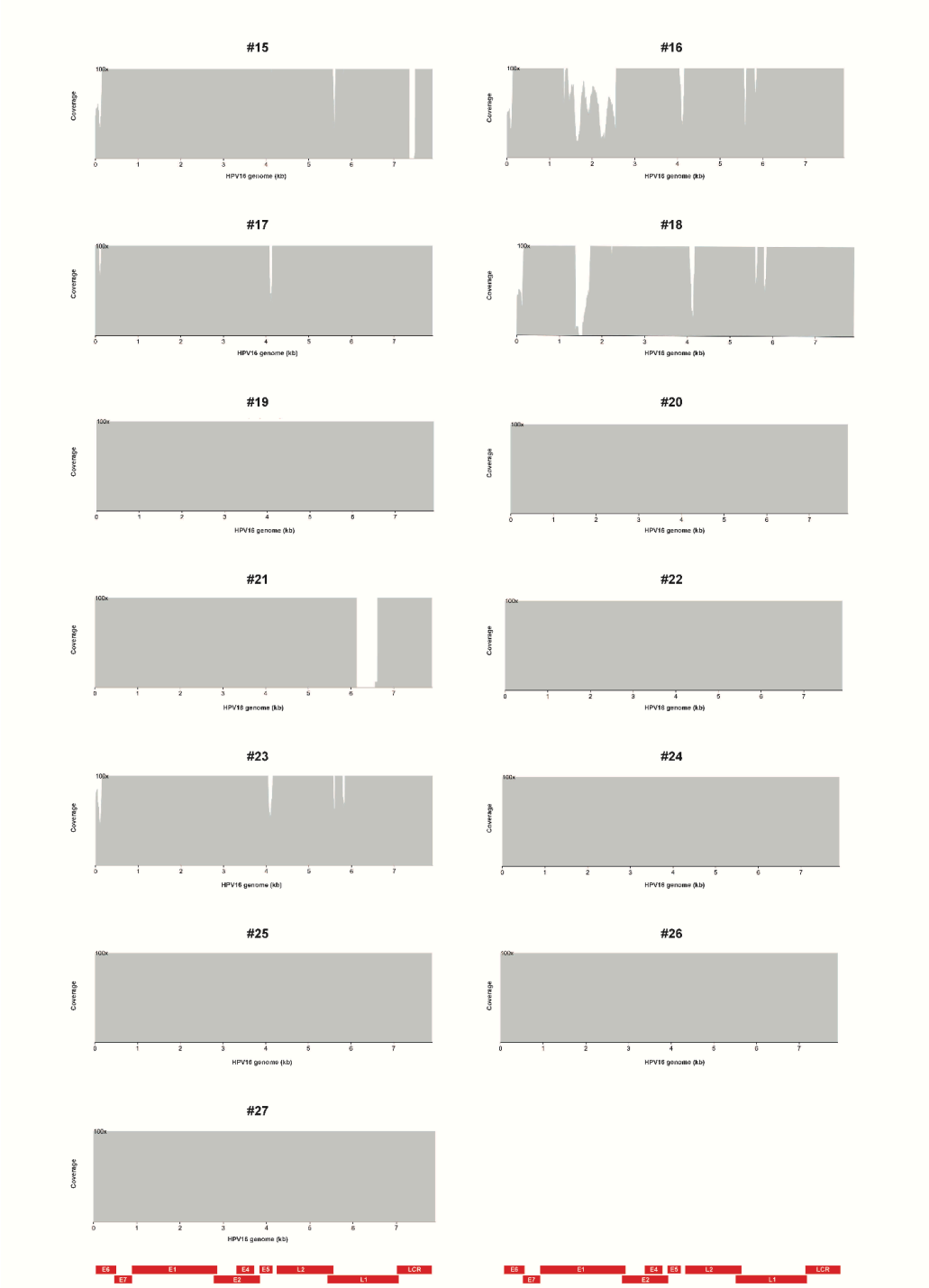
#15
#16
#17
#18
#19
#20
#21
#22
#23
#24
#25
#26
#27
Coverage
HPV16 genome (kb)
E6
E7
E1
E2
E4
E5
L2
L1
LCR

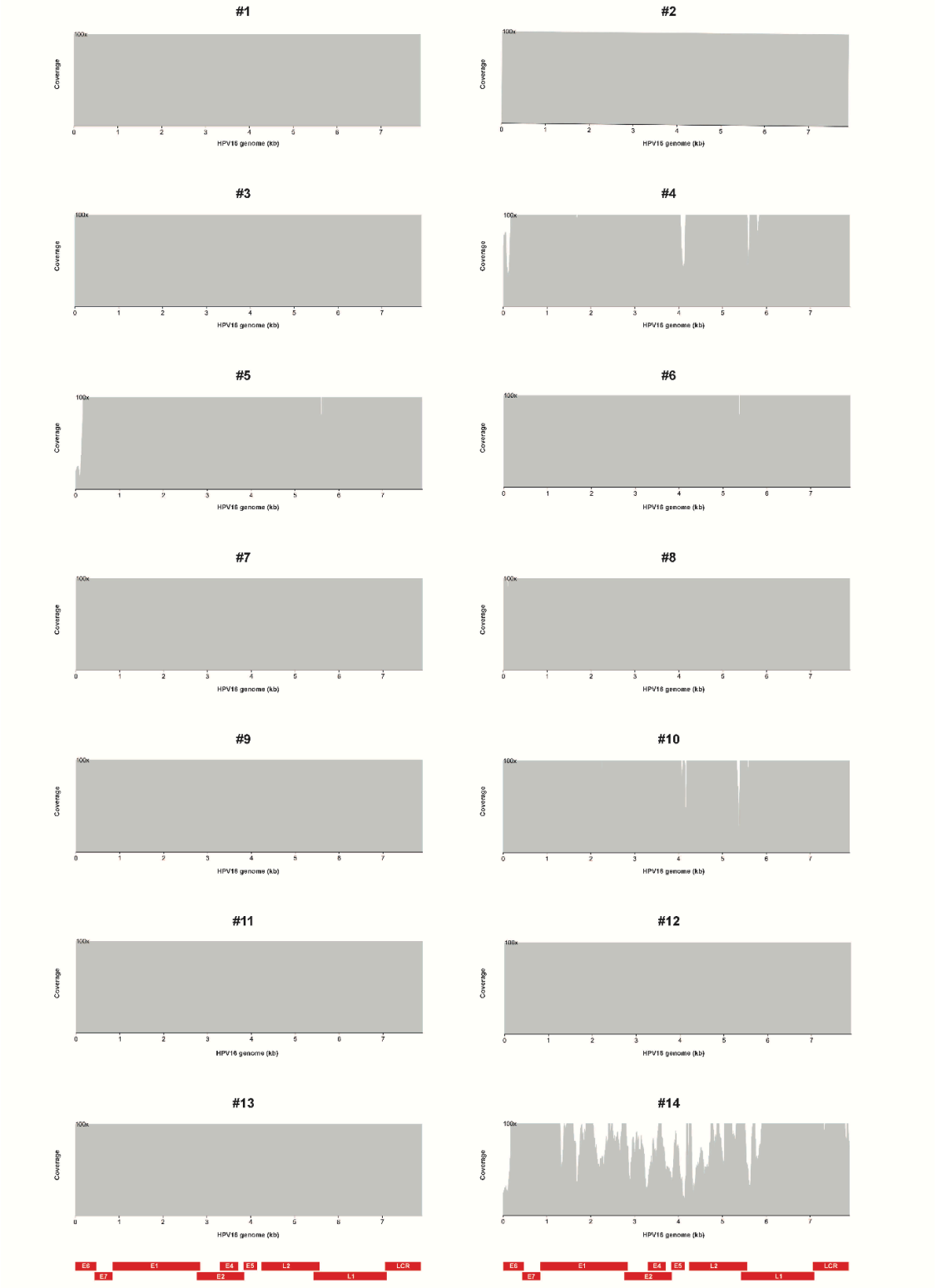

Figure S3: Coverage plots of the HPV16 genome obtained through FFPE-TLC sequencing from 27 FFPE HPV⁺ OPSCC patient samples. Each panel (numbered 1 to 27) shows the read coverage

across the HPV16 genome. The y-axis shows the depth of sequencing reads (coverage). Grey shading shows the number of aligned reads at different genomic positions. Red gene maps at the bottom of each plot show the HPV16 genes (E6, E7, E1, E2, E4, E5, L2 and L1) and the LCR. Differences in integration status, physical structure (episomal versus integrated) and sequencing depth cause variation in coverage across the genome and between samples. Samples exhibiting sudden declines or localised peaks in coverage (e.g. samples #4, #10, #14, #16, #18 and #23) may indicate potential viral integration events. Samples with flat or low coverage probably contain no HPV16 DNA.

Table S1. Clinicopathological and Molecular Characteristics of HPV⁺ HNSCC and CSCC Cell Lines (Bradford et al. 2003; Tang et al. 2020; Wald et al. 2011; Göttgens et al. 2021; Pattillo et al. 1977; Jackson et al. 2013)

	Cell line	HPV Status	Primary Site	Sex	Age	Alcohol/ Smoking	TNM	Viral Load	TP53	PIK3A	Tp63	Keap1
HNSCC cell lines	UM-SCC-47	HPV16⁺	Tongue	Male	53	-/Yes	T4N2bM0	15	Wild type	Gain	Gain	Wild type
	UPCI:SCC090	HPV16⁺	Base of Tongue	Male	46	Yes/Yes	T2N0	739	Wild type	Gain	Gain	Gain
	UM-SCC-104	HPV16⁺	Floor of mouth	Male	56	Yes/Yes	T4N2bM0	1	Wild type Missense mutation	WT	-	-
	93-VU-147T	HPV16⁺	Floor of mouth	Male	58	Yes/Yes	T4N2	n.a.	Missense mutation	Not detected	Gain	Not reported
	UPCI:SCC152	HPV16⁺	Hypopharynx	Male	47	Yes/Yes	Recurrence of SCC090	210	Shallow deleted	Gain	Gain	Gain
	UPCI:SCC154	HPV16⁺	Tongue	Male	54	Yes/Yes	T4N2	1	Wild type	Gain	Gain	Wild type
CSCC cell lines	CaSki	HPV16⁺	Cervix uteri	Female	45	-/-	IIIB or higher	≈600	Wild type (inactivated by HPV16-E6)	-	-	-

	Cell line	HPV Status	Primary Site	Sex	Age	Alcohol/ Smoking	TNM	Viral Load	TP53	PIK3A	Tp63	Keap1
	SiHa	$HPV16^{+}$	Cervix uteri	Female	55	-/-	IB	1–2	Wild type (inactivated by HPV16-E6)	-	-	-

Table S2. Primes used in TLA analysis for HPV16 integration detection.

Primer set	Name	Direction	Binding position	Sequence
1	VP16 E7	RV	620	TGCTCATAACAGTAGAGATCAG
		FW	843	TTCTCAGAAACCATAATCTACCA
2	VP16 E1	RV	898	CATCCATTACATCCCGTACC
		FW	1050	AGAAACAGAGACAGCACATG

RV = Reverse; FW = Forward

Table S3. Capture probes used in FFPE-TLC

Probe	Location	Size (kb)
HPV16	HPV16 sequence	7800
HPV18	HPV18 sequence	7735
RPL4	Chr15:66791653-66797193	5540
GAPDH	Chr12:6643585-6647537	3952
ACTB	Chr7:5566779-5570232	3453

Table S4: Information on HPV genome coverage in HPV$^+$ HNSCC cell lines.

Cell line	primer set	bases of HPV genome covered at least 30x	% of bases of HPV genome covered at least 30x	Median Coverage (reads)	Minimal Coverage (reads)	Maximal Coverage (reads)
UD-SCC-2	P1	7904	100	3157	46	536002
	P2	7904	100	745	37	999406
UM-SCC-47	P1	7488	94,74	2664	0	382486
	P2	7892	99,85	2182	7	999372
UPCI:SCC090	P1	7860	99,44	9292	18	422978
	P2	7747	98,01	3973	6	999265
UPCI:SCC152	P1	7904	100	4760	45	334927
	P2	7885	99,76	3157	27	999201
UM-SCC-104	P1	7878	99,67	861	0	269428
	P2	7879	99,68	541	0	804929
UPCI:SCC154	P1	7880	99,7	497	7	578279
	P2	6390	80,85	61	0	999997
93-VU-147T	P1	7895	99,89	4231	20	322916
	P2	7892	99,85	2804	13	999976

Table S5. Integration locations of HPV16 with specified breakpoints in the human and viral genomes in HPV$^+$ HNSCC cell lines.

Cell line	Chromosome	Break points	Hg19 location	Hg19 Gene	HPV16 location	HPV16 gene
UD-SCC-2	chrX	6	96,215,117 (tail)	DIAPH2	4,984 (head)	L2
			96,238,769 (tail)	DIAPH2	5,458 (head)	L2
			96,369,882 (head)	DIAPH2	3,101(tail)	E2
			96,373,470 (tail)	DIAPH2	3,245 (head)	E2

Cell line	Chromosome	Break points	Hg19 location	Hg19 Gene	HPV16 location	HPV16 gene
			96,375,641 (tail)	DIAPH2	7,888 (tail)	-
			96,380,876 (tail)	DIAPH2	7,709 (head)	-
UM-SCC-47	chr3	2	189,612,849 (tail)	TP63	3719 (head)	E2
			189,596,814 (head)	TP63	3312 (tail)	E2
UPCI:SCC090	chr3	2	82,041,282 (tail)	LINC02008	7590 (head)	-
			82,275,717 (head)	LINC02008	1,072 (tail)	E1
	chr6	5	36,878,572 (head)	C6orf89	4,974 (head)	L2
			36,904,459 (tail)	-	6,411 (head)	L1
			37,129,029 (head)	-	4,948 (tail)	L2
			37,135,220 (head)	-	5,025 (tail)	L2
			37,164,550 (tail)	-	5,254 (head)	L2
	chr9	12	100,575,617 (head)	PTCSC2	681 (head)	E7
			100,596,047 (tail)	PTCSC2	1,308 (tail)	E1
			100,620,064 (tail)	-	823 (head)	E7
			100,653,547 (head)	-	662 (head)	E7
			100,665,228 (tail)	TRMO	4,708 (tail)	E5
			100,676,884 (tail)	TRMO	2,062 (tail)	E1
			100,699,563 (tail)	HEMGN	1078 (tail)	E1
			100,702,506 (head)	HEMGN	5,969 (head)	L1
			100,704,893 (head)	HEMGN	7,434 (head)	-
			100,707,990 (tail)	-	284 (head)	E6
			100,714,372 (tail)	-	1,824 (tail)	E1
UPCI:SCC152	chr3	4	81,834,934 (head)	-	6,660 (tail)	L1
			82,041,282 (tail)	LINC02008	7819 (head)	-
			82,016,561 (head)	-	n.d.	
			82,275,717 (head)	LINC02008	1,072 (tail)	E1
	chr9	10	100,575,617 (head)	PTCSC2	681 (head)	E7
			100,596,047 (tail)	PTCSC2	1,308 (tail)	E1
			100,620,064 (tail)	-	823 (head)	E7
			100,665,228 (tail)	TRMO	4,708 (tail)	E5

Cell line	Chromosome	Break points	Hg19 location	Hg19 Gene	HPV16 location	HPV16 gene
			100,676,884 (tail)	TRMO	2,062 (tail)	E1
			100,699,563 (tail)	HEMGN	1078 (tail)	E1
			100,702,506 (head)	HEMGN	5,969 (head)	L1
			100,704,893 (head)	HEMGN	7,434 (head)	-
			100,714,372 (tail)	-	1,824 (tail)	E1
			100,581,164	PTCSC 2	n.d.	
UM-SCC-104	chr17	2	19,609,637 (tail)	SLC47A 2	3682 (tail)	E2
			19,609,646 (head)	SLC47A 2	2697 (head)	E1
UPCI:SCC 154	chr21	2	16,645,539 (tail)	-	1,988 (head)	E1
			16,688,012 (head)	-	2,002 (head)	E1
93-VU-147 T	chr2	1	101,595,323 (tail)	NPAS2	1,072(tail)/ 7,552 (tail)	E1/not annotated
	chr3	4	51,537,011 (tail)	-	3,684 (tail)	E2
			51,537,453 (head)	-	4507 (head)	L2
			51,567,601 (tail)	-	6,067 (tail)	L1
			51,577,389 (tail)	RAD54L 2	2,623 (head)	E1
	chr15	2	31,627,224 (tail)	KLF13	4155 (tail)	-
			31,627,391 (head)	KLF13	1628 (head)	E1
	chr17		36423208 (head)	-	1067 (tail)	E1
	chrX	2	33,479,828 (tail)	-	3810 (head)	E2
			33,479,836 (head)	-	138 (tail)	E6

Table S6: Coverage data of HPV genomes in OPSCC FFPE samples.

Sample #	Bases of HPV genome covered at least 30x	% of bases of HPV genome covered at least 30x	Median coverage (reads)	Minimal coverage (reads)	Maximal coverage (reads)
1	7904	100	12695	632	28494
2	7904	100	8333	452	25682
3	7904	100	756	98	2243
4	7901	99,96	280	29	1125
5	7778	98,41	455	12	1827
6	7904	100	3414	78	6457
7	7904	100	4558	444	7885
8	7904	100	1346	83	3551

Sample #	Bases of HPV genome covered at least 30x	% of bases of HPV genome covered at least 30x	Median coverage (reads)	Minimal coverage (reads)	Maximal coverage (reads)
9	7904	100	1686	182	3337
10	7882	99,72	839	29	1891
11	7904	100	12781	347	52422
12	7662	96,94	101	16	1699
13	7747	98,01	409	0	1922
14	7657	96,88	276	14	1755
15	7904	100	779	86	1520
16	7904	100	649	33	8345
17	7616	96,36	306	0	2067
18	7904	100	20143	1830	41889
19	7904	100	5794	531	14502
20	7904	100	784	116	1527
21	7409	93,74	24931	0	108634
22	7904	100	425	40	1784
23	7904	100	5460	682	9329
24	7904	100	27361	4611	44457
25	7904	100	12952	1348	42551
26	7904	100	3637	178	7415
27	7904	100	29095	2610	63612

Table S7: HPV integration sites with identified breakpoints in the human and viral genome in FFPE tissues.

Sample	Chromosome	Number of breakpoints	hg19 location	Orientation*	hg19 gene	HPV16 location	Orientation*	HPV gene
11	chr6	1	68972636	-	LINC02549	3446	-	E2/E4
	chr9	1	2656785	-	VLDLR	3505	+	E2/E4
12	chr2	2	103384870	-	TMEM182	5068	+	L2
			103388162	-	TMEM182	5047	+	L2
	chr2	2	157183335	+	NR4A2	5523	-	L2
			157189965	-	NR4A2	1297	-	E1
13	chr3	2	112054091	-	CD200	6664	+	L1
			112054367	+	CD200	7497	+	LCR
14	chr2	2	60706308	-	BCL11A	3040	-	E2
			60706950	+	BCL11A	3295	+	E2
	chr5	2	82630844	+	XRCC4	1244	-	E1
			82651923	-	XRCC4	2558	+	E1
16	chr3	3	189098274	-	-	513	-	E6
			189099974	+	-	6507	+	L1
			189119362	-	-	2638	-	E1
17	chr2	2	28508226	-	BABAM2	2381	-	E1
			28509536	+	BABAM2	2256	+	
18	chr17	2	39678936	-	-	1542	+	E1
			39678951	+	-	2872	-	
19	chr2	2	184957986	-	-	6922	+	L1
			184960413	+	-	2493	-	E1

Sample	Chromosome	Number of breakpoints	hg19 location	Orientation*	hg19 gene	HPV16 location	Orientation*	HPV gene
	chr22	5	32282767	+	DEPDC5	2757	-	E1
			32293202	-	DEPDC5	2270	+	E1
			32296749	-	DEPDC5	1603	+	E1
			32297245	+	DEPDC5	3080	-	E2
			32314096	-	-	1265	-	E1
20	chr1	1	73676109	-	-	3842	+	E2
	chr6	1	17025479	+	-	2992	-	E2
	chr17	10	1959459	-	HIC1	1603	+	E1
			1967689	+	SMG6	468	-	E6
			1982073	-	SMG6	371	+	E6
			2004317	-	SMG6	4878	+	L2
			2005470	+	SMG6	5735	-	L1
			2007649	-	SMG6	2329	+	E1
			2023167	-	SMG6	5351	+	L2
			2024510	-	SMG6	4320	+	L2
			2029046	+	SMG6	676	-	E7
			2039828	+	SMG6	940	-	E1
	chrY	2	28701528	+	-	956	-	E1
			28759700	-	PARP4P1	2523	-	E1
21	chr1	1	33347001	-	-	3984	+	E5
	chr1	2	186344999	-	ODR4	6535	+	L1
			186345023	+	ODR4	4408	-	L2

Sample	Chromosome	Number of breakpoints	hg19 location	Orientation*	hg19 gene	HPV16 location	Orientation*	HPV gene
	chr2	2	131845245	+	FAM168B	3993	-	E5
			131848446	-	FAM168B	3564	+	E2/E4
	chr4	2	99496204	+	TSPAN5	1478	+	E1
			99505137	-	TSPAN5	3493	-	E2/E4
	chr8	2	64847798	-	LINC01414	3068	-	E2
			64867588	-	LINC01414	5828	+	L1
	chr16	2	15803291	+	NDE1	4729	+	L2
			15814528	-	NDE1	3939	-	E5
22	chr3	2	142711904	-	PAQR9-AS1	3734	-	Downstream E4
			142712550	+	PAQR9-AS1	4749	+	L2
	chr8	2	48967602	-	UBE2V2	4564	+	L2
			48967605	+	UBE2V2	2815	-	E2
23	chr2	6	77393687	-	LRRTM4	4292	-	L2
			77395155	-	LRRTM4	5082	-	L2
			77410284	-	LRRTM4	2396	-	E1
			77410302	+	LRRTM4	2481	+	E1
			77418915	-	LRRTM4	2598	-	E1
			77428493	+	LRRTM4	4215	+	Downstream E5
	chr14	3	103313007	+	TRAF3	2465	-	E1

Sample	Chromosome	Number of breakpoints	hg19 location	Orientation*	hg19 gene	HPV16 location	Orientation*	HPV gene
			103342642	-	TRAF3	2409	+	E1
			103407800	+	CDC42BPB	1529	-	E1
	chrY	2	16063155	+	-	7368	-	LCR
			16063671	+	-	2191	+	E1
25	chr1	2	174888849	+	RABGAP1L	5692	+	L1
			174904833	-	RABGAP1L	5506	-	L2
	chr13	1	59602224	+	-	502	-	E6
	chr17	2	49518193	+	LINC02073	5802	+	L1
			49518820	-	LINC02073	7620	-	LCR
26	chr1	2	84677551	-	PRKACB	7436	+	LCR
			84677569	+	PRKACB	2658	-	E1
	chr14	1	22695532	-	TRA	2715	-	E1
	chr20	2	30615204	+	CCM2L	3792	+	E2
			30650598	-	HCK	2746	-	E1
27	chr2	1	27008947	-	CENPA	3163	+	E2
	chr2	2	85249393	-	KCMF1	2521	+	E1
			85249467	+	KCMF1	6296	-	L1
	chr2	7	218686281	+	TNS1	5156	-	L2
			218692971	+	TNS1	4848	+	L2

Sample	Chromosome	Number of breakpoints	hg19 location	Orientation*	hg19 gene	HPV16 location	Orientation*	HPV gene
			218693753	-	TNS1	3978	+	E5
			218713292	+	TNS1	4623	+	L2
			218713556	+	TNS1	3795	-	Downstream E4
			218748339	+	TNS1	7356	-	LCR
			218832423	+	TNS1	7103	+	L1
	chr2	3	26970306	-	-	4152	+	Downstream E5
			26970716	+	-	1237	-	E1
			26977462	-	-	7736	+	LCR
	chr2	3	56990551	+	-	3470	+	E2
			57025925	-	-	3152	-	E2
			57026200	+	-	3161	+	E2
	chr3	2	30710587	+	TGFBR2	6724	-	L1
			30710754	-	TGFBR2	6901	+	L1
	chr3	4	51187185	-	DOCK3	6793	+	L1
			51187612	-	DOCK3	4799	+	L2
			51192717	-	DOCK3	189	+	E6
			51284786	+	DOCK3	3059	-	E2
	chr4	7	42572056	+	ATP8A1	5426	+	L2

Sample	Chromosome	Number of breakpoints	hg19 location	Orientation*	hg19 gene	HPV16 location	Orientation*	HPV gene
			42587996	-	ATP8A1	481	+	E6
			42588125	+	ATP8A1	434	-	E6
			42591473	-	ATP8A1	4577	+	L2
			42594288	-	ATP8A1	725	+	E7
			42603298	-	ATP8A1	675	+	E7
			42617277	-	ATP8A1	2405	-	E1
	chr4	4	133238868	+	-	1132	-	E1
			133240415	+	-	652	+	E7
			133242328	-	-	7297	+	LCR
			133263740	+	-	2752	+	E1
	chr5	1	13241703	-	-	2697	-	E1
	chr5	4	23803278	+	-	4096	+	E5
			23805326	+	-	3307	-	E2
			24260958	+	-	7688	-	LCR
			25567153	-	-	5240	-	L2
	chr7	5	67348113	+	-	7454	+	LCR
			67370712	-	-	5036	-	L2
			67370939	+	-	5049	+	L2
			67376270	-	-	4889	-	L2

Sample	Chromosome	Number of breakpoints	hg19 location	Orientation*	hg19 gene	HPV16 location	Orientation*	HPV gene
			67378361	-	-	4599	-	L2
	chr8	2	116618540	+	TRPS1	3920	-	E5
			116631838	+	TRPS1	5882	-	L1
	chr9	5	92056481	+	SEMA4D	3430	-	E2
			92076601	-	SEMA4D	3759	+	E2
			92076788	+	SEMA4D	601	-	E7
			92078554	-	SEMA4D	3382	-	E2/E4
			92079996	-	SEMA4D	7627	+	LCR
	chr9	3	134100237	-	NUP214	572	+	E7
			134103563	-	NUP214	3458	+	E2/E4
			134105982	+	NUP214	562	-	E7
	chr12	2	130548282	-	-	7523	+	LCR
			130548612	+	-	287	-	E6
	chr13	2	115037444	+	CDC16	3971	+	E5
			115085449	-	CHAMP1	5643	+	L2
	chr14	1	68405219	-	RAD51B	6170	+	L1
	chr15	2	85996166	+	AKAP13	5550	+	L2
			85997651	-	AKAP13	6925	-	L1
	chr18	2	3285903	+	-	2148	+	E1

Sample	Chromosome	Number of breakpoints	hg19 location	Orientation*	hg19 gene	HPV16 location	Orientation*	HPV gene
			3286195	-	-	3692	-	Downstream E4
	chr22	1	47876095	-	LINC01644	726	-	E7

* Orientation: + = sense strand, - = anti-sense strand

Table S8: Validation of HPV breakpoints in cell lines and FFPE tumour specimens via PCR and Sanger sequencing.

Cell lines			
Cell line	**Int. site**	**Breakpoints confirmed by PCR**	**Breakpoints confirmed by seq**
UPCI:SCC090	Chr3	2/2	Not determined
	Chr6	3/5	Not determined
	Chr9	3/12	Not determined
UPCI:SCC154	Chr21	2/2	Not determined
93-VU-147T	Chr3	1/4	Not determined
	ChrX	1/2	1/2
FFPE tumour samples			
Patient #	**Int. site**	**Breakpoints confirmed by PCR**	**Breakpoints confirmed by seq**
FFPE-TLC different from DIPS-PCR results			
14	Chr2	2/2	1/2
	Chr5	2/2	2/2
15	Chr13	0/1	-
22	Chr3	2/2	0
	Chr8	2/2	0
	Chr18	0/1	-
23	Chr6	0/1	-
FFPE-TLC results partly similar to DIPS-PCR results			
19	Chr2	1/2	0
	Chr22	3/5	1/3
FFPE-TLC results similar to DIPS results			
16	Chr3	3/3	3/3
18	Chr17	2/2	1/2

Table S9: HPV integration loci with characterised breakpoints in the human and viral genomes within FFPE tissues of tonsillar and metastatic neoplasms.

Sample	Location	Chromosome	Number of breakpoints	hg19 location	Orientation*	hg19 gene	HPV16 location	Orientation*	HPV gene
25	Tonsil	chr1	2	174888849	+	RABGAP1L	5692	+	L1
				174904833	-	RABGAP1L	5506	-	L2
		chr13	1	59602224	+	-	502	-	E6
		chr17	2	49518193	+	LINC02073	5802	+	L1
				49518820	-	LINC02073	7620	-	LCR
	Lung	chr1	1	3740891	+	-	2151	-	E1
		chr3	2	174624145	-	NAALADL2	6983	-	L1
				174854979	+	NAALADL2	7161	+	LCR
		chr13	1	59602224	+	-	502	-	E6
		chr17	8	65962502	-	BPTF	6701	-	L1
				65945009	+	BPTF	n.d.	n.d.	
				65946266	+	BPTF	878	+	E1
				65952754	-	BPTF	5564	-	L2
				65955810	+	BPTF	1597	+	E1
				65957741	-	BPTF	827	-	E7
				65959118	+	BPTF	4801	+	L2
				65961234	-	BPTF	2150	-	E1

Sample	Location	Chromosome	Number of breakpoints	hg19 location	Orientation*	hg19 gene	HPV16 location	Orientation*	HPV gene
		chr19	1	11631228	+	ECSIT	2151	-	E1
	Liver	chr1	1	3740891	+	-	2151	-	E1
		chr3	3	174624145	-	NAALADL2	6983	-	L1
				174854979	+	NAALADL2	7161	+	LCR
				174864097	-	NAALADL2	5238	-	L2
		chr13	1	59602224	+	-	502	-	E6
		chr17	7	65945009	+	BPTF	n.d.	n.d.	
				65946266	+	BPTF	878	+	E1
				65952754	-	BPTF	5564	-	L2
				65955810	+	BPTF	1597	+	E1
				65957741	-	BPTF	827	-	E7
				65959118	+	BPTF	4801	+	L2
				65961234	-	BPTF	2150	-	E1
		chr19	1	11631228	+	ECSIT	2151	-	E1
26	Tonsil	chr1	2	84677551	-	PRKACB	7436	+	LCR
				84677569	+	PRKACB	2658	-	E1
		chr14	1	22695532	-	TRA	2715	-	E1
		chr20	2	30615204	+	CCM2L	3792	+	E2
				30650598	-	HCK	2746	-	E1

Sample	Location	Chromosome	Number of breakpoints	hg19 location	Orientation*	hg19 gene	HPV16 location	Orientation*	HPV gene
	Lung	chr1	2	84677551	-	PRKACB	7436	+	LCR
				84677569	+	PRKACB	2658	-	E1
27	Tonsil	chr2	1	27008947	-	CENPA	3163	+	E2
		chr2	2	85249393	-	KCMF1	2521	+	E1
				85249467	+	KCMF1	6296	-	L1
		chr2	7	218692971	+	TNS1	5156	-	L2
				218693753	+	TNS1	4848	+	L2
				218713292	-	TNS1	3978	+	E5
				218748339	+	TNS1	4623	+	L2
				218713556	+	TNS1	3795	-	Downstream E4
				218832423	+	TNS1	7356	-	LCR
				218686281	+	TNS1	7103	+	L1
		chr2	3	26970306	-	-	4152	+	Downstream E5
				26970716	+	-	1237	-	E1
				26977462	-	-	7736	+	LCR
		chr2	3	56990551	+	-	3470	+	E2
				57025925	-	-	3152	-	E2
				57026200	+	-	3161	+	E2
		chr3	2	30710754	+	TGFBR2	6724	-	L1
				30710587	-	TGFBR2	6901	+	L1
		chr3	4	51284786	-	DOCK3	6793	+	L1
				51192717	-	DOCK3	4799	+	L2
				51187185	-	DOCK3	189	+	E6

Sample	Location	Chromosome	Number of breakpoints	hg19 location	Orientation*	hg19 gene	HPV16 location	Orientation*	HPV gene
				51187612	+	DOCK3	3059	-	E2
		chr4	7	42572056	+	ATP8A1	5426	+	L2
				42587996	-	ATP8A1	481	+	E6
				42588125	+	ATP8A1	434	-	E6
				42591473	-	ATP8A1	4577	+	L2
				42594288	-	ATP8A1	725	+	E7
				42603298	-	ATP8A1	675	+	E7
				42617277	-	ATP8A1	2405	-	E1
		chr4	4	133238868	+	-	1132	-	E1
				133240415	+	-	652	+	E7
				133242328	-	-	7297	+	LCR
				133263740	+	-	2752	+	E1
		chr5	1	13241703	-	-	2697	-	E1
		chr5	4	23803278	+	-	4096	+	E5
				23805326	+	-	3307	-	E2
				24260958	+	-	7688	-	LCR
				25567153	-	-	5240	-	L2
		chr7	5	67348113	+	-	7454	+	LCR
				67370712	-	-	5036	-	L2
				67370939	+	-	5049	+	L2
				67376270	-	-	4889	-	L2
				67378361	-	-	4599	-	L2
		chr8	2	116618540	+	TRPS1	3920	-	E5
				116631838	+	TRPS1	5882	-	L1

Sample	Location	Chromosome	Number of breakpoints	hg19 location	Orientation*	hg19 gene	HPV16 location	Orientation*	HPV gene
		chr9	5	92056481	+	SEMA4D	3430	-	E2
				92076601	-	SEMA4D	3759	+	E2
				92076788	+	SEMA4D	601	-	E7
				92079996	-	SEMA4D	3382	-	E2/E4
				92078554	-	SEMA4D	7627	+	LCR
		chr9	3	134100237	-	NUP214	572	+	E7
				134105982	-	NUP214	3458	+	E2/E4
				134103563	+	NUP214	562	-	E7
		chr12	2	130548282	-	-	7523	+	LCR
				130548612	+	-	287	-	E6
		chr13	2	115037444	+	CDC16	3971	+	E5
				115085449	-	CHAMP1	5643	+	L2
		chr14	1	68405219	-	RAD51B	6170	+	L1
		chr15	2	85996166	+	AKAP13	5550	+	L2
				85997651	-	AKAP13	6925	-	L1
		chr18	2	3286195	+	-	2148	+	E1
				3285903	-	-	3692	-	E2
		chr22	1	47876095	-	LINC01644	726	-	E7
	Bone	chr2	3	26970306	-	KCNK3	4152	+	Downstream E5
				26970716	+	KCNK3	1237	-	E1
				26977462	-	KCNK3	7736	+	LCR
		chr2	3	56990551	+	-	3470	+	E4
				57025925	-	-	3152	-	E2
				57026200	+	-	3161	+	E2

Sample	Location	Chromosome	Number of breakpoints	hg19 location	Orientation*	hg19 gene	HPV16 location	Orientation*	HPV gene
		chr2	4	26980969	-	-	6659	+	L1
				27005664	-	-	4935	-	L2
				26937318	-	-	6075	-	L1
				26949960	+	-	3908	+	E5
		chr2	1	27012521	-	-	6853	-	L1
		chr3	3	51187185	-	DOCK3	189	+	E6
				51187612	+	DOCK3	3059	-	E2
				51200788	-	DOCK3	4693	+	L2
		chr4	7	42572056	+	ATP8A1	5426	+	L2
				42587996	-	ATP8A1	481	+	E6
				42588125	+	ATP8A1	434	-	E6
				42591473	-	ATP8A1	4577	+	L2
				42594288	-	ATP8A1	725	+	E7
				42603298	-	ATP8A1	675	+	E7
				42617277	-	ATP8A1	2405	-	E1
		chr4	4	133238868	+	-	1132	-	E1
				133240415	+	-	652	+	E7
				133242328	-	-	7297	+	LCR
				133263740	+	-	2752	+	E1
		chr5	1	13241703	-	-	2697	-	E1
		chr5	4	23803278	+	-	4096	+	E5
				23805326	+	-	3307	-	E2
				24260958	+	-	7688	-	LCR
				25567153	-	-	5240	-	L2

Sample	Location	Chromosome	Number of breakpoints	hg19 location	Orientation*	hg19 gene	HPV16 location	Orientation*	HPV gene
		chr6	2	6940618	-	-	7495	+	LCR
				6906868	+	-	3901	-	E5
		chr6	2	126569786	+	-	2606	+	E1
				126569677	-	-	6092	-	L1
		chr6	2	6909251	-	-	2532	+	E1
				6933792	+	-	3042	-	E2
		chr6	2	126561844	+	-	5955	+	L1
				126552406	+	-	6377	+	L1
		chr7	3	67370712	-	-	5036	-	L2
				67370939	+	-	5049	+	L2
				67376270	-	-	4889	-	L2
		chr8	1	116631838	+	TRPS1	5882	-	L1
		chr9	3	92056481	+	SEMA4D	3430	-	E4
				92076601	-	SEMA4D	3759	+	E2
				92078554	-	SEMA4D	7627	+	LCR
		chr9	3	134100237	-	NUP214	572	+	E7
				134105982	-	NUP214	3458	+	E4
				134103563	+	NUP214	562	-	E7
		chr10	3	21605210	-	-	5035	-	L2
				21605228	+	-	3326	+	E2
				21588603	+	-	6991	-	L1
		chr12	2	130548282	-	-	7523	+	LCR
				130548612	+	-	287	-	E6
		chr13	1	115037444	+	CDC16	3971	+	E5

Sample	Location	Chromosome	Number of breakpoints	hg19 location	Orientation*	hg19 gene	HPV16 location	Orientation*	HPV gene
		chr14	1	68405219	-	RAD51B	6170	+	L1
		chr15	2	85996166	+	AKAP13	5550	+	L2
				85997651	-	AKAP13	6925	-	L1
		chr22	1	47876095	-	-	726	-	E7

Table S10: Detection of HPV16–HPV16 genomic fusion events and associated breakpoint sites in clonal tumour samples.

Sample	Tumour location	HPV16 location	Orientation*	HPV16 location	Orientation*
25	Tonsil	5733	-	5805	+
		2072	+	6551	-
		577	+	7431	-
		2329	-	3672	+
	Lung	577	+	7431	-
		2329	-	3672	+
	Liver	577	+	7431	-
		2329	-	3672	+
26	Tonsil	2707	+	4632	+
	Lung	-			
27	Tonsil	412	+	7220	-
		2719	-	3238	+
		7499	-	7523	+
	Bone	412	+	7220	-
		2719	-	3238	+
		7499	-	7523	+

* Orientation: + = sense strand, - = anti-sense strand

10 References

Adeniji, A. O., Twenter, B. M., Byrns, M. C., Jin, Y., Chen, M., Winkler, J. D., & Penning, T. M. (2012). Development of potent and selective inhibitors of aldo-keto reductase 1C3 (type 5 17β-hydroxysteroid dehydrogenase) based on N-phenyl-aminobenzoates and their structure-activity relationships. *Journal of Medicinal Chemistry*, *55*(5), 2311–2323.

Akagi, K., Li, J., Broutian, T. R., Padilla-Nash, H., Xiao, W., Jiang, B., Rocco, J. W., Teknos, T. N., Kumar, B., Wangsa, D., He, D., Ried, T., Symer, D. E., & Gillison, M. L. (2014). Genome-wide analysis of HPV integration in human cancers reveals recurrent, focal genomic instability. *Genome Research*, *24*(2), 185–199.

Allahyar, A., Pieterse, M., Swennenhuis, J., Los-de Vries, G. T., Yilmaz, M., Leguit, R., Meijers, R. W. J., van der Geize, R., Vermaat, J., Cleven, A., van Wezel, T., Diepstra, A., van Kempen, L. C., Hijmering, N. J., Stathi, P., Sharma, M., Melquiond, A. S. J., de Vree, P. J. P., Verstegen, M. J. A. M., … de Laat, W. (2021a). Robust detection of translocations in lymphoma FFPE samples using targeted locus capture-based sequencing. *Nature Communications*, *12*(1), 3361.

Arenz, A., Patze, J., Kornmann, E., Wilhelm, J., Ziemann, F., Wagner, S., Wittig, A., Schoetz, U., Engenhart-Cabillic, R., Dikomey, E., & Fritz, B. (2019). HPV-negative and HPV-positive HNSCC cell lines show similar numerical but different structural chromosomal aberrations. *Head & Neck*, *41*(11), 3869–3879.

Baird, L., & Yamamoto, M. (2020). The Molecular Mechanisms Regulating the KEAP1-NRF2 Pathway. *Molecular and Cellular Biology*, *40*(13), e00099-20.

Balaji, H., Demers, I., Wuerdemann, N., Schrijnder, J., Kremer, B., Klussmann, J. P., Huebbers, C. U., & Speel, E.-J. M. (2021). Causes and Consequences of HPV Integration in Head and Neck Squamous Cell Carcinomas: State of the Art. *Cancers*, *13*(16), 4089.

Barger, J. F., & Plas, D. R. (2010). Balancing biosynthesis and bioenergetics: Metabolic programs in oncogenesis. *Endocrine-Related Cancer*, *17*(4), R287–R304.

Bradford, C. R., Zhu, S., Ogawa, H., Ogawa, T., Ubell, M., Narayan, A., Johnson, G., Wolf, G. T., Fisher, S. G., & Carey, T. E. (2003). P53 mutation correlates with cisplatin sensitivity in head and neck squamous cell carcinoma lines. *Head & Neck*, *25*(8), 654–661.

Campbell, J. D., Yau, C., Bowlby, R., Liu, Y., Brennan, K., Fan, H., Taylor, A. M., Wang, C., Walter, V., Akbani, R., Byers, L. A., Creighton, C. J., Coarfa, C., Shih, J., Cherniack, A. D., Gevaert, O., Prunello, M., Shen, H., Anur, P., … Van Waes, C. (2018). Genomic, Pathway Network, and Immunologic

Features Distinguishing Squamous Carcinomas. *Cell Reports*, *23*(1), 194-212.e6.

Carreau, A., Hafny-Rahbi, B. E., Matejuk, A., Grillon, C., & Kieda, C. (2011). Why is the partial oxygen pressure of human tissues a crucial parameter? Small molecules and hypoxia. *Journal of Cellular and Molecular Medicine*, *15*(6), 1239–1253.

Checa, J., & Aran, J. M. (2020). Reactive Oxygen Species: Drivers of Physiological and Pathological Processes. *Journal of Inflammation Research*, *13*, 1057–1073.

Contreras-Paredes, A., De la Cruz-Hernández, E., Martínez-Ramírez, I., Dueñas-González, A., & Lizano, M. (2009). E6 variants of human papillomavirus 18 differentially modulate the protein kinase B/phosphatidylinositol 3-kinase (akt/PI3K) signaling pathway. *Virology*, *383*(1), 78–85.

Cruz-Gregorio, A., Aranda-Rivera, A. K., Aparicio-Trejo, O. E., Coronado-Martínez, I., Pedraza-Chaverri, J., & Lizano, M. (2019). E6 Oncoproteins from High-Risk Human Papillomavirus Induce Mitochondrial Metabolism in a Head and Neck Squamous Cell Carcinoma Model. *Biomolecules*, *9*(8), 351.

Cruz-Gregorio, A., Martínez-Ramírez, I., Pedraza-Chaverri, J., & Lizano, M. (2019). Reprogramming of Energy Metabolism in Response to Radiotherapy in Head and Neck Squamous Cell Carcinoma. *Cancers*, *11*(2), Article 2.

Dang, C. V., & Semenza, G. L. (1999). Oncogenic alterations of metabolism. *Trends in Biochemical Sciences*, *24*(2), 68–72.

Dayton, T. L., Gocheva, V., Miller, K. M., Israelsen, W. J., Bhutkar, A., Clish, C. B., Davidson, S. M., Luengo, A., Bronson, R. T., Jacks, T., & Vander Heiden, M. G. (2016). Germline loss of PKM2 promotes metabolic distress and hepatocellular carcinoma. *Genes & Development*, *30*(9), 1020–1033.

de Vree, P. J. P., de Wit, E., Yilmaz, M., van de Heijning, M., Klous, P., Verstegen, M. J. A. M., Wan, Y., Teunissen, H., Krijger, P. H. L., Geeven, G., Eijk, P. P., Sie, D., Ylstra, B., Hulsman, L. O. M., van Dooren, M. F., van Zutven, L. J. C. M., van den Ouweland, A., Verbeek, S., van Dijk, K. W., … de Laat, W. (2014). Targeted sequencing by proximity ligation for comprehensive variant detection and local haplotyping. *Nature Biotechnology*, *32*(10), 1019–1025.

Dekker, J., Rippe, K., Dekker, M., & Kleckner, N. (2002). Capturing Chromosome Conformation. *Science*, *295*(5558), 1306–1311.

Demers, I., Balaji, H., Feitsma, H., Stelloo, E., Swennenhuis, J., Sergeeva, I., Wuerdemann, N., van den Hout, M. F. C. M., Wagner, S., Kremer, B., Klussmann, J. P., Huebbers, C. U., & Speel, E.-J. M. (2024). Proximity ligation-based sequencing for the identification of human papillomavirus genomic integration sites in formalin-fixed paraffin embedded oropharyngeal squamous cell carcinomas. *Journal of Medical Virology*, *96*(8), e29837.

Dominguez, J. E., Graham, J. F., Cummins, C. J., Loreck, D. J., Galarraga, J., Van der Feen, J., DeLaPaz, R., & Smith, B. H. (1987). Enzymes of glucose metabolism in cultured human gliomas: Neoplasia is accompanied by altered hexokinase, phosphofructokinase, and glucose-6-phosphate dehydrogenase levels. *Metabolic Brain Disease*, *2*(1), 17–30.

Faraji, F., Rettig, E. M., Tsai, H.-L., El Asmar, M., Fung, N., Eisele, D. W., & Fakhry, C. (2019). The prevalence of human papillomavirus in oropharyngeal cancer is increasing regardless of sex or race, and the influence of sex and race on survival is modified by human papillomavirus tumor status. *Cancer*, *125*(5), 761–769.

Flier, J. S., Mueckler, M. M., Usher, P., & Lodish, H. F. (1987). Elevated Levels of Glucose Transport and Transporter Messenger RNA Are Induced by ras or src Oncogenes. *Science*, *235*(4795), 1492–1495.

Genotyping and Characterization of HPV Status, Hypoxia, and Radiosensitivity in 22 Head and Neck Cancer Cell Lines—PMC. (n.d.). Retrieved August 17, 2025, from

Gormley, M., Creaney, G., Schache, A., Ingarfield, K., & Conway, D. I. (2022). Reviewing the epidemiology of head and neck cancer: Definitions, trends and risk factors. *British Dental Journal*, *233*(9), 780–786.

Göttgens, E.-L., Ansems, M., Leenders, W. P. J., Bussink, J., & Span, P. N. (2021). Genotyping and Characterization of HPV Status, Hypoxia, and Radiosensitivity in 22 Head and Neck Cancer Cell Lines. *Cancers*, *13*(5), 1069.

Groves, I. J., Drane, E. L. A., Michalski, M., Monahan, J. M., Scarpini, C. G., Smith, S. P., Bussotti, G., Várnai, C., Schoenfelder, S., Fraser, P., Enright, A. J., & Coleman, N. (2021). Short- and long-range cis interactions between integrated HPV genomes and cellular chromatin dysregulate host gene expression in early cervical carcinogenesis. *PLOS Pathogens*, *17*(8), e1009875.

Guo, Y., Meng, X., Ma, J., Zheng, Y., Wang, Q., Wang, Y., & Shang, H. (2014). Human Papillomavirus 16 E6 Contributes HIF-1α Induced Warburg Effect by Attenuating the VHL-HIF-1α Interaction. *International Journal of Molecular Sciences*, *15*(5), 7974–7986.

Haeggblom, L., Attoff, T., Yu, J., Holzhauser, S., Vlastos, A., Mirzae, L., Ährlund-Richter, A., Munck-Wikland, E., Marklund, L., Hammarstedt-Nordenvall, L., Ye, W., Ramqvist, T., Näsman, A., & Dalianis, T. (2019). Changes in incidence and prevalence of human papillomavirus in tonsillar and base of tongue cancer during 2000-2016 in the Stockholm region and Sweden. *Head & Neck*, *41*(6), 1583–1590.

Hanahan, D., & Weinberg, R. A. (2011). Hallmarks of Cancer: The Next Generation. *Cell*, *144*(5), 646–674.

Höckel, M., & Vaupel, P. (2001). Tumor Hypoxia: Definitions and Current Clinical, Biologic, and Molecular Aspects. *JNCI: Journal of the National Cancer Institute*, *93*(4), 266–276.

Huebbers, C. U., Adam, A. C., Preuss, S. F., Schiffer, T., Schilder, S., Guntinas-Lichius, O., Schmidt, M., Klussmann, J. P., & Wiesner, R. J. (2015). High glucose uptake unexpectedly is accompanied by high levels of the mitochondrial β-F1-ATPase subunit in head and neck squamous cell carcinoma. *Oncotarget*, *6*(34), 36172–36184.

Huebbers, C. U., Verhees, F., Poluschkin, L., Olthof, N. C., Kolligs, J., Siefer, O. G., Henfling, M., Ramaekers, F. C. S., Preuss, S. F., Beutner, D., Seehawer, J., Drebber, U., Korkmaz, Y., Lam, W. L., Vucic, E. A., Kremer, B., Klussmann, J. P., & Speel, E.-J. M. (2019). Upregulation of AKR1C1 and AKR1C3 expression in OPSCC with integrated HPV16 and HPV-negative tumors is an indicator of poor prognosis. *International Journal of Cancer*, *144*(10), 2465–2477.

Israelsen, W. J., & Vander Heiden, M. G. (2015). Pyruvate kinase: Function, regulation and role in cancer. *Seminars in Cell & Developmental Biology*, *43*, 43–51.

Jackson, R., Togtema, M., & Zehbe, I. (2013). Subcellular localization and quantitation of the human papillomavirus type 16 E6 oncoprotein through immunocytochemistry detection. *Virology*, *435*(2), 425–432.

Jemal, A., Simard, E. P., Dorell, C., Noone, A.-M., Markowitz, L. E., Kohler, B., Eheman, C., Saraiya, M., Bandi, P., Saslow, D., Cronin, K. A., Watson, M., Schiffman, M., Henley, S. J., Schymura, M. J., Anderson, R. N., Yankey, D., & Edwards, B. K. (2013). Annual Report to the Nation on the Status of Cancer, 1975-2009, featuring the burden and trends in human papillomavirus(HPV)-associated cancers and HPV vaccination coverage levels. *Journal of the National Cancer Institute*, *105*(3), 175–201.

Jung, Y.-S., Najy, A. J., Huang, W., Sethi, S., Snyder, M., Sakr, W., Dyson, G., Hüttemann, M., Lee, I., Ali-Fehmi, R., Franceschi, S., Struijk, L., Kim, H. E., Kato, I., & Kim, H.-R. C. (2017a). HPV-associated differential regulation of tumor metabolism in oropharyngeal head and neck cancer. *Oncotarget*, *8*(31), 51530–51541.

Kam, W. W.-Y., & Banati, R. B. (2013). Effects of ionizing radiation on mitochondria. *Free Radical Biology and Medicine*, *65*, 607–619.

Karbalaie Niya, M. H., Keyvani, H., Safarnezhad Tameshkel, F., Salehi-Vaziri, M., Teaghinezhad-S, S., Bokharaei Salim, F., Monavari, S. H. R., & Javanmard, D. (2018). Human Papillomavirus Type 16 Integration Analysis by Real-time PCR Assay in Associated Cancers. *Translational Oncology*, *11*(3), 593–598.

Keeley, T. P., & Mann, G. E. (2019). Defining Physiological Normoxia for Improved Translation of Cell Physiology to Animal Models and Humans. *Physiological Reviews*, *99*(1), 161–234.

Klussmann, J. P., Mooren, J. J., Lehnen, M., Claessen, S. M. H., Stenner, M., Huebbers, C. U., Weissenborn, S. J., Wedemeyer, I., Preuss, S. F., Straetmans, J. M. J. A. A., Manni, J. J., Hopman, A. H. N., & Speel, E.-J. M. (2009). Genetic Signatures of HPV-related and Unrelated Oropharyngeal Carcinoma and Their Prognostic Implications. *Clinical Cancer Research*, *15*(5), 1779–1786.

Koritzinsky, M., Magagnin, M. G., van den Beucken, T., Seigneuric, R., Savelkouls, K., Dostie, J., Pyronnet, S., Kaufman, R. J., Weppler, S. A., Voncken, J. W., Lambin, P., Koumenis, C., Sonenberg, N., & Wouters, B. G. (2006). Gene expression during acute and prolonged hypoxia is regulated by distinct mechanisms of translational control. *The EMBO Journal*, *25*(5), 1114–1125.

Kunkel, M., Moergel, M., Stockinger, M., Jeong, J.-H., Fritz, G., Lehr, H.-A., & Whiteside, T. L. (2007a). Overexpression of GLUT-1 is associated with resistance to radiotherapy and adverse prognosis in squamous cell carcinoma of the oral cavity. *Oral Oncology*, *43*(8), 796–803.

Lechner, M., Liu, J., Masterson, L., & Fenton, T. R. (2022). HPV-associated oropharyngeal cancer: Epidemiology, molecular biology and clinical management. *Nature Reviews. Clinical Oncology*, *19*(5), 306–327.

Leemans, C. R., Braakhuis, B. J. M., & Brakenhoff, R. H. (2011). The molecular biology of head and neck cancer. *Nature Reviews. Cancer*, *11*(1), 9–22.

Li, J. Z., Gao, W., Chan, J. Y.-W., Ho, W.-K., & Wong, T.-S. (2012). Hypoxia in Head and Neck Squamous Cell Carcinoma. *ISRN Otolaryngology*, *2012*, 708974.

Li, N., Chamkha, I., Verma, G., Swoboda, S., Lindstedt, M., Greiff, L., Elmér, E., & Ehinger, J. (2024). Human papillomavirus-associated head and neck squamous cell carcinoma cells rely on glycolysis and display reduced oxidative phosphorylation. *Frontiers in Oncology*, *13*.

Lim, Y. X., & D'Silva, N. J. (2024). HPV-associated oropharyngeal cancer: In search of surrogate biomarkers for early lesions. *Oncogene*, *43*(8), 543–554.

Ma, D., Huang, Y., & Song, S. (2019a). Inhibiting the HPV16 oncogene-mediated glycolysis sensitizes human cervical carcinoma cells to 5-fluorouracil. *OncoTargets and Therapy*, *12*, 6711–6720.

Mainguené, J., Vacher, S., Kamal, M., Hamza, A., Masliah-Planchon, J., Baulande, S., Ibadioune, S., Borcoman, E., Cacheux, W., Calugaru, V., Courtois, L., Crozes, C., Deloger, M., Girard, E., Delord, J.-P., Dubray-Vautrin, A., Larbi Chérif, L., Dupain, C., Jeannot, E., … Bièche, I. (2022). Human papilloma virus integration sites and genomic signatures in head and neck squamous cell carcinoma. *Molecular Oncology*, *16*(16), 3001–3016.

Martínez-Ramírez, I., Carrillo-García, A., Contreras-Paredes, A., Ortiz-Sánchez, E., Cruz-Gregorio, A., & Lizano, M. (2018). Regulation of Cellular Metabolism

by High-Risk Human Papillomaviruses. *International Journal of Molecular Sciences*, *19*(7), 1839.

Mathupala, S. P., Ko, Y. H., & Pedersen, P. L. (2006). Hexokinase II: Cancer's double-edged sword acting as both facilitator and gatekeeper of malignancy when bound to mitochondria. *Oncogene*, *25*(34), 4777–4786.

McKeown, S. R. (2014). Defining normoxia, physoxia and hypoxia in tumours-implications for treatment response. *The British Journal of Radiology*, *87*(1035), 20130676.

Michiels, C., Tellier, C., & Feron, O. (2016). Cycling hypoxia: A key feature of the tumor microenvironment. *Biochimica et Biophysica Acta (BBA) - Reviews on Cancer*, *1866*(1), 76–86.

Mims, J., Bansal, N., Bharadwaj, M. S., Chen, X., Molina, A. J., Tsang, A. W., & Furdui, C. M. (2015). Energy Metabolism in a Matched Model of Radiation Resistance for Head and Neck Squamous Cell Cancer. *Radiation Research*, *183*(3), 291–304.

Muñoz-Bello, J. O., Olmedo-Nieva, L., Castro-Muñoz, L. J., Manzo-Merino, J., Contreras-Paredes, A., González-Espinosa, C., López-Saavedra, A., & Lizano, M. (2018). HPV-18 E6 Oncoprotein and Its Spliced Isoform E6*I Regulate the Wnt/β-Catenin Cell Signaling Pathway through the TCF-4 Transcriptional Factor. *International Journal of Molecular Sciences*, *19*(10), Article 10.

Olthof, N. C., Speel, E.-J. M., Kolligs, J., Haesevoets, A., Henfling, M., Ramaekers, F. C. S., Preuss, S. F., Drebber, U., Wieland, U., Silling, S., Lam, W. L., Vucic, E. A., Kremer, B., Klussmann, J.-P., & Huebbers, C. U. (2014a). Comprehensive analysis of HPV16 integration in OSCC reveals no significant impact of physical status on viral oncogene and virally disrupted human gene expression. *PloS One*, *9*(2), e88718.

Olthof, N. C., Speel, E.-J. M., Kolligs, J., Haesevoets, A., Henfling, M., Ramaekers, F. C. S., Preuss, S. F., Drebber, U., Wieland, U., Silling, S., Lam, W. L., Vucic, E. A., Kremer, B., Klussmann, J.-P., & Huebbers, C. U. (2014b). Comprehensive analysis of HPV16 integration in OSCC reveals no significant impact of physical status on viral oncogene and virally disrupted human gene expression. *PloS One*, *9*(2), e88718.

Ozbun, M. A. (2019). Extracellular events impacting human papillomavirus infections: Epithelial wounding to cell signaling involved in virus entry. *Papillomavirus Research*, *7*, 188–192.

Paget-Bailly, P., Meznad, K., Bruyère, D., Perrard, J., Herfs, M., Jung, A. C., Mougin, C., Prétet, J.-L., & Baguet, A. (2019). Comparative RNA sequencing reveals that HPV16 E6 abrogates the effect of E6*I on ROS metabolism. *Scientific Reports*, *9*(1), 5938.

Pakos-Zebrucka, K., Koryga, I., Mnich, K., Ljujic, M., Samali, A., & Gorman, A. M. (2016). The integrated stress response. *EMBO Reports*, *17*(10), 1374–1395.

Pattillo, R. A., Hussa, R. O., Story, M. T., Ruckert, A. C., Shalaby, M. R., & Mattingly, R. F. (1977). Tumor antigen and human chorionic gonadotropin in CaSki cells: A new epidermoid cervical cancer cell line. *Science (New York, N.Y.)*, *196*(4297), 1456–1458.

Penning, T. M. (2017). Aldo-Keto Reductase Regulation by the Nrf2 System: Implications for Stress Response, Chemotherapy Drug Resistance, and Carcinogenesis. *Chemical Research in Toxicology*, *30*(1), 162–176.

Pim, D., & Banks, L. (2010). Interaction of viral oncoproteins with cellular target molecules: Infection with high-risk vs low-risk human papillomaviruses. *APMIS: Acta Pathologica, Microbiologica, et Immunologica Scandinavica*, *118*(6–7), 471–493.

Pol, S. V. (2015). Papillomavirus E6 Oncoproteins Take Common Structural Approaches to Solve Different Biological Problems. *PLOS Pathogens*, *11*(10), e1005138.

Qin, T., Koneva, L. A., Liu, Y., Zhang, Y., Arthur, A. E., Zarins, K. R., Carey, T. E., Chepeha, D., Wolf, G. T., Rozek, L. S., & Sartor, M. A. (2020). Significant association between host transcriptome-derived HPV oncogene E6* influence score and carcinogenic pathways, tumor size, and survival in head and neck cancer. *Head & Neck*, *42*(9), 2375–2389.

Reder, H., Wagner, S., Wuerdemann, N., Langer, C., Sandmann, S., Braeuninger, A., Dugas, M., Gattenloehner, S., Wittekindt, C., & Klussmann, J. P. (2021). Mutation patterns in recurrent and/or metastatic oropharyngeal squamous cell carcinomas in relation to human papillomavirus status. *Cancer Medicine*, *10*(4), 1347–1356.

Rietbergen, M. M., Leemans, C. R., Bloemena, E., Heideman, D. A. M., Braakhuis, B. J. M., Hesselink, A. T., Witte, B. I., Baatenburg de Jong, R. J., Meijer, C. J. L. M., Snijders, P. J. F., & Brakenhoff, R. H. (2013). Increasing prevalence rates of HPV attributable oropharyngeal squamous cell carcinomas in the Netherlands as assessed by a validated test algorithm. *International Journal of Cancer*, *132*(7), 1565–1571.

Robinson, K. M., Janes, M. S., Pehar, M., Monette, J. S., Ross, M. F., Hagen, T. M., Murphy, M. P., & Beckman, J. S. (2006). Selective fluorescent imaging of superoxide in vivo using ethidium-based probes. *Proceedings of the National Academy of Sciences*, *103*(41), 15038–15043.

Sannigrahi, M. K., Rajagopalan, P., Lai, L., Liu, X., Sahu, V., Nakagawa, H., Jalaly, J. B., Brody, R. M., Morgan, I. M., Windle, B. E., Wang, X., Gimotty, P. A., Kelly, D. P., White, E. A., & Basu, D. (n.d.). HPV E6 regulates therapy responses in oropharyngeal cancer by repressing the PGC-1α/ERRα axis. *JCI Insight*, *7*(18), e159600.

Sonawane, K., Suk, R., Chiao, E. Y., Chhatwal, J., Qiu, P., Wilkin, T., Nyitray, A. G., Sikora, A. G., & Deshmukh, A. A. (2017). Oral Human Papillomavirus Infection: Differences in Prevalence Between Sexes and Concordance With Genital Human Papillomavirus Infection, NHANES 2011 to 2014. *Annals of Internal Medicine*, *167*(10), 714–724.

Speel, E. J. M. (2017). HPV Integration in Head and Neck Squamous Cell Carcinomas: Cause and Consequence. In W. Golusiński, C. R. Leemans, & A. Dietz (Eds.), *HPV Infection in Head and Neck Cancer* (pp. 57–72). Springer International Publishing.

Spriggs, K. A., Bushell, M., & Willis, A. E. (2010). Translational Regulation of Gene Expression during Conditions of Cell Stress. *Molecular Cell*, *40*(2), 228–237.

Storrs, C. H., & Silverstein, S. J. (2007). PATJ, a Tight Junction-Associated PDZ Protein, Is a Novel Degradation Target of High-Risk Human Papillomavirus E6 and the Alternatively Spliced Isoform 18 E6*. *Journal of Virology*, *81*(8), 4080–4090.

Suarez-Arnedo, A., Torres Figueroa, F., Clavijo, C., Arbeláez, P., Cruz, J. C., & Muñoz-Camargo, C. (2020). An image J plugin for the high throughput image analysis of in vitro scratch wound healing assays. *PloS One*, *15*(7), e0232565.

Sun, L., Shen, X., Liu, Y., Zhang, G., Wei, J., Zhang, H., Zhang, E., & Ma, F. (2010). The location of endogenous wild-type p53 protein in 293T and HEK293 cells expressing low-risk HPV-6E6 fusion protein with GFP. *Acta Biochimica Et Biophysica Sinica*, *42*(3), 230–235.

Symer, D. E., Akagi, K., Geiger, H. M., Song, Y., Li, G., Emde, A.-K., Xiao, W., Jiang, B., Corvelo, A., Toussaint, N. C., Li, J., Agrawal, A., Ozer, E., El-Naggar, A. K., Du, Z., Shewale, J. B., Stache-Crain, B., Zucker, M., Robine, N., … Gillison, M. L. (2022). Diverse tumorigenic consequences of human papillomavirus integration in primary oropharyngeal cancers. *Genome Research*, *32*(1), 55–70.

Tang, J.-Y., Li, D.-Y., He, L., Qiu, X.-S., Wang, E.-H., & Wu, G.-P. (2020). HPV 16 E6/E7 Promote the Glucose Uptake of GLUT1 in Lung Cancer Through Downregulation of TXNIP Due to Inhibition of PTEN Phosphorylation. *Frontiers in Oncology*, *10*, 559543.

Tiron, A., Ristescu, I., Postu, P. A., Tiron, C. E., Zugun-Eloae, F., & Grigoras, I. (2020). Long-Term Deleterious Effects of Short-term Hyperoxia on Cancer Progression—Is Brain-Derived Neurotrophic Factor an Important Mediator? An Experimental Study. *Cancers*, *12*(3), Article 3.

Umnajvijit, W., Sangthong, J., Loison, F., Vaeteewoottacharn, K., & Ponglikitmongkol, M. (2021). An internal class III PDZ binding motif in HPV16 E6* protein is required for Dlg degradation activity. *Biochimica Et Biophysica Acta. General Subjects*, *1865*(5), 129850.

Van Veelen, C. W. M., Rijksen ,Gert, Van Ketel ,B. A., & and Staal, G. E. J. (1988). The Pyruvate Kinase Isoenzyme Shift in Human Gliomas: A potential marker in the treatment of gliomas. *British Journal of Neurosurgery*, *2*(2), 257–263.

Vazquez-Vega, S., Sanchez-Suarez, L. P., Andrade-Cruz, R., Castellanos-Juarez, E., Contreras-Paredes, A., Lizano-Soberon, M., Garcia-Carranca, A., & Benitez Bribiesca, L. (2013). Regulation of p14ARF expression by HPV-18 E6 variants. *Journal of Medical Virology*, *85*(7), 1215–1221.

Vigneswaran, N., & Williams, M. D. (2014). Epidemiologic trends in head and neck cancer and aids in diagnosis. *Oral and Maxillofacial Surgery Clinics of North America*, *26*(2), 123–141.

Vyas, S., Zaganjor, E., & Haigis, M. C. (2016). Mitochondria and Cancer. *Cell*, *166*(3), 555–566.

Wald, A. I., Hoskins, E. E., Wells, S. I., Ferris, R. L., & Khan, S. A. (2011). Alteration of microRNA profiles in squamous cell carcinoma of the head and neck cell lines by human papillomavirus. *Head & Neck*, *33*(4), 504–512.

Wanichwatanadecha, P., Sirisrimangkorn, S., Kaewprag, J., & Ponglikitmongkol, M. (2012b). Transactivation activity of human papillomavirus type 16 E6*I on aldo-keto reductase genes enhances chemoresistance in cervical cancer cells. *The Journal of General Virology*, *93*(Pt 5), 1081–1092.

Williams, V. M., Filippova, M., Soto, U., & Duerksen-Hughes, P. J. (2011). HPV-DNA integration and carcinogenesis: Putative roles for inflammation and oxidative stress. *Future Virology*, *6*(1), 45–57.

Woodman, C. B. J., Collins, S. I., & Young, L. S. (2007). The natural history of cervical HPV infection: Unresolved issues. *Nature Reviews Cancer*, *7*(1), 11–22.

Yan, S.-X., Luo, X.-M., Zhou, S.-H., Bao, Y.-Y., Fan, J., Lu, Z.-J., Liao, X.-B., Huang, Y.-P., Wu, T.-T., & Wang, Q.-Y. (2013). Effect of Antisense Oligodeoxynucleotides Glucose Transporter-1 on Enhancement of Radiosensitivity of Laryngeal Carcinoma. *International Journal of Medical Sciences*, *10*(10), 1375–1386.

Zanier, K., Charbonnier, S., Sidi, A. O. M. O., McEwen, A. G., Ferrario, M. G., Poussin-Courmontagne, P., Cura, V., Brimer, N., Babah, K. O., Ansari, T., Muller, I., Stote, R. H., Cavarelli, J., Vande Pol, S., & Travé, G. (2013). Structural Basis for Hijacking of Cellular LxxLL Motifs by Papillomavirus E6 Oncoproteins. *Science*, *339*(6120), 694–698.

Zhang, Y., Dakic, A., Chen, R., Dai, Y., Schlegel, R., & Liu, X. (2017). Direct HPV E6/Myc interactions induce histone modifications, Pol II phosphorylation, and hTERT promoter activation. *Oncotarget*, *8*(56), 96323–96339.

Zhang, Y., Koneva, L. A., Virani, S., Arthur, A. E., Virani, A., Hall, P. B., Warden, C. D., Carey, T. E., Chepeha, D. B., Prince, M. E., McHugh, J. B., Wolf, G. T.,

Rozek, L. S., & Sartor, M. A. (2016). Subtypes of HPV-Positive Head and Neck Cancers Are Associated with HPV Characteristics, Copy Number Alterations, PIK3CA Mutation, and Pathway Signatures. *Clinical Cancer Research: An Official Journal of the American Association for Cancer Research*, *22*(18), 4735–4745.

Ziogas, M., Siefer, O., Wuerdemann, N., Balaji, H., Gross, E., Drebber, U., Klussmann, J. P., & Huebbers, C. U. (2024). Analysis of Expression and Regulation of AKR1C2 in HPV-Positive and -Negative Oropharyngeal Squamous Cell Carcinoma. *Cancers*, *16*(17), Article 17.